NASA TECHNICAL MEMORANDUM

NASA TM X-3111

NASA TM X-3111

CENTAUR FEEDLINE DYNAMICS STUDY USING POWER SPECTRAL METHODS

by Carl F. Lorenzo

Lewis Research Center
Cleveland, Ohio 44135

NATIONAL AERONAUTICS AND SPACE ADMINISTRATION • WASHINGTON, D. C. • NOVEMBER 1974

1. Report No.	2. Government Accession No.	3. Recipient's Catalog No.
NASA TM X-3111		

4. Title and Subtitle	5. Report Date
CENTAUR FEEDLINE DYNAMICS STUDY USING POWER SPECTRAL METHODS	November 1974
	6. Performing Organization Code

7. Author(s)	8. Performing Organization Report No.
Carl F. Lorenzo	E-7482
	10. Work Unit No.
	501-24

9. Performing Organization Name and Address	11. Contract or Grant No.
Lewis Research Center National Aeronautics and Space Administration Cleveland, Ohio 44135	
	13. Type of Report and Period Covered
12. Sponsoring Agency Name and Address	Technical Memorandum
National Aeronautics and Space Administration Washington, D.C. 20546	14. Sponsoring Agency Code

15. Supplementary Notes

16. Abstract

Tests were conducted to determine the dynamic characteristics of the Centaur/RL-10 oxygen and hydrogen feedlines. The fundamental-mode resonant frequencies were determined by applying power spectral methods to noise-generated data from hot firings of the RL-10 engine. The effect of net positive suction pressure of the main feed pumps on resonant frequency characteristics was determined to be a straight-line relation. Power spectral methods were also used to determine the dynamic characteristics of the boost pumps.

17. Key Words (Suggested by Author(s))		18. Distribution Statement
Centaur/RL-10	POGO	Unclassified - unlimited
Dynamics	Power spectral analysis	Category 28
Feedlines	Pumps	
Fluid	Rocket engines	

19. Security Classif. (of this report)	20. Security Classif. (of this page)	21. No. of Pages	22. Price*
Unclassified	Unclassified	71	$3.75

* For sale by the National Technical Information Service, Springfield, Virginia 22151

CENTAUR FEEDLINE DYNAMICS STUDY USING POWER SPECTRAL METHODS

by Carl F. Lorenzo

Lewis Research Center

SUMMARY

Tests were conducted to determine the dynamic characteristics of the Centaur/RL-10 oxygen and hydrogen feedlines. The fundamental-mode resonant frequencies were determined by applying power spectral methods to noise-generated data from hot firings of the RL-10 engine. The effect of net positive suction pressure of the main feed pumps on resonant frequency characteristics was determined to be a straight-line relation.

Power spectral methods were also used to determine the dynamic characteristics of the boost pumps.

INTRODUCTION

This study was conducted to determine the resonant frequency characteristics of the Centaur liquid-oxygen and liquid-hydrogen feedlines, so that the lines may be properly represented in POGO[1] analysis. This determination could not be made analytically, since the effect of pump inlet compliance cannot presently be predicted analytically. Current studies (e.g., ref. 1) are approaching this problem. Previous studies (e.g., ref. 2) have used sinusoidal excitation to determine feedline characteristics. For this study, it was impractical to use a known sinusoidal disturbance to excite the feedline dynamics. Hence, the system-generated noise during hot engine firings was used as an excitation source, and power spectral methods were used to analyze the data.

Specific transfer functions for the feedlines were not determined because of the difficulty in isolating the large number of potential inputs which could be driving the lines. (Specifically, each projected area on the line which has a motion can be a dynamic pumping source for the feedline.) Instead, resonant frequencies were determined

---

[1]POGO - An instability in a rocket vehicle related to an interaction of the propulsion system with the vehicle structure.

which could be used with conventional modeling to represent the feedlines in POGO modeling.

APPARATUS

The primary test items are the fuel and oxidizer suction ducts of the Centaur vehicle. The Centaur vehicle used in these tests was housed in an altitude chamber (figs. 1 and 2) where hot firings of the engines could be performed with the engine nozzles flowing full. In addition, the facility has thermal simulation capabilities, so that the proper heat loads and temperatures can be achieved.

The operation and configuration of the balance of the Centaur vehicle are quite similar to the flight configuration with the following exceptions: First, the peroxide used to power the boost pump through a turbine drive is stored remotely from the vehicle and hence can be controlled to achieve desired speed values. Secondly, the vehicle is mounted, by attachment to the aft ring, about the periphery of the oxidant tank. Hence, vibration modes will not be the same as those in flight.

Both feedlines have the following features in common: A boost pump at the propellant tank base feeds a duct, which in turn branches in two directions to feed the two RL-10 engines used to propel the Centaur. The branches are each terminated in the main feed pumps. The branches of the liquid-hydrogen feedline are symmetrical. The branches of the liquid-oxygen feedline are of unequal length, and the common feed duct is very short. The geometries of the hydrogen and oxygen feedlines are shown in figures 3 and 4, respectively. The general characteristics and parameters of the Centaur vehicle are described in reference 3 and will not be repeated herein.

Two types of pressure transducers were used:

(1) Those common to the vehicle normal instrumentation complement: These units, in general, had response ranges limited to about 100 to 200 hertz, depending on installation. These transducer signals were ac coupled, so that dynamic effects could be studied.

(2) Flush-mounted dynamic pressure transducers of the piezoelectric type: These transducers had a frequency range of 5 hertz to 1 kilohertz (amplitude, ±3 dB).

The purpose of the high-frequency attenuation was to limit the high-frequency content of this signal, so that maximum recorder range might be utilized in the frequency range of interest. The primary range of interest was 5 to 50 hertz for frequencies pertinent to the POGO problem. However, it was recognized that the line resonance could be above this frequency range. In addition, it was felt that the availability of higher frequency data and possibly higher line modes might be useful in identifying the fundamental line modes. Hence, the ranges of interest were 0 to 100 hertz for the primary

modes and 0 to 1000 hertz for higher modes.

An analysis of the liquid-hydrogen feed system is presented in appendix A. All symbols are defined in appendix B.

PROCEDURE

The following procedure was used in obtaining the required test data: When appropriate ambient (test chamber) pressures and temperatures were achieved, the RL-10 rocket engines were fired. The data were recorded on frequency-modulated recording tape for later analysis. Test runs were made to allow adjustment of instrument sensitivity when possible. The net positive suction pressure (NPSP) for the main pumps was varied by adjusting the peroxide flow to the boost pump drive turbines, thereby varying boost pump speed. In cases where NPSP was varied from the normal operating point, the off-design condition was achieved by first starting at the normal operating point and then changing boost pump speed after stable operation had been achieved. The duration of a data point (i.e., a given NPSP setting) was approximately 120 seconds. From this data record, sections as long as 80 seconds of "steady state" (constant NPSP) data could be selected for analysis.

DATA ANALYSIS

The primary data analysis was the determination of the power spectral density for the sensed signals. From data of this form, the system dynamics could be studied. The power spectral analysis was performed with a Federal Scientific analyzer. With this analyzer, the bandwidth is in a fixed relation to frequency range and sample time. Specifically,

$$\beta = \frac{1}{T}$$

and

$$T = \frac{500}{F}$$

where the bandwidth β, in hertz, is the reciprocal of the time duration of the input signal (in the digital memory); T is the time, in seconds, for a single sample; and F is

the frequency range of the analysis in hertz. Two frequency ranges are considered in this report, 100 and 1000 hertz. The following table summarizes the analysis parameters associated with the power spectra presented in the report:

Analysis frequency range, F, Hz	Single-sample time, T, sec	Bandwidth, β, Hz	Noise bandwidth,[a] β_n, Hz	Number of samples	Total time, t, sec
100	5	0.2	0.32	16	80
1000	1/2	2.0	3.2	128	64

[a]The noise bandwidth (or effective bandwidth) β_n is the bandwidth of a rectangular filter which passes a signal with the same mean square value as the actual filter when the filter input is white Gaussian noise.

Except where noted otherwise, for the 100-hertz analysis, 16 samples were averaged together, requiring a total recording time of 64 seconds. In all cases, the starting times of the analysis were the same. Each analysis yields 500 frequency points as output.

For purposes of this study, the following quantities are of interest: The autocorrelation function $R_x(\tau)$ is defined by

$$R_x(\tau) = \lim_{T\to\infty} \frac{1}{T} \int_0^T x(t)x(t+\tau)\, dt$$

The power spectral density function $G_x(f)$ is defined by

$$G_x(f) = 2\int_{-\infty}^{\infty} R_x(\tau)e^{-j2\pi f\tau}\, d\tau = 4\int_0^{\infty} R_x(\tau)\cos 2\pi f\tau\, d\tau$$

This can also be expressed as

$$G_x(f) = \lim_{\Delta f\to 0}\lim_{T\to\infty} \frac{1}{(\Delta f)T}\int_0^T x^2(t, f, \Delta f)\, dt$$

where $x(t, f, \Delta f)$ is that portion of $x(t)$ in the frequency range of f to $f + \Delta f$.

For more details and applications of these functions, see reference 4 or similar texts. An approximation to these functions was formed by the analyzer, which is described in the analyzer manual (ref. 5). The averaging technique used in the analyzer

functioned by taking the square of the ensemble average of the voltage (linear) spectrum. Because of the limitations of the analysis equipment, the frequencies in the first 5 or 10 percent of the analysis range are questionable. For this reason, no important conclusions are drawn from that part of the data.

RESULTS AND DISCUSSION

Most of the results of the experimental study are presented as plots of power spectral density (PSD) as a function of frequency. As an aid to interpreting this information, the rotational speeds of the major components of the RL-10 system are presented in table I. Associated with each of these rotational speeds is a characteristic frequency (based on one pulse per revolution), which is also presented in the table. In the data, multiples of these frequencies also occur. In the tests where NPSP was varied, the variation was achieved by changing boost-pump turbine speeds. Hence, the frequencies varied appropriately relative to those in the table.

As indicated previously, the NPSP was stepped between desired values during long engine firings. Four values of NPSP were studied for each propellant system; these are tabulated in table II. The plots of NPSP as a function of time, on which the table is based, are presented in figures 5 and 6. Straight lines have been faired through the segments of data on which the power spectral analysis was performed.

In interpreting the data that follow, the high power concentrations associated with turbomachinery rotational speeds and the thrust controller frequency are not of interest. In general, the data to be presented are considered as the comparison of the PSD's of two channels. With this form of comparison the square root of the ratio of the PSD's of the channels could be interpreted as the amplitude ratio if the input channel were the only input (coherence was equal to 1). Hence, the difference (on a log basis) can be viewed as a psuedo-transfer-function amplitude ratio.

Apparent in some of the data that follow is a significant frequency content at 5 hertz, which has been identified as the limit cycle frequency of the thrust controller. This is indicated quite prominently on the chamber pressure PSD plot in figure 7.

Hydrogen Feedline Dynamics

A diagram of the liquid-hydrogen feedline is shown in figure 8. In this system, a boost pump supplies a main feed duct which branches into two equal-length legs which in turn supply liquid hydrogen to the main feed pumps. Indicated on the diagram are both the pressure and acceleration instrumentation locations and identifying numbers (which

are referred to in the text). Also shown are the various expansion joints and bellows. The duct makes many changes in direction. These bends provide projected areas which under vibration can allow local dynamic pumping of fluid.

Power spectral densities were computed from time histories for each of the instruments indicated in figure 8. This computation was made for both the accelerations and the pressures. All pressures but 801P were measured with flush-mounted transducers. The PSD plots obtained from the outputs of these transducers form the key results of the study.

The power spectral densities for the two extreme ends of the hydrogen duct, that is, the outlet of the boost pump (803P) and the inlet to the C-2 main fuel pump (802P), are shown in the top half of figure 9. The NPSP of 47.5 kN/m^2 (6.9 psi) for the data of this plot is the nominal operating NPSP for the RL-10 engine system. The figure shows that the power spectra are quite similar at the low-frequency end, gradually diverge at medium frequencies to a maximum difference at 44 hertz, and gradually converge again at high frequencies. This indicates a peak in the amplitude between the two channels and, hence, a fluid mode of the duct at 44 hertz.

The power spectral density of the pressure at the junction of the branch lines is added to the curves for 802P and 803P in the bottom half of figure 9. The junction pressure (822P) power spectral density exhibits the same general trends as those of 802P and 803P but lies between them from 0 to 100 hertz. The junction pressure PSD is very close to the 803P values.

Figures 10 to 12 present similar data for decreasing values of NPSP. In all cases, the pressures at the two extreme ends of the hydrogen duct are given, and the junction pressure is added in a subsequent plot. The general trends are the same as those noted for the nominal NPSP condition. However, the maximum difference in PSD between the extreme ends of the line varies with increasing NPSP. This difference would correspond to a damping variation. Further, the frequency at which the resonance occurs shifts with NPSP.

It is useful to examine these data in another form before generalizing the results. If the data shown on these plots, together with the remaining pressures indicated in figure 8, are smoothed to eliminate the statistical variations and cross plotted for a particular frequency as a function of distance along the duct, these data can be interpreted as fluid-pressure-mode shapes.

The transducer 801P was a cavity-type transducer, and its dynamic characteristics were not known. An indication of that transducer response can be obtained by examining the PSD of that transducer for all runs relative to similar data for the flush transducer 802P on the C-2 engine side. These plots are shown in figure 13. If we assume that the two sides behave in a similar manner, comparison of these plots indicates a resonance in the transducer in the vicinity of 200 hertz. Thus, the transducer would not be valid

for high frequencies but would appear to be usable at frequencies to 100 hertz.

A magnitude ratio of pressure at some position x along the ducts to pressure at the junction can be calculated from the PSD's of the signals by using the relation

$$\left|\frac{P_x}{P_J}\right| \approx \sqrt{\frac{G_x}{G_J}}$$

where G is the power spectral density. We assume that the coherence is high, otherwise this relation is not valid. Applying this procedure to the data of run 8G-1 (fig. 9), the nominal NPSP condition, yields the fluid-pressure-mode shapes of figure 14. The parameter on the figure is frequency, ranging from 20 to 50 hertz. As frequency increases from 20 to 44 hertz, the magnitude ratio increases also; above 44 hertz, the magnitude ratio decreases (e.g., the 50-Hz line). Additional frequencies above 50 hertz have not been shown in order to eliminate confusion on the plots.

Data are not available for the C-1 engine branch duct except at the termination. The terminating points are shown on the left side of figure 14; the values are approximately the same as those for the terminating points on the C-2 engine side. These results suggest that the behavior is that of a quarter-wave mode with the two branch ducts acting as parallel elements and behaving in similar manner. Specifically, a mode from end to end in the branch ducts (i.e., an unsymmetrical mode from engine to engine) does not occur in this frequency range. This conclusion cannot be drawn from the data alone since phase information is not available. However, analysis of similar systems (appendix A) indicates that the unsymmetric mode occurs at a frequency considerably above the symmetric mode.

Further, the magnitude ratio of the main feed duct being less than 1.0 indicates that the dominant disturbance to the system originates near the main feed pump. Again, the conclusion is based on the rough modeling results of appendix A.

Also, comparison of the experimental pressure-mode-shape results with the analytically determined mode shape indicates that the experimental mode shapes have a downward trend in the vicinity of the main pump. This trend is probably caused by the fact that the termination is not a simple compliance as was assumed in the analytical model. It is quite likely that nonlinear effects are occurring, probably associated with the pump inlet cavitation "bubble." Such nonlinear effects have been discussed in the literature (e.g., ref. 6). Generally, similar results are obtained as the NPSP is reduced from nominal, as shown in figure 15.

The mode shapes of largest magnitude (at resonance) for each NPSP have been plotted together for ease of comparison in figure 16. Figures 17 and 18 summarize the experimentally observed behavior of the liquid-hydrogen feedline dynamics as a function

of NPSP. The resonant frequency (fig. 18) appears as a straight-line function of NPSP. Although similar results have been observed in the literature (ref. 7), the reader is cautioned against accepting this result literally since a significant amount of interpretation is involved in determining the frequency values in view of the statistical variation. In figure 18 the maximum value of the mode-shape plots is shown as a function of NPSP.

Oxygen Feedline Dynamics

A diagram of the liquid-oxygen feedline is shown in figure 19. The system is functionally similar to the hydrogen feedline, except that the branch ducts for the oxygen system are of unequal length, resulting in an unsymmetrical system. Also, the main feed duct is very short, precluding pressure measurements. Since the liquid-oxygen feedline is unsymmetrical, it was decided to put the detailed instrumentation on the long leg (i.e., to the C-2 engine side). A single cavity transducer was placed at the termination of the C-1 engine feedline (805P). The pressure 809P is considered to be the junction pressure. The transducer 806P failed during the test sequence. Since it was impractical to open the facility to replace it, the closest transducer, 812P, will be the basis of argument in the following discussion.

The power spectral density plots for the oxygen duct as a function of NPSP are presented in figures 20 to 23. The data in figure 20 were taken at the nominal NPSP of 154.0 kN/m^2 (22.3 psi).

The interpretation of the data is not as straightforward for the oxygen feedline as for the hydrogen feedline. By consideration of both the end pressures and the intermediate pressures (through-mode shapes) for all the NPSP for the oxygen duct, it appears that the duct resonance occurs in the 95- to 100-hertz frequency range. This observation appears to be contradicted when NPSP is 154.0 kN/m^2 (22.3 psi) (fig. 22). In this figure there is some apparent dynamic activity in the lower frequency range. Examination of the pressure-mode shapes in this area, however, does not indicate a resonant condition in the feedline. The peak in spectral power at 61 hertz results from the passing frequencies associated with the liquid-oxygen boost pump and is not a line resonance.

The power spectral densities of the termination pressures, together with those of the intermediate pressures, are shown in figure 21. From this figure, it becomes more apparent that the resonance is in the 95- to 100-hertz range. This result is also shown at an NPSP of 77.9 kN/m^2 (11.3 psi) in figure 22. The intermediate-line-pressure PSD's at this NPSP are also shown in figure 22. These intermediate values lie between the PSD's for the terminating pressures, as is shown in the mode-shape plots which follow. For an NPSP of 55.8 kN/m^2 (8.1 psi), figure 23, there is no dynamic activity in the low-frequency range.

Plotting the data from all runs (all NPSP's) for the cavity transducer 805P on a single plot, figure 24, shows that the corner frequency for the transducer is about 100 hertz. The PSD data generated from this transducer are therefore considered to be usable over the range 0 to 100 hertz.

The pressure-mode-shape plots for the oxygen feedline are shown in figure 25. The characteristics are quite similar to those observed for the hydrogen feedline. The characteristic decrease in pressure ratio near the feedline termination, which was seen on the hydrogen feedline, is not so apparent with these data because of the location of the transducers on the feedline and the lost transducer.

The right branch termination (pressure 805P) is always near or slightly below the junction pressure (i.e., $|P_x/P_j| \leq 1$).

The pressure-mode shapes as a function of NPSP at the resonant frequencies are shown together for comparison purposes in figure 26. The variations in resonant frequency with NPSP for the oxygen duct are plotted in figure 27. As for the hydrogen feedline, a function approximating a straight line fits the data over the frequency range considered.

Pump Characteristics

Placement of pressure transducers upstream and downstream of the boost pumps allowed their dynamic performance to be assessed. The power spectral densities for the liquid-hydrogen boost pump inlet and discharge pressures at NPSP values of 33.1 and 17.9 kN/m^2 (4.8 and 2.6 psi) are shown in figures 28 and 29, respectively. A striking feature of these data is the significant difference in power content between inlet and discharge pressure over the entire frequency range (0 to 100 Hz). This difference is an indication of the noise-generating capability of the pump. The same characteristic is also exhibited for the main hydrogen feed pump in figure 30. However, the main hydrogen feed pump data are questionable since it was necessary to place the discharge transducer some distance from the main flow. The liquid-oxygen boost pump characteristics for NPSP of 98.5 and 55.8 kN/m^2 (14.3 and 8 psi) are shown in figures 31 and 32, respectively. For these data the discharge power is higher than the inlet power over most of the frequency range. However, there are frequency bands over which the inlet displays power concentrations which exceed those of the discharge. These concentrations occur at 9, 20, and 38 hertz, approximately. It is significant that these concentrations are not reflected at the discharge. Indeed, the power concentrations at the discharge (58 and 54 Hz) occur where there is little or no dynamic activity at the inlet. The 58- and 54-hertz peaks are the characteristic frequencies (one per revolution) of the oxygen boost pump. The oxygen main pump characteristics for an NPSP of 154.0 kN/m^2 (22.3 psi) are shown in figure 33. Here, again, because of the placement

of the discharge pressure transducer, that measurement may be dynamically degraded. There are several possible explanations for this type of behavior. The first and probably most likely explanation is that the inlet measurement is dynamically uncoupled from the discharge measurement. This uncoupling would occur physically if a large compliance existed between the two measurements that would prevent the transmission of information. The second explanation involves the possibility of nonlinearity in the pump. That is, the frequency concentration at the inlet of the pump might be moved by pump nonlinear characteristics to a different frequency. For example, if the pump behaved in a square-law manner, the energy concentrations would be moved to a frequency of twice that of the input. In the more general case where the discharge power is slightly higher than the inlet power, the additional possibility exists that an input (other than the inlet pressure) of considerably larger magnitude could be generating new frequencies and power levels, such that the inlet pressure effect is lost (or masked). The overriding input could be the rotational input of the pump shaft reflected through the blade passing frequencies.

Additional Data

There are several data plots that do not logically fit in the preceding sections but are worthwhile results of the study.

The power spectral density for C-2 thrust chamber pressure is shown in figure 7. Here dynamic activity is seen at 5 and 61 hertz. The 61-hertz peak is generated by the liquid-oxygen boost pump, as indicated previously. The 5-hertz activity was found to be associated with the thrust control valve located downstream of the main pump in the liquid-oxygen line. The transducer for this measurement is a cavity type, so that high-frequency interpretation is precluded.

It is of some interest to examine the high-frequency characteristic of the ducts; this is done, for several pressures at NPSP near nominal, for the hydrogen duct in figure 34. The various turbomachinery rotational speeds are readily apparent in the plots.

While accelerometer data was gathered and studied, no significant trends were observed relative to the pressure spectra. One interesting trend was noticed for the pump-face acceleration spectra; namely, as NPSP was increased the spectrum level increased over the frequency range of 0 to 100 hertz, as shown in figure 35.

CONCLUDING REMARKS

An experimental study of the Centaur/RL-10 liquid-oxygen and liquid-hydrogen

feedline dynamic characteristics has been made using power spectral methods. The resonant frequencies of the feedline have been identified by the power spectral technique and pressure-mode shapes determined from power spectra. Use of the power spectral density (PSD) technique eliminated the need of external dynamic excitation during the hot firing of the RL-10 rocket engines.

The effect of variation of net positive suction pressure (NPSP) was studied; the relation of feedline resonant frequency to NPSP was experimentally found to be a straight-line function over the NPSP range covered in the study.

As a generality, the one fundamental difficulty which was observed in applying the power spectral methods to determination of dynamic characteristics of these physical systems appears to be associated with determination of the inputs disturbing the system and in knowing when such inputs are active and influential.

Lewis Research Center,
National Aeronautics and Space Administration,
Cleveland, Ohio, July 8, 1974,
501-24.

APPENDIX A

ANALYSIS OF LIQUID-HYDROGEN FEED SYSTEM

An analysis of the liquid-hydrogen feed system was performed to assist in interpretation of the experimental data. A linear distributed parameter analysis of the duct was made. The configuration analyzed is that shown in figure 36, which shows the main feed duct with two equal-length branch ducts to the main pumps. The cavitation bubble and the pump and engine impedance were characterized by a resistance and compliance termination (of unknown magnitude). The system was excited by four inputs located at the exit of the boost pump, the inlets to each of the main pumps, and the junctions of the branch ducts with the main feed duct. The inputs were flow disturbances at all points except the boost pump discharge, which was a pressure disturbance. These disturbances were analogous to those which might be excited by the motion of a projected area of the duct. The analysis used the techniques of reference 8, which allow frequency responses to be easily determined. The block diagram for the system analyzed is shown in figure 37. The block diagram contains the normal distributed parameter blocks. In addition, a set of parallel distributed blocks allows computation of pressures along the ducts (for mode-shape computation). The block diagram was reduced for the transfer functions P_{x_1}/inputs and P_{x_3}/inputs.

The effect of driving-point location for the condition

$$R_A = 1.5\times10^6 \text{ N-sec/m}^5 \ (885 \text{ lbf-sec/ft}^5)$$

$$R_E = 3.56\times10^8 \text{ N-sec/m}^5 \ (2.1\times10^5 \text{ lbf-sec/ft}^5)$$

$$C_E = 1.18\times10^{-10} \text{ m}^5/\text{N} \ (2\times10^{-7} \text{ ft}^5/\text{lbf})$$

was determined (transfer function of P_F/inputs) and is shown in figures 38 to 41. For the cases presented, the termination impedances R_E of the branch ducts are equal. The response when the system is driven at the boost pump exit (P_F/I_1) is shown in figure 38. This could be viewed as the response of the system to boost-pump-generated noise. The response shows resonances at 48, 219, and 425 hertz, approximately. In addition, there is a dipole at 237 hertz which is probably caused by the symmetry of the system (i.e., both branches of the same length). The principal value of the phase angle is shown in the figures. The response when the system is driven at the junction between the two branch ducts (P_F/I_2) is shown in figure 39. The resonances occur at the same frequencies. However, the resonance at 225 hertz now is the dominant resonance relative to the 48-hertz resonance, which dominated when the I_1 signal was driving. From

these two driving points (I_1 and I_2), only the symmetrical modes of the system can be excited. That is, the system will respond in that manner in which the two branch ducts behave the same.

The response of the system to excitation at the main pump inlet (I_3), called driving-point impedance, is shown in figure 40. In this case, the symmetrical modes occur as in the previous cases. However, additional modes occur at frequencies of 73 and 376 hertz which can only be excited from points off the line of symmetry of the system. Similar results are shown in figure 41, where the excitation source is now at the inlet to the far pump (P_F/I_4). In this case, the resonance at 48 hertz is very nearly masked by the asymmetric resonance at 74 hertz. An important analytical result was that for certain combinations of the terminating parameters the symmetric resonance could be completely masked in the frequency response plots. This could pose a problem in identifying such systems by using experimental mode shapes, as was done in the study.

In order to further detail the response of this system, the "mode shapes" as a function of frequency were determined for the I_1 driving point. The symmetrical response of the system to excitation at I_1 for frequency steps between 20 and 70 hertz is shown in figure 42(a). Plots of the mode shape with excitation at point I_1 at the symmetric and asymmetric resonances of 48 and 74 hertz, respectively, are shown in figure 42(b). The relative phase angles between the local pressure and the excitation flow are shown on the plots.

The results of unsymmetrical excitation (exciting at I_3) for the same system are indicated in figure 43(a). Again, mode-shape plots near the resonant frequencies are indicated in figure 43(b). These plots are notably different than the results indicated in figure 42(b).

The responses when the system is excited at the junction have not been shown. But experience with the analysis has shown that the mode shapes on the branch ducts always follow the identical values that are obtained with excitation at I_1 and that the values on the main feedline always have the same values as those obtained when the system is driven at I_3.

The effects of terminating compliance and resistance on resonant frequency are shown in figure 44, where $R_A = 1.5\times10^6$ N-sec/m^5 (885 lbf-sec/ft^5) and the excitation source is at point I_1. When the driving point is moved to point I_3, the asymmetric mode occurs also, as is indicated in figure 45. The situation where the symmetric mode is obscured by the asymmetric mode is shown in figure 46. In these cases the numerator terms of the solutions appear to be very important and move the apparent resonant frequency (indicated by amplitude peak) as a function of driving point. This is shown in figures 47 to 50, where the resonant frequencies are 27, 30, 43, and 41 hertz, when driving at I_1, I_2, I_3, and I_4, respectively.

APPENDIX B

SYMBOLS

C	compliance, m^5/N (ft^5/lbf)
c	sonic speed, m/sec (ft/sec)
F	analysis frequency range, Hz
f	frequency, Hz
Δf	effective filter bandwidth, Hz
j	$\sqrt{-1}$
$G_x(f)$	power spectral density function
I	disturbance input location (fig. 36)
l	line length, m (ft)
N	number of samples
P	pressure, kN/m^2 (psi)
Q	volume flow, m^3/sec (ft^3/sec)
R	resistance, $N\text{-}sec/m^5$ ($lbf\text{-}sec/ft^5$)
$R_x(\tau)$	autocorrelation function
S	Laplace operator
T	time per sample, sec
t	time, sec
x	variable; position along feedline
Z_o	characteristic acoustic impedance, $N\text{-}sec/m^5$ ($lbf\text{-}sec/ft^5$)
β	bandwidth, Hz
β_n	noise bandwidth, Hz
τ	time displacement, sec

Subscripts

A, E, F, J	position in feedline (figs. 36 and 37)
j	junction
x	position along feedline
1, 2, 3	segment of feedline (fig. 39)

REFERENCES

1. Ghahremani, F. G.; and Rubin, S.: Empirical Evaluation of Pump Inlet Compliance. Rep. ATR-73(7257)-1, Aerospace Corp. (NASA CR-123963), July 1972.

2. Wagner, R. G.: Titan II Engine Transfer Function Test Results. Rep. TOR-0059(6471)-9, Aerospace Corp., Feb. 1971.

3. Anon.: Performance Evaluation of Atlas-Centaur Restart Capability in Earth Orbit. NASA TM X-1647, 1968.

4. Bendat, Julius S.; and Piersol, Allan G.: Measurement and Analysis of Random Data. John Wiley & Sons, Inc., 1966.

5. Anon.: Instruction Manual - For the Ubiquitous ® Spectrum Analyzer, The UPS-6 Series Ubiquitous ® Processing System. Federal Scientific Corp., May 19, 1969.

6. Bikle, F. A.; Fidler, L. E.; and Rohrs, J. B.: A Study of System Coupled Instability Techniques. Martin Co. (AFRPL-TR-66-143, Pts. I and II), July 1966.

7. Bramblett, G.; Knowles, R.; and Sack, L.: Pump Cavitation Impedance as a Factor in Vehicle Longitudinal Vibrations. Paper 66-559, AIAA, June 1966.

8. Lorenzo, Carl F.; and Riehl, John P.: Reduce II - A Computer Program for the Symbolic Reduction of Large Block Diagrams. NASA TN D-7621, 1974.

TABLE I. - TYPICAL ROTATIONAL SPEEDS OF MAJOR COMPONENTS OF RL-10 SYSTEM

Component	Rotational speed, rpm	Characteristic frequency, Hz
Liquid-oxygen pump	12 300	205
Liquid-hydrogen pump and turbine	30 700	512
Liquid-hydrogen boost pump turbine	40 800	680
Liquid-hydrogen boost pump	6 820	113.6
Liquid-oxygen boost pump turbine	33 600	560
Liquid-oxygen boost pump	3 690	61.6

TABLE II. - NET POSITIVE SUCTION PRESSURE FOR LIQUID HYDROGEN AND OXYGEN RL-10 PROPELLANT SYSTEMS

Run	Liquid-oxygen-system net positive suction pressure		Liquid-hydrogen-system net positive suction pressure	
	kN/m^2	psi	kN/m^2	psi
8F-1	78.3	11.3	23.4	3.4
8F-2	55.9	8.1	17.9	2.6
8G-1	154.0	22.3	47.6	6.9
8G-2	98.5	14.3	33.1	4.8

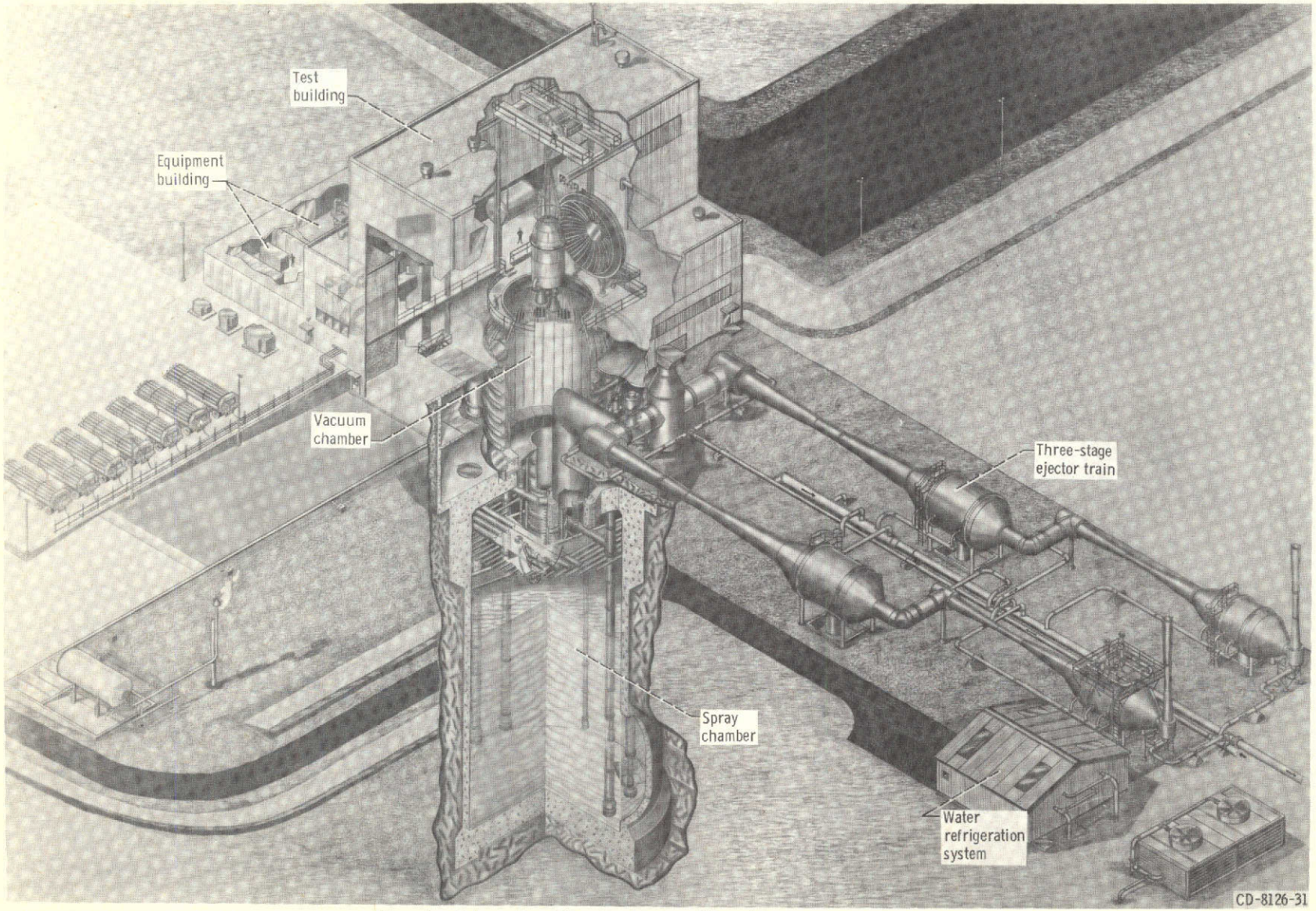

Figure 1. - Cutaway view of Plum Brook Spacecraft Propulsion Research Facility (B-2).

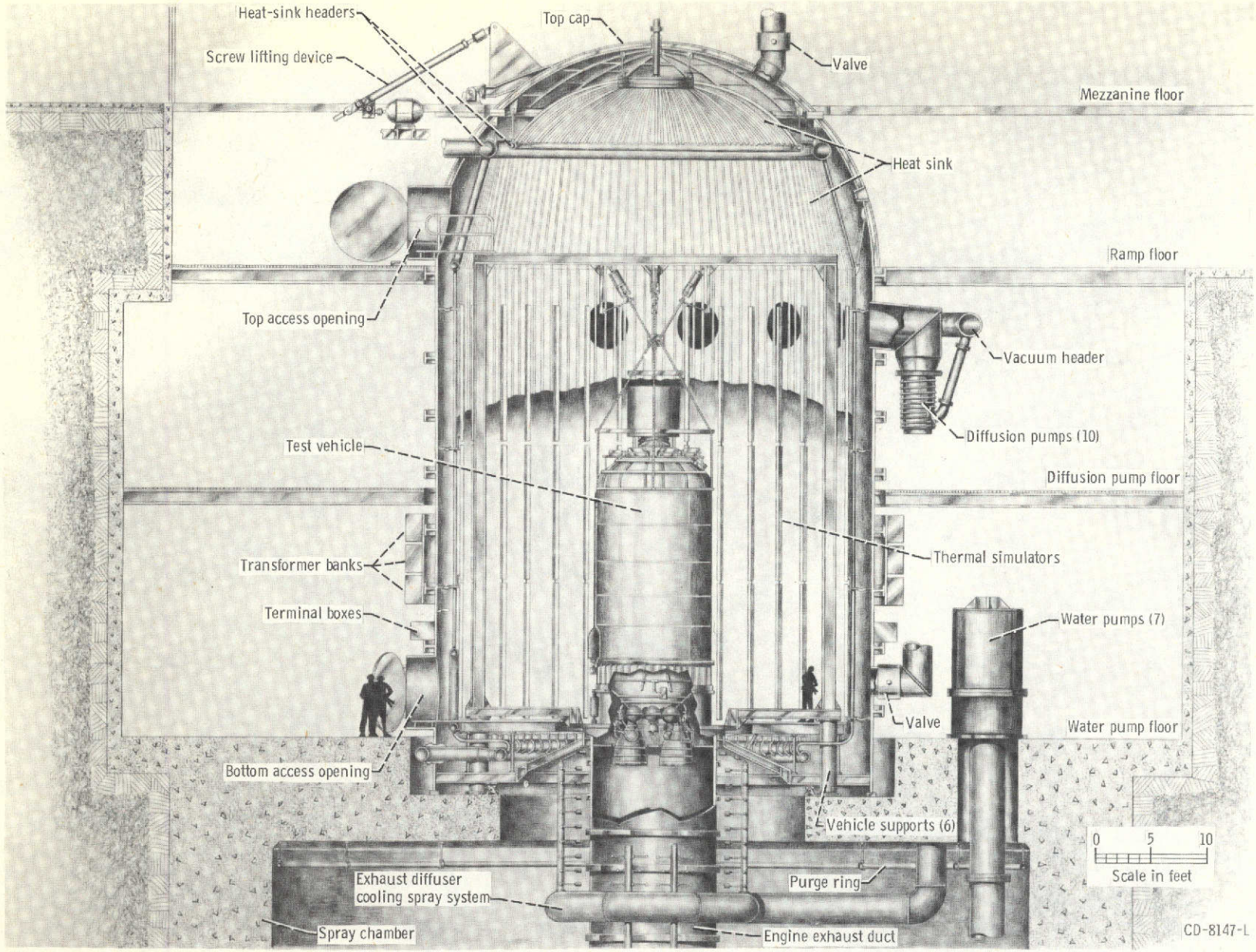

Figure 2. - Cross section through test chamber of Spacecraft Propulsion Research Facility (B-2).

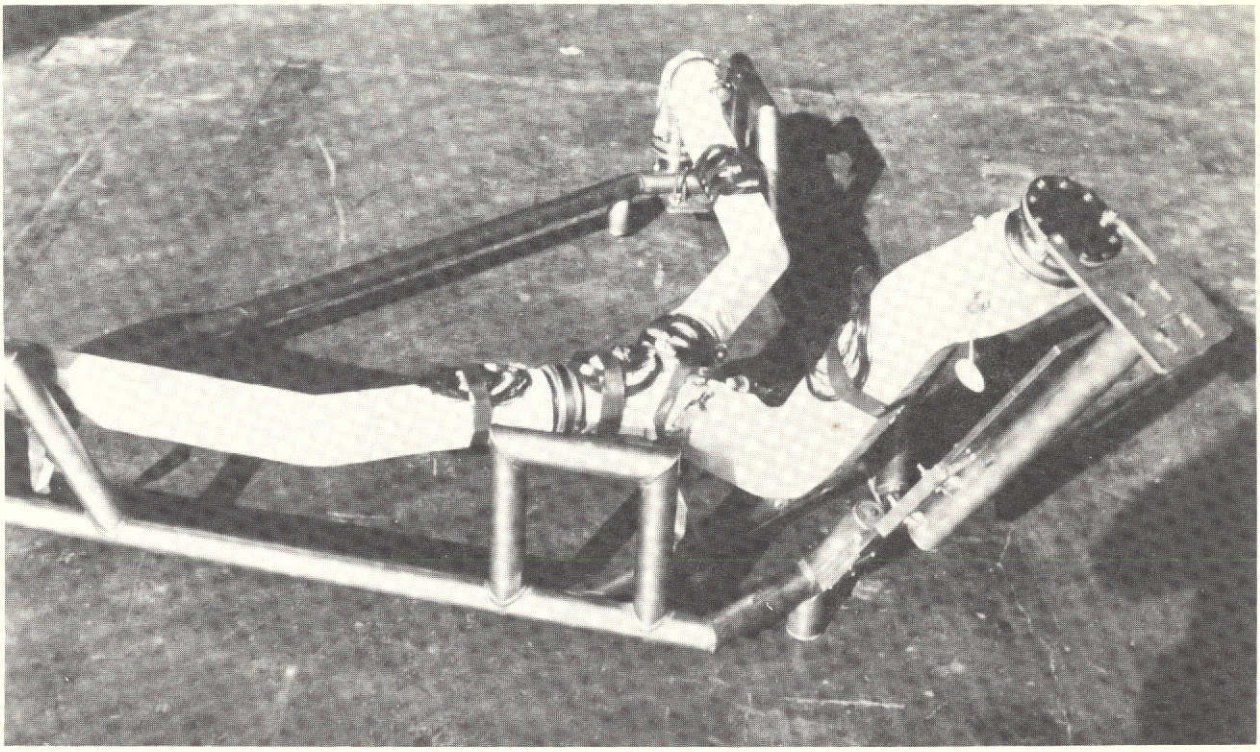

Figure 3. - Liquid-hydrogen feedline.

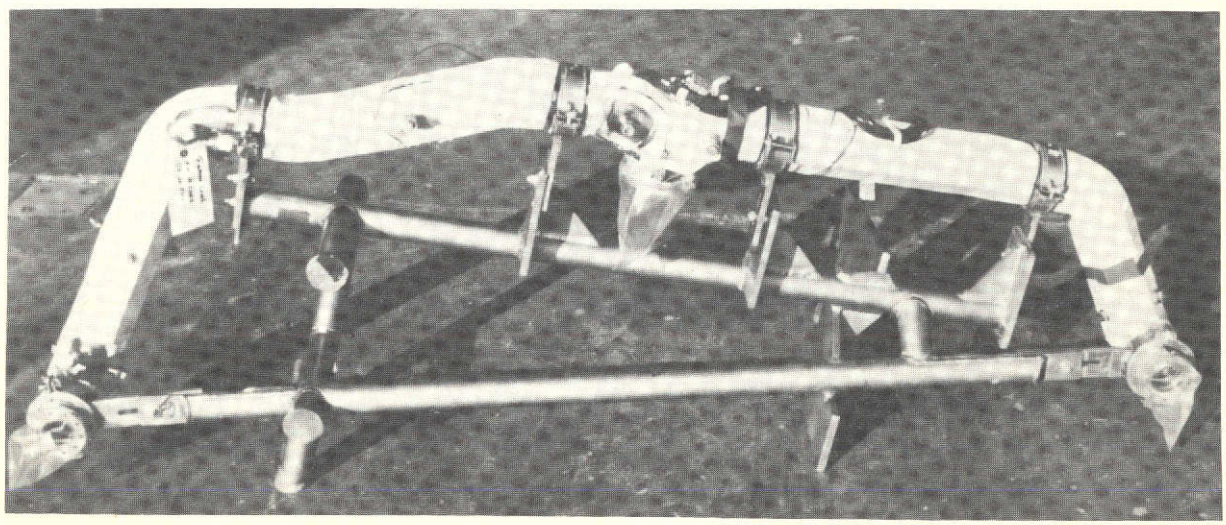

Figure 4. - Liquid-oxygen feedline.

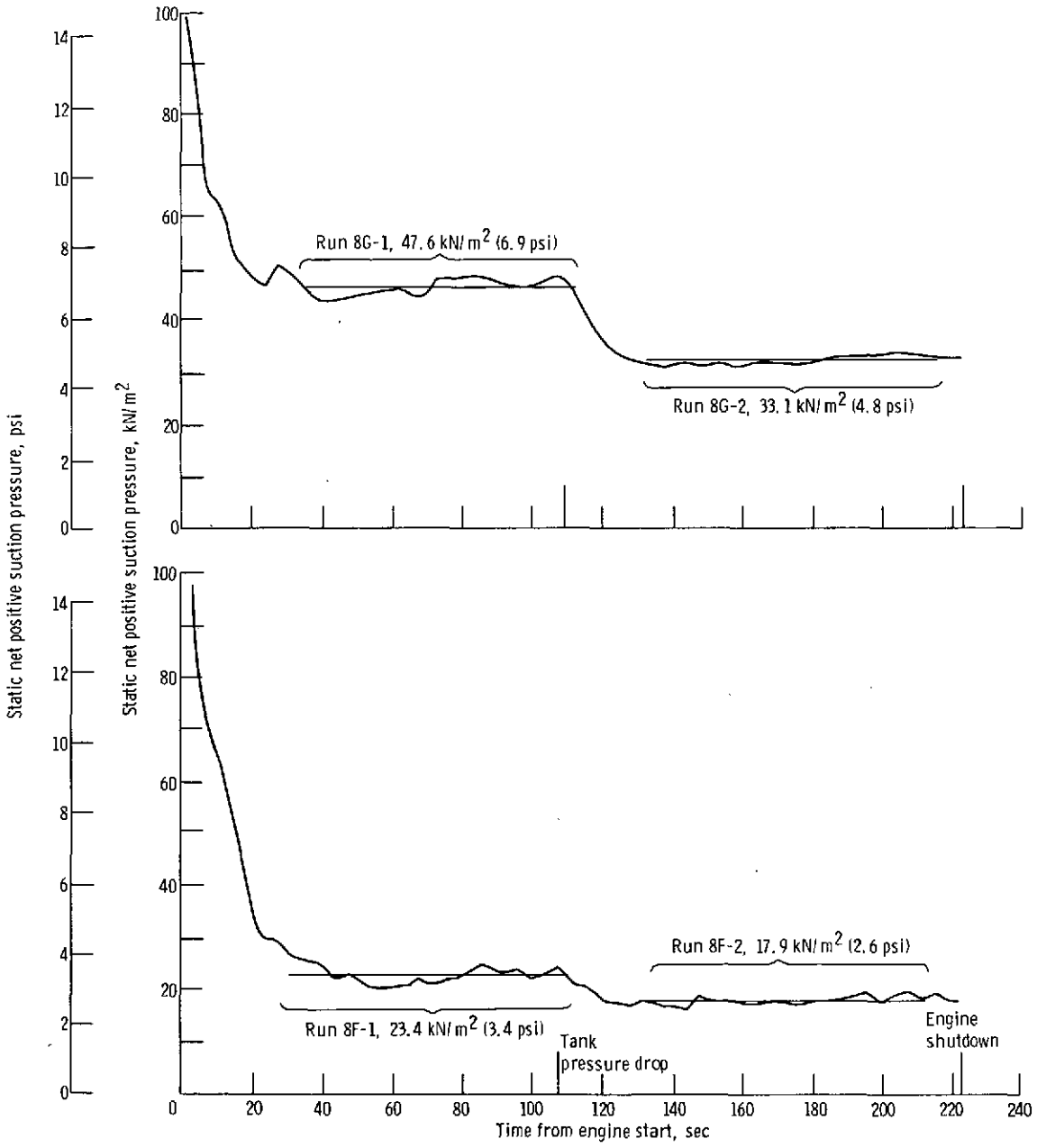

Figure 5. - Static net positive suction pressure of liquid hydrogen during C-2 engine firing.

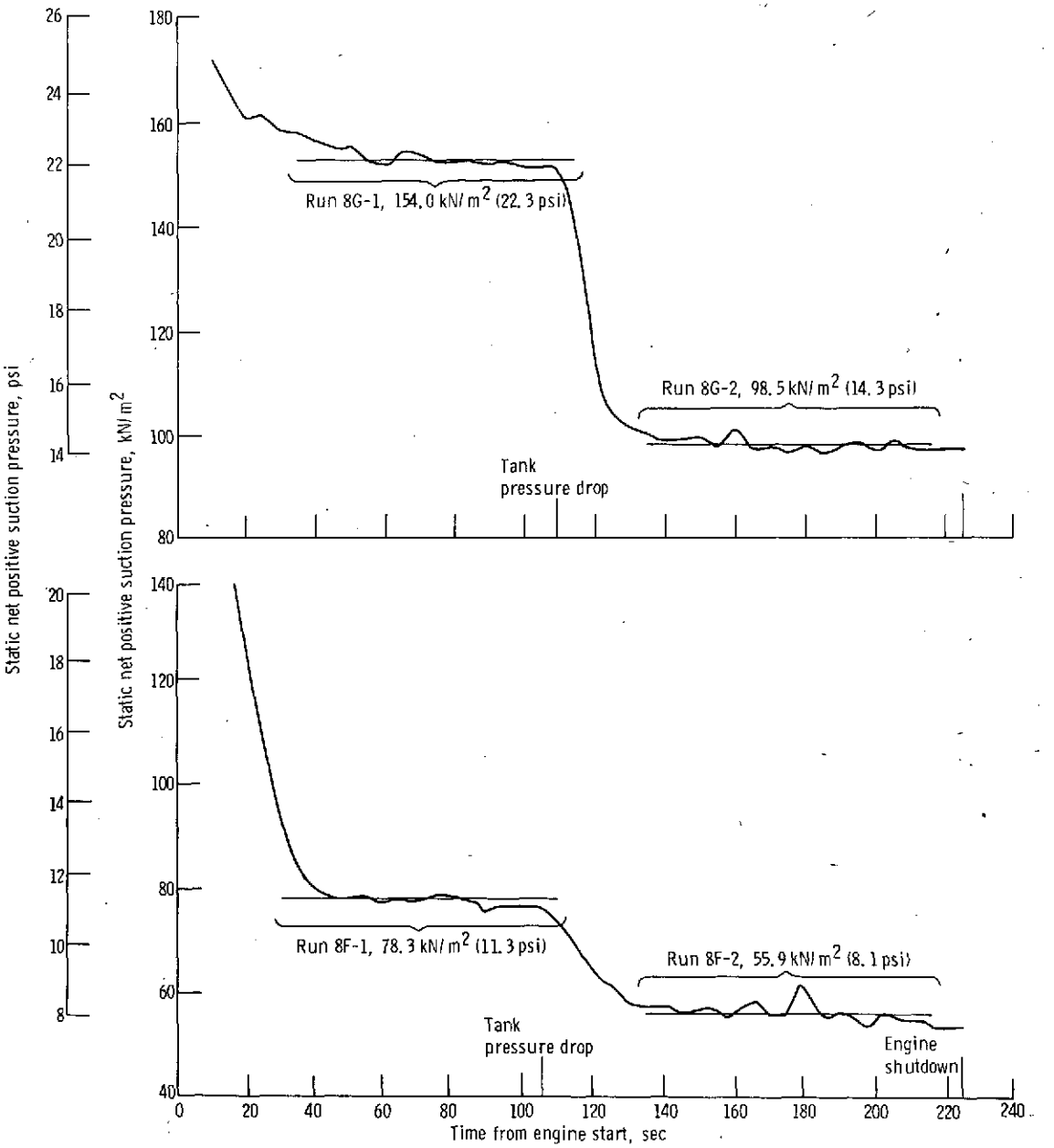

Figure 6. - Static net positive suction pressure of liquid oxygen during C-2 engine firing.

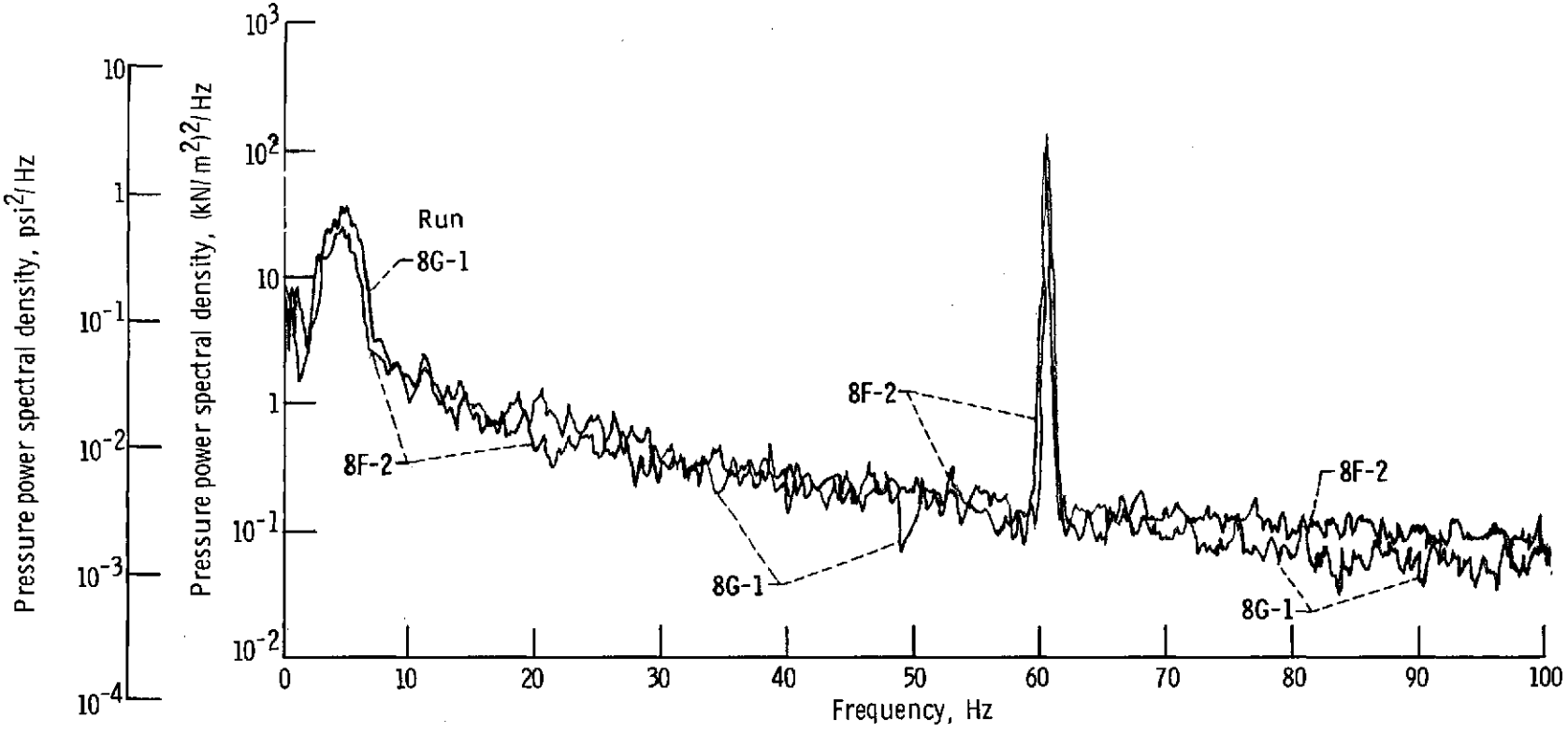

Figure 7. - Power spectral density of C-2 engine chamber pressure (821P).

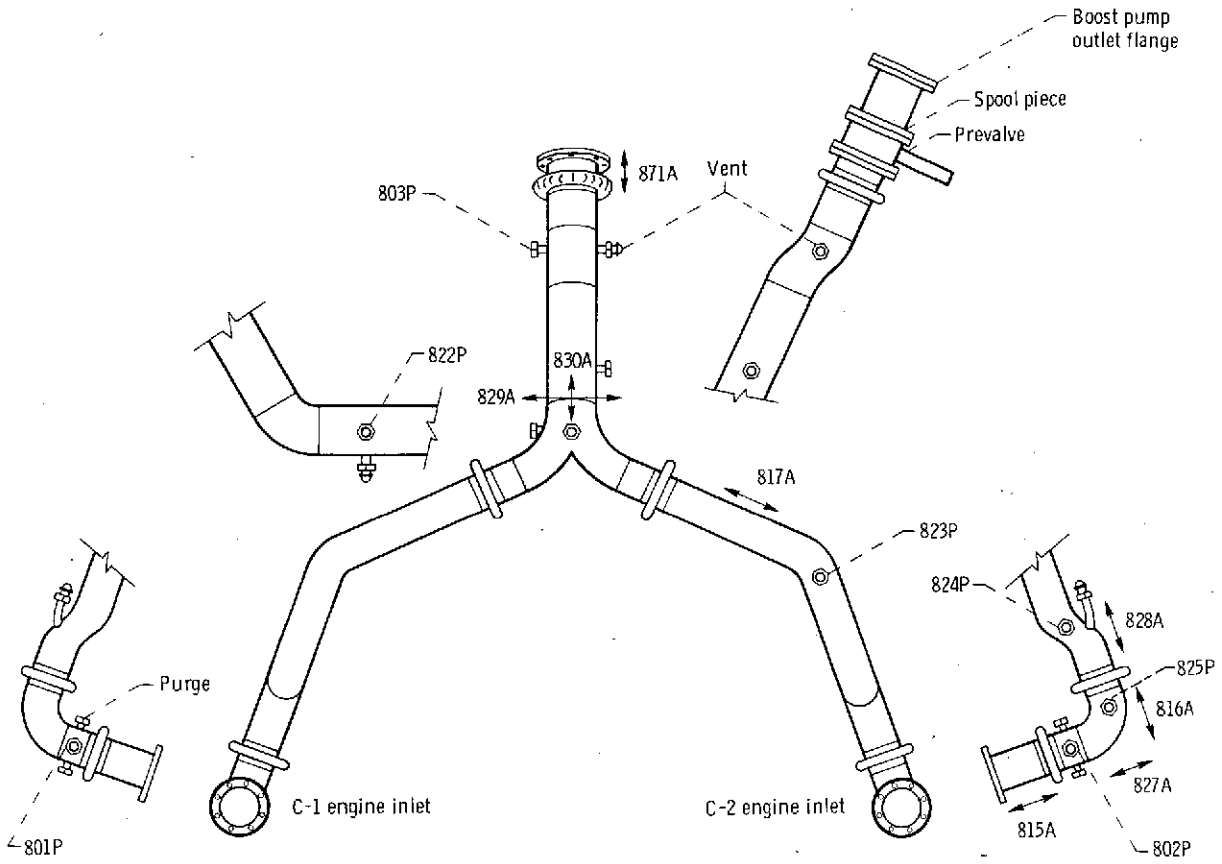

Figure 8. - Location of instrumentation on liquid-hydrogen feedline for Centaur RL-10 dynamics tests in Plum Brook B-2 test facility. View looking forward.

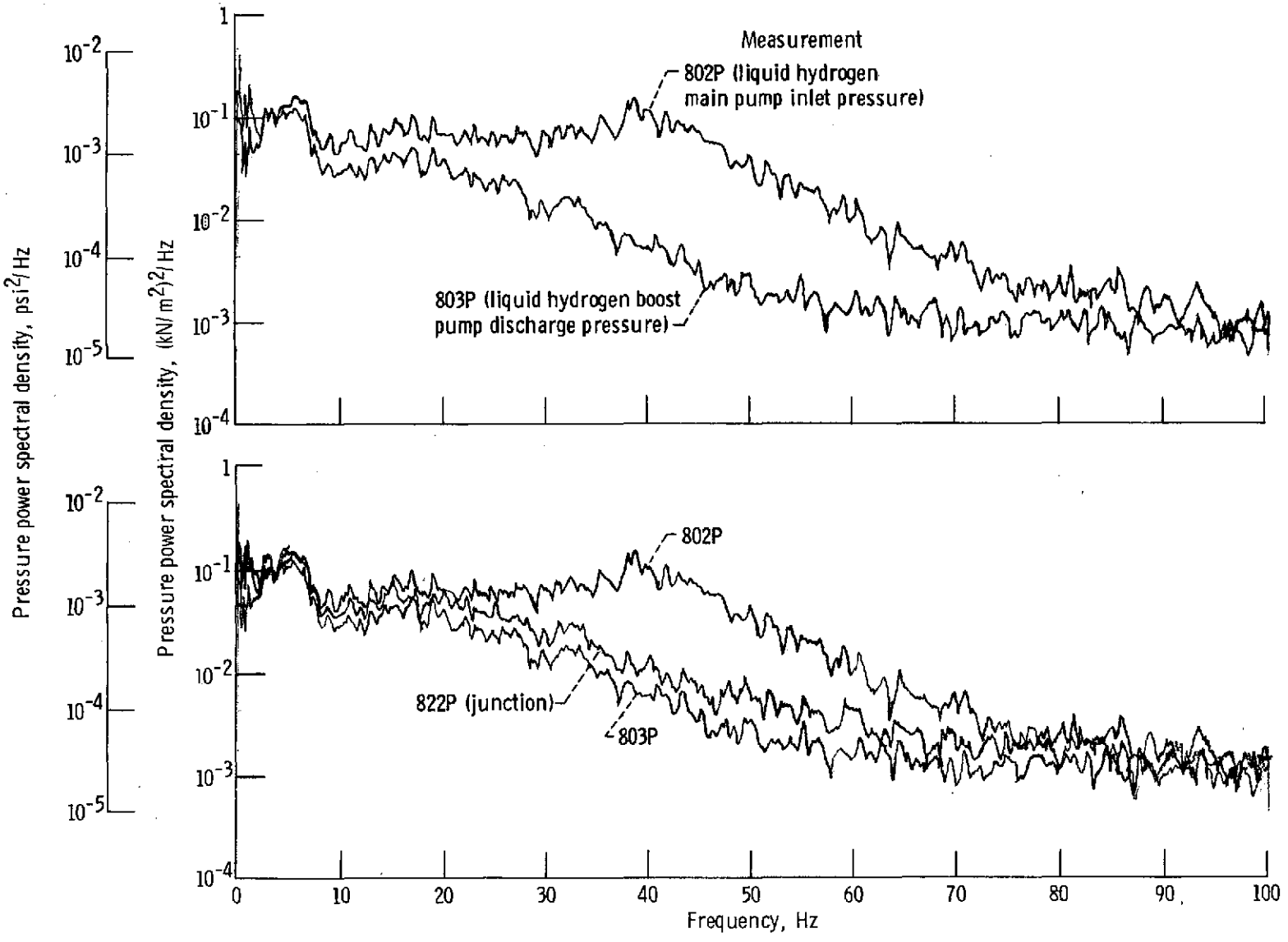

Figure 9. - Power spectral density of liquid-hydrogen feedline at a net positive suction pressure of 47.6 kN/m^2 (6.9 psi) - run 8G-1.

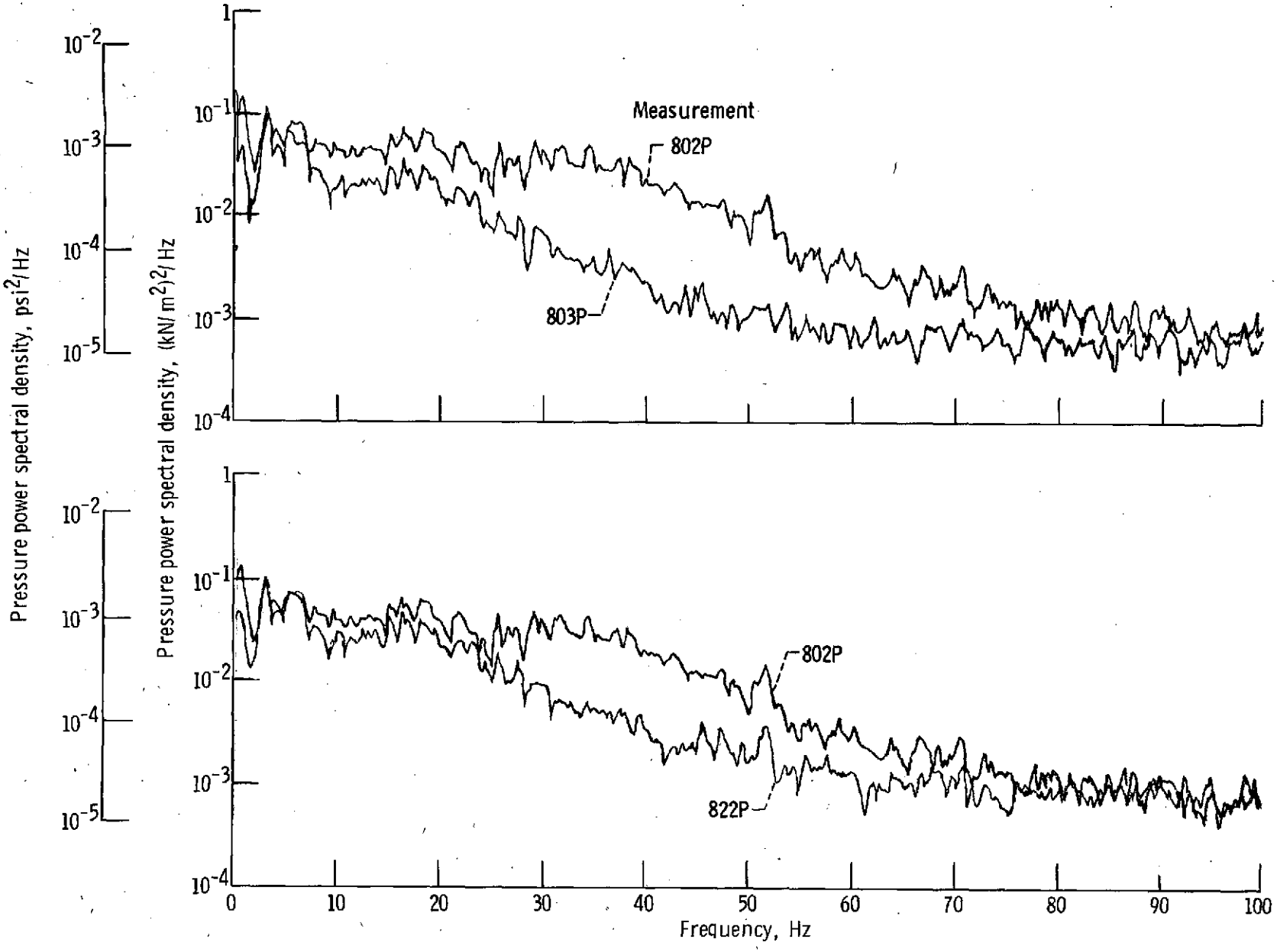

Figure 10. - Power spectral density of liquid-hydrogen feedline at net positive suction pressure of 33.1 kN/m^2 (4.8 psi) - run 8G-2.

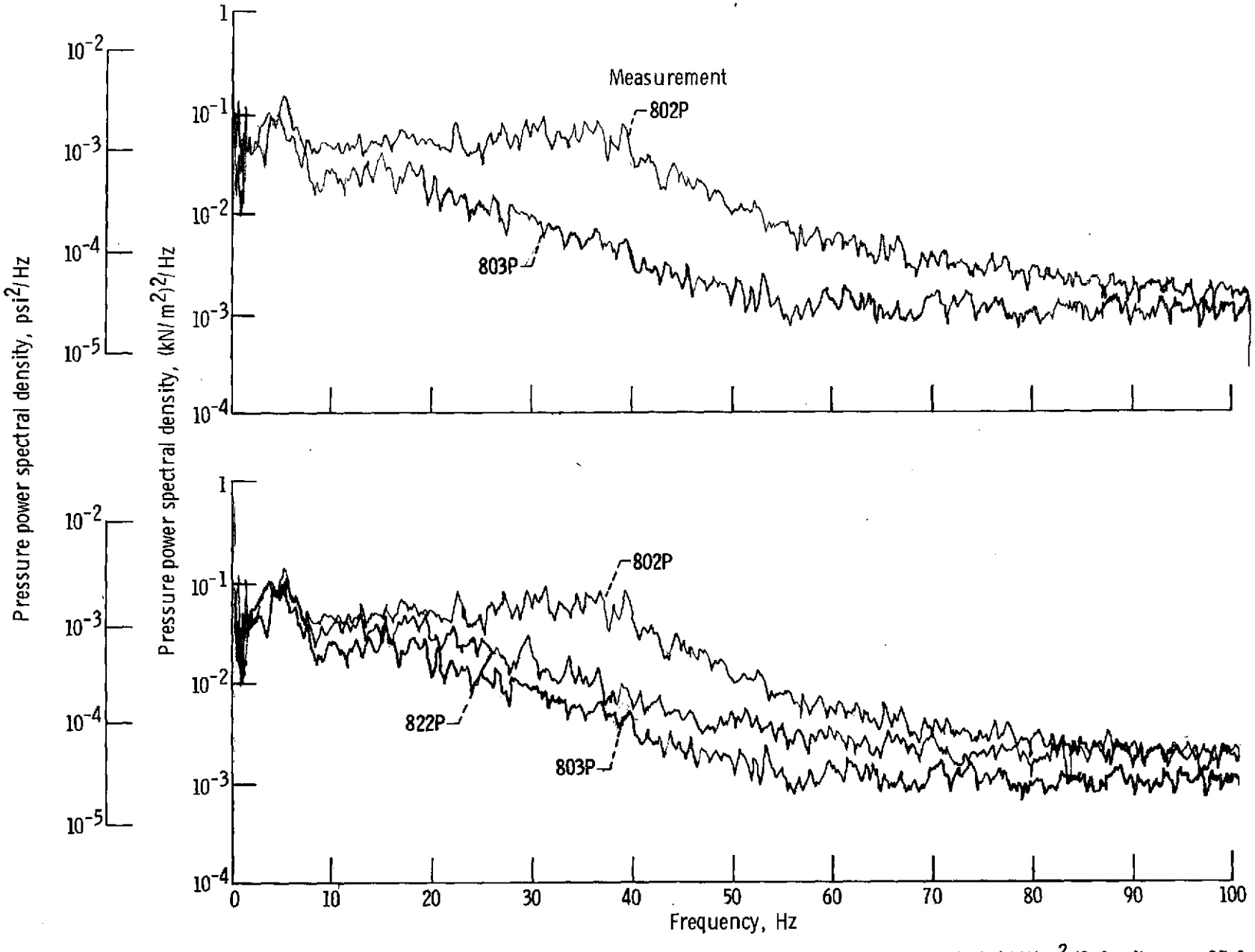

Figure 11. - Power spectral density of liquid-hydrogen feedline at net positive suction pressure of 23.4 kN/m^2 (3.4 psi) - run 8F-1.

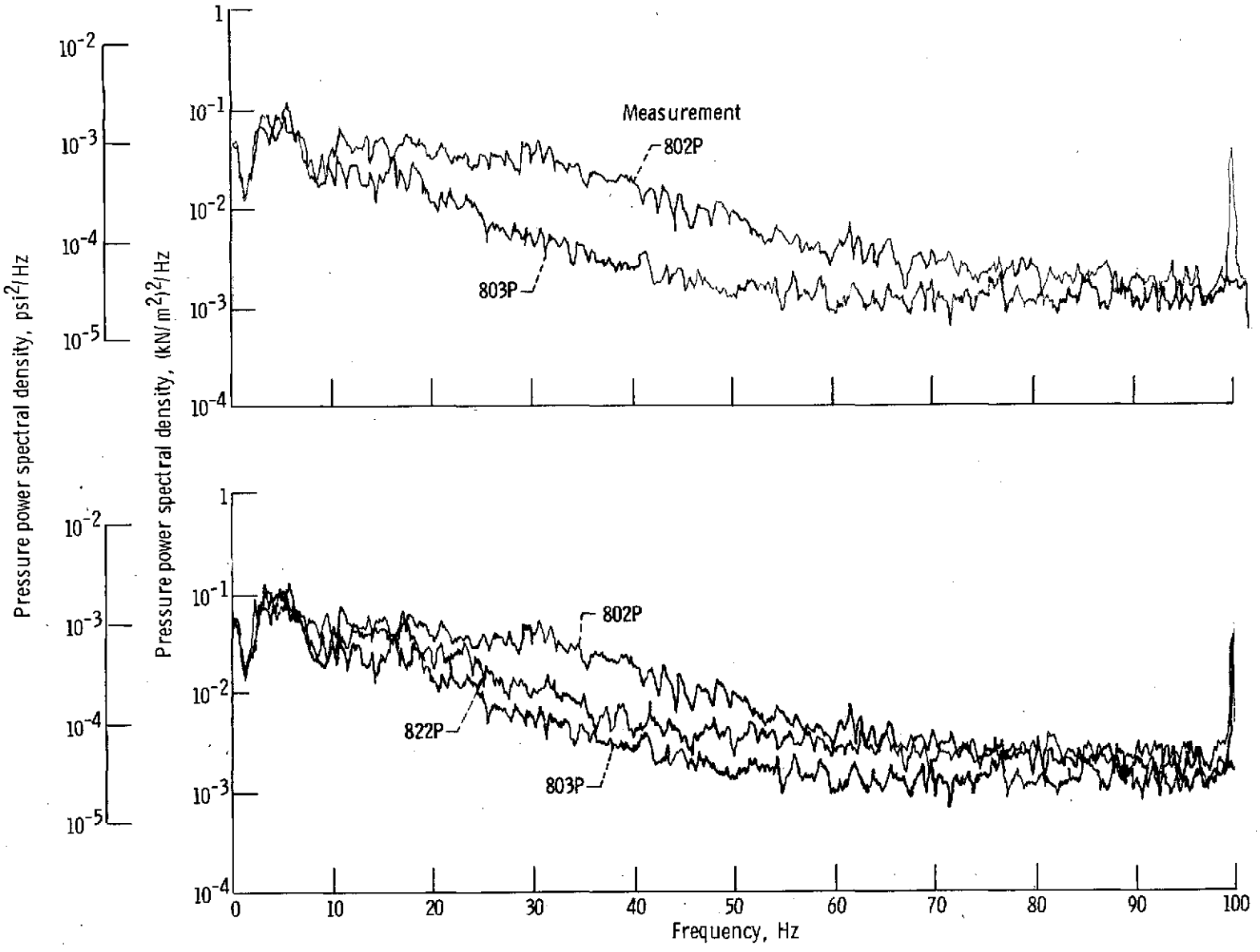

Figure 12. - Power spectral density of liquid-hydrogen feedline at net positive suction pressure of 17.9 kN/m^2 (2.6 psi) - run 8F-2.

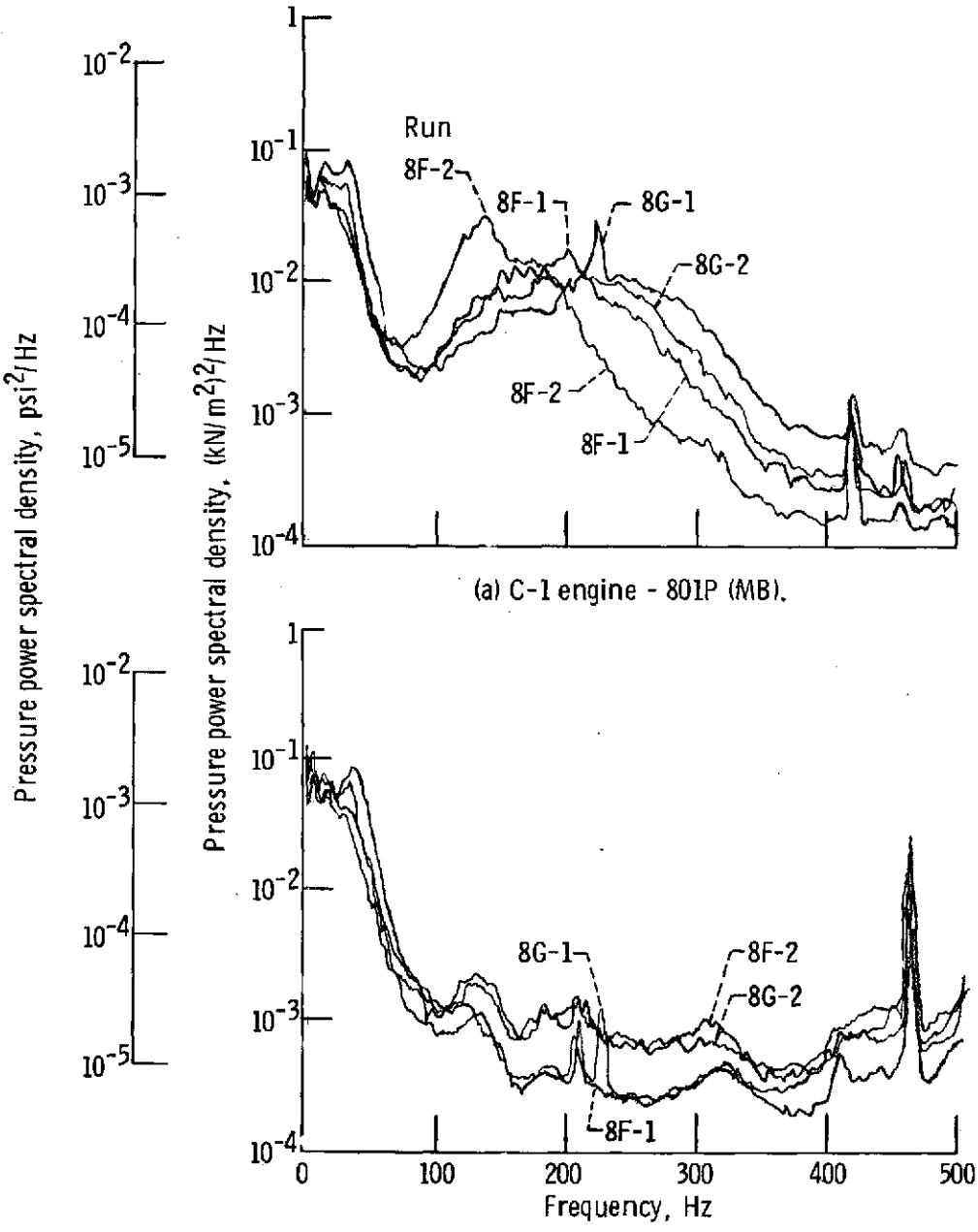

Figure 13. - Power spectral density of C-1 and C-2 engine fuel pump inlet pressure.

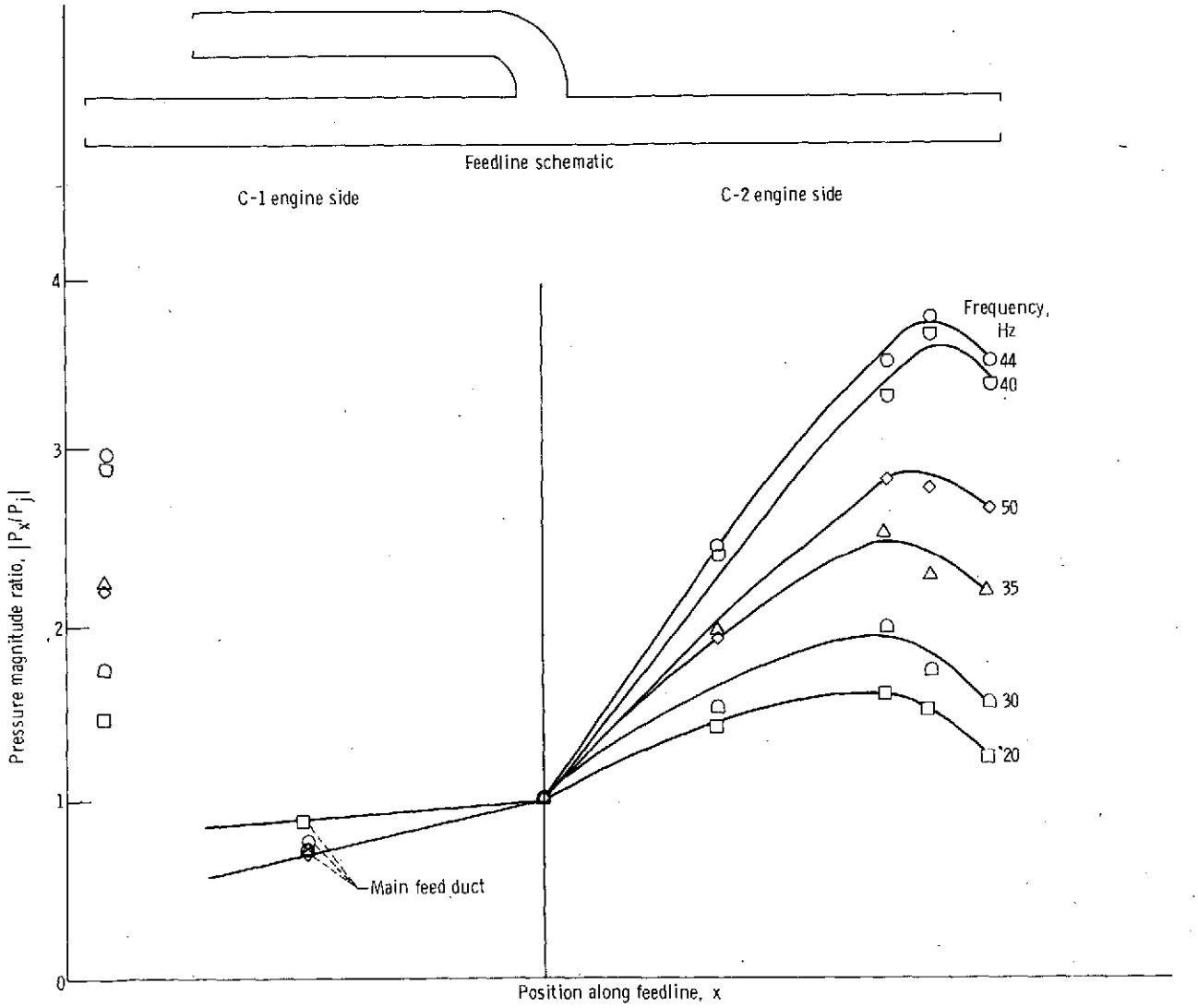

Figure 14. - Pressure magnitude ratio for liquid-hydrogen feedline at nominal net positive suction pressure of 47.6 kN/m^2 (6.9 psi) - run 8G-1.

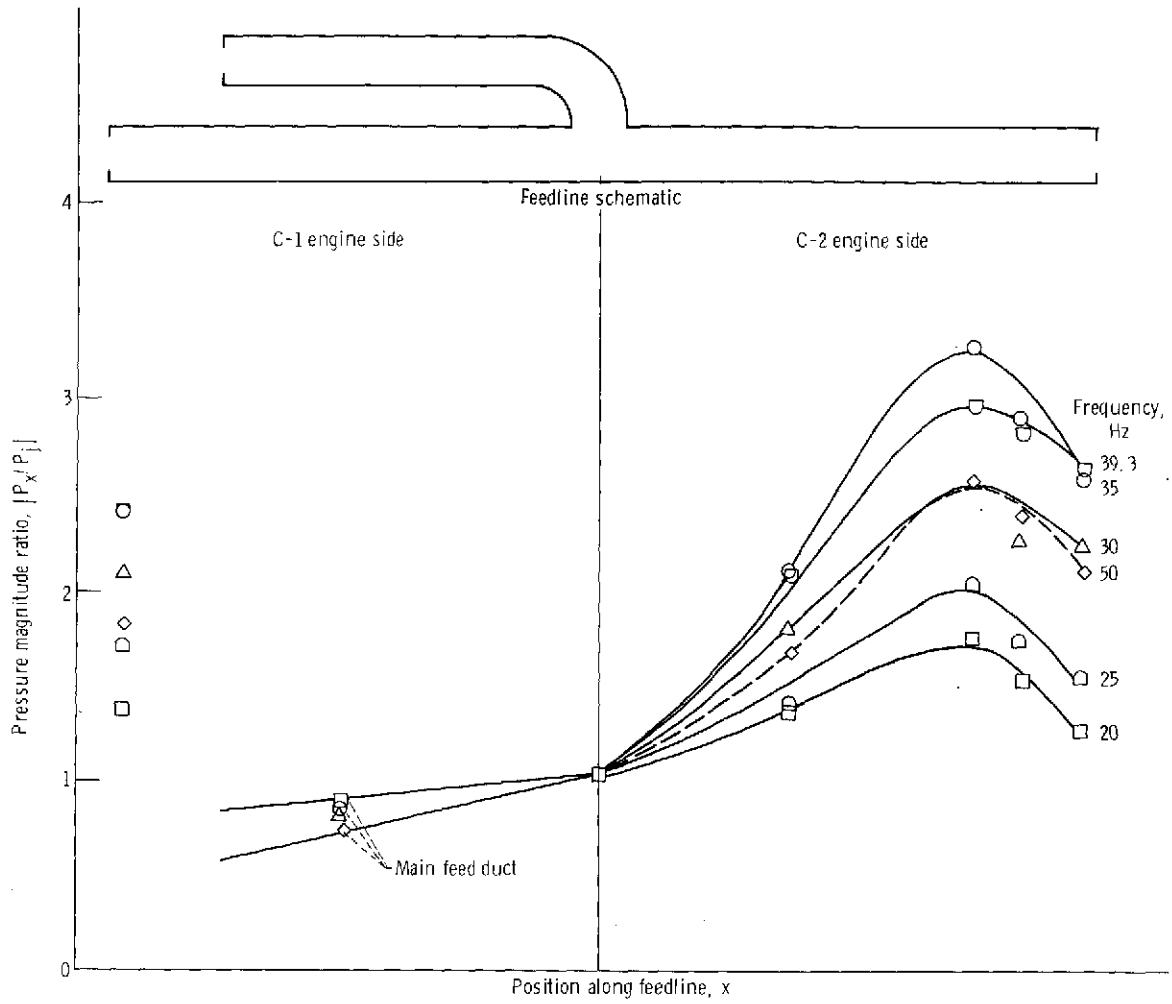

(a) NPSP = 33.1 kN/m^2 (4.8 psi); run 8G-2.

Figure 15. - Pressure magnitude ratio for liquid-hydrogen feedline at net positive suction pressures (NPSP) below nominal.

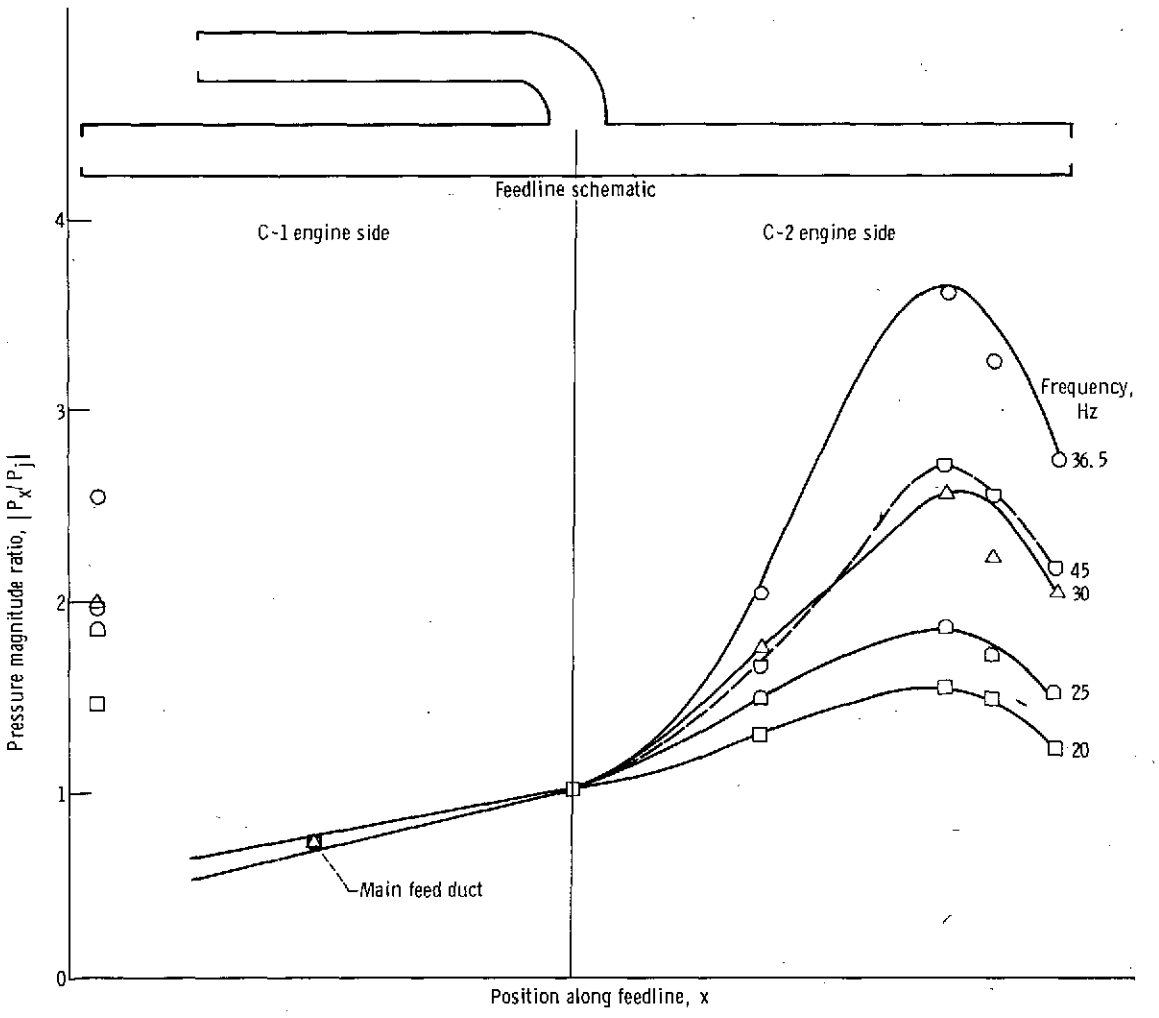

(b) NPSP = 23.4 kN/m^2 (3.4 psi); run 8F-1.

Figure 15. - Continued.

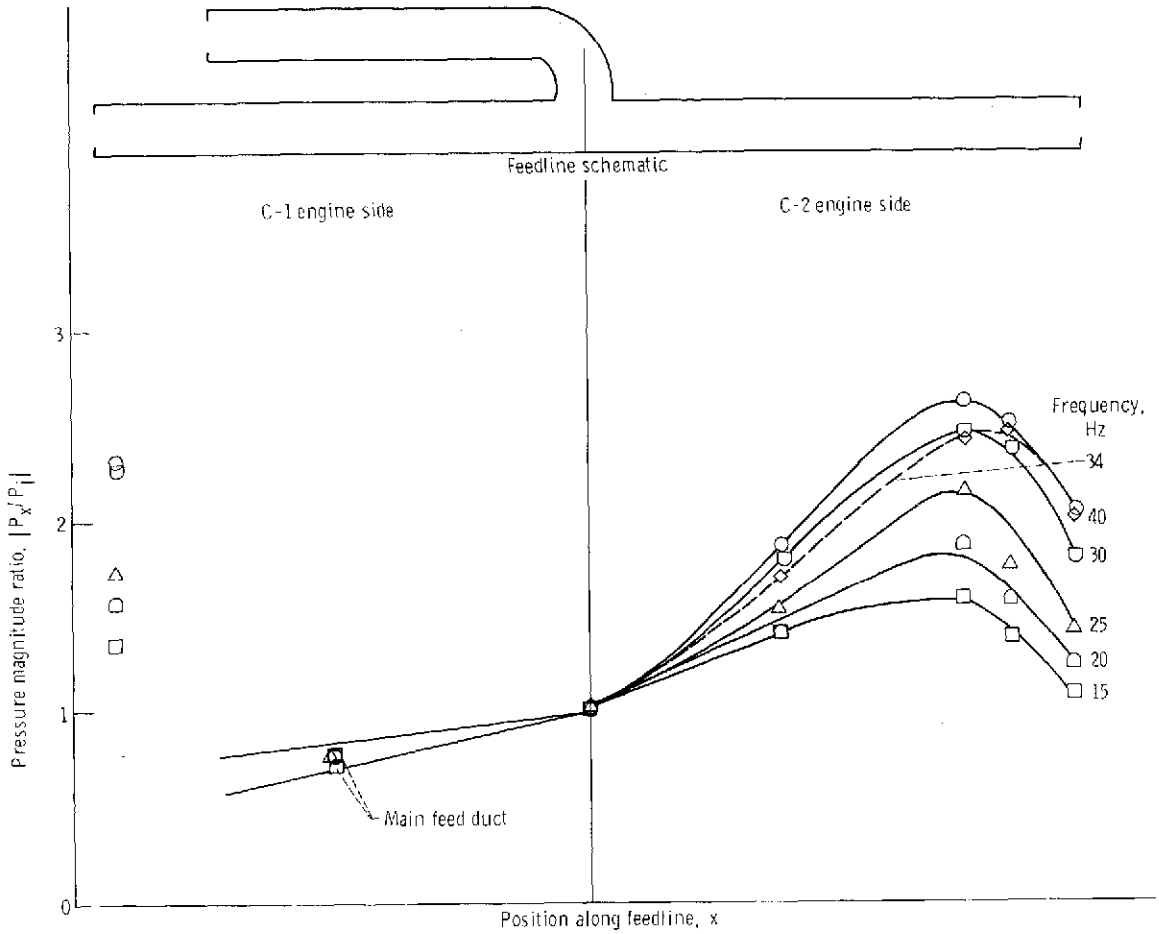

(c) NPSP = 17.9 kN/m^2 (2.6 psi); run 8F-2.

Figure 15. - Concluded.

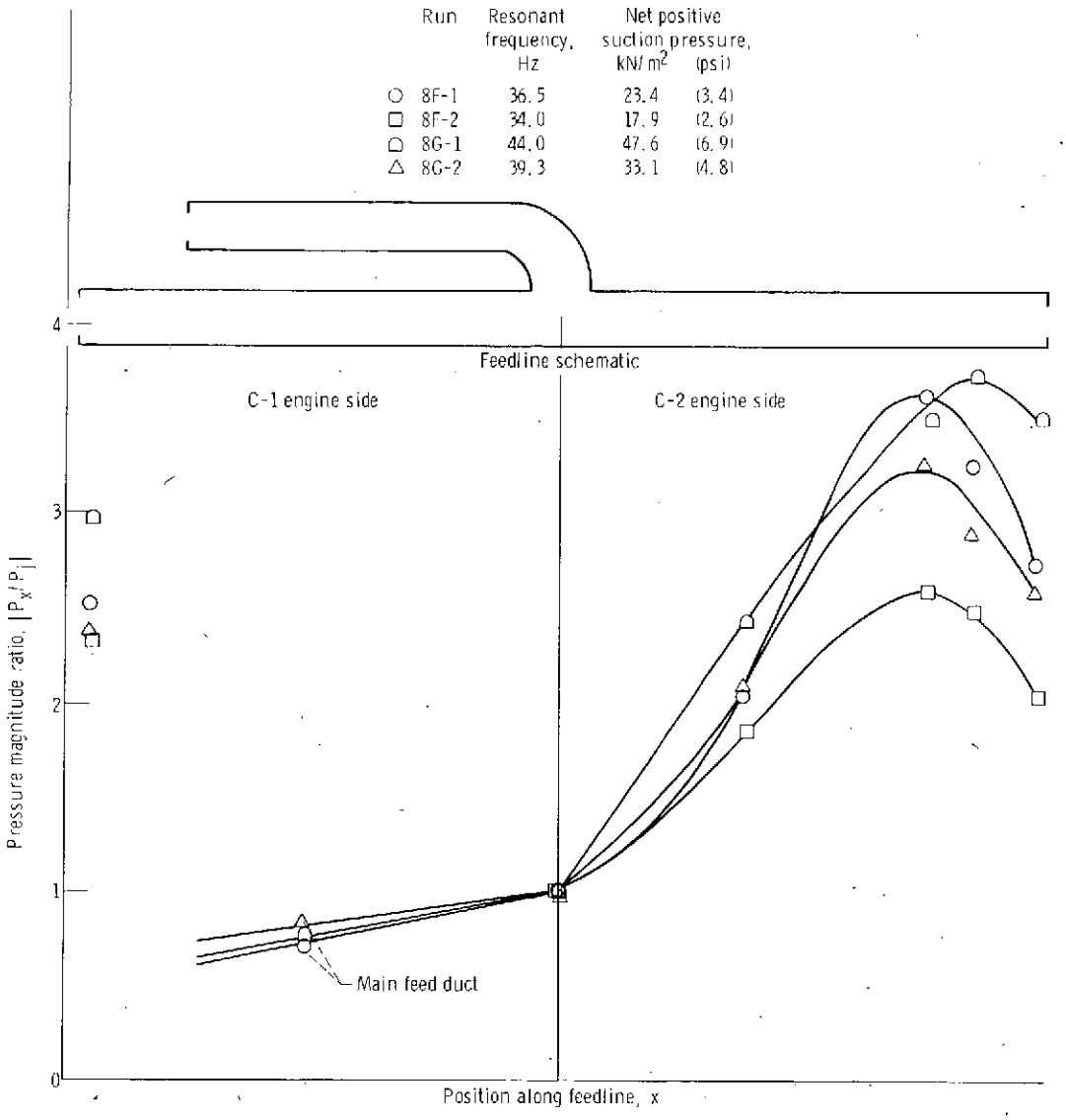

Figure 16. - Comparison of maximum pressure magnitude ratios at resonant frequencies - liquid-hydrogen feedline.

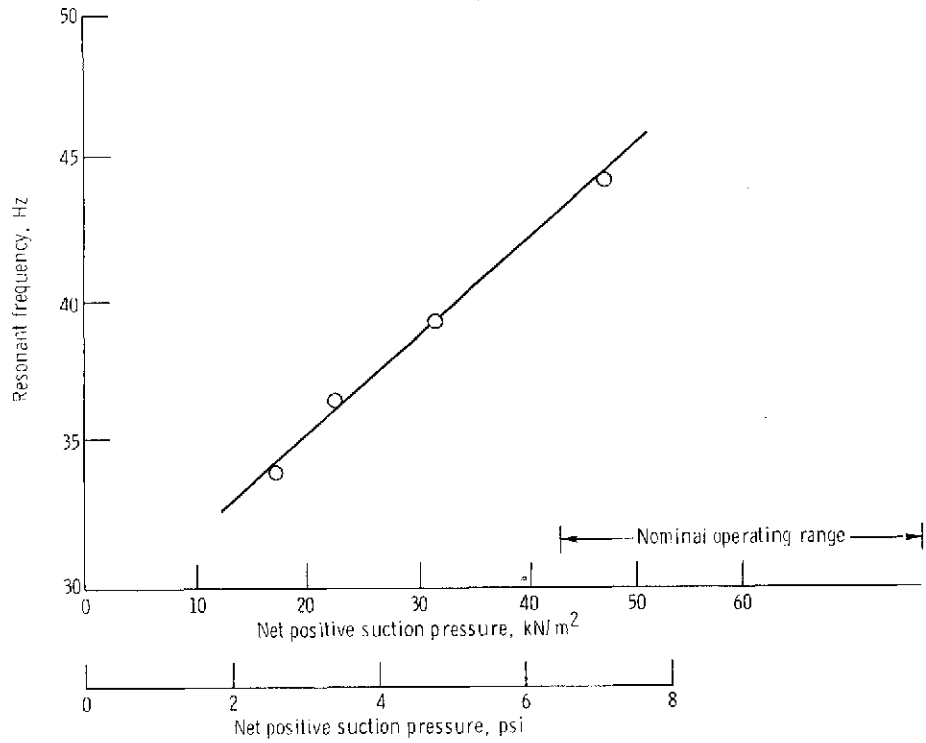

Figure 17. - Resonant frequency as a function of net positive suction pressure - liquid-hydrogen feedline.

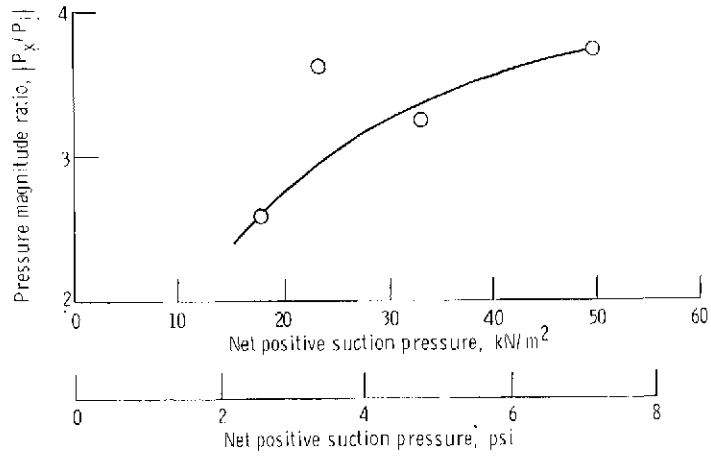

Figure 18. - Maximum pressure magnitude ratio as a function of net positive suction pressure - liquid-hydrogen feedline.

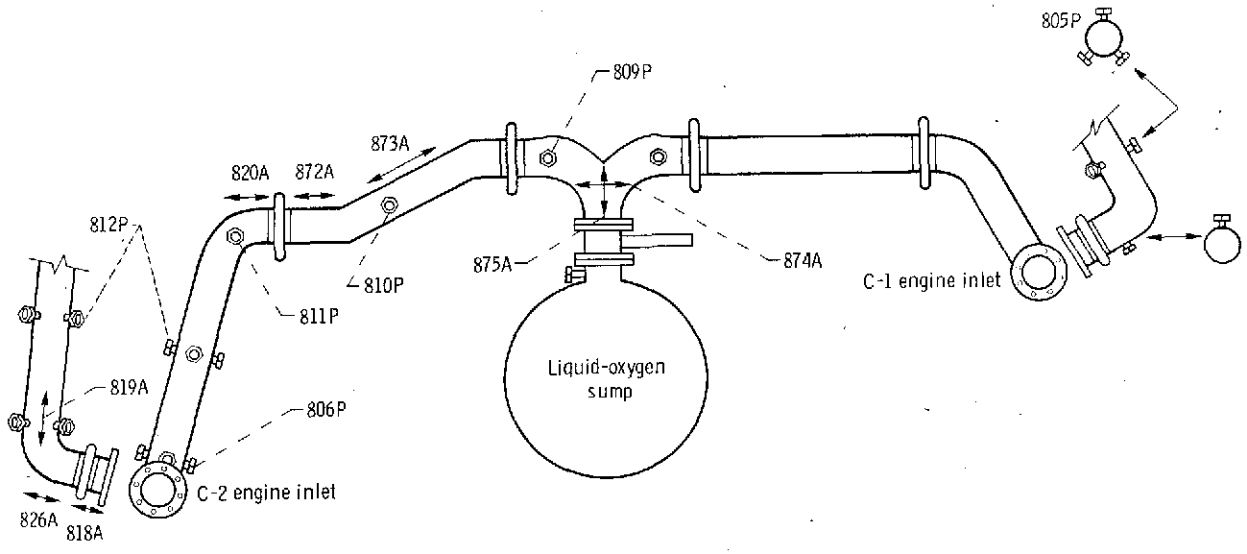

Figure 19. - Location of instrumentation on liquid-oxygen feedline for Centaur RL-10 dynamics tests in Plum Brook B-2 test facility. View looking forward.

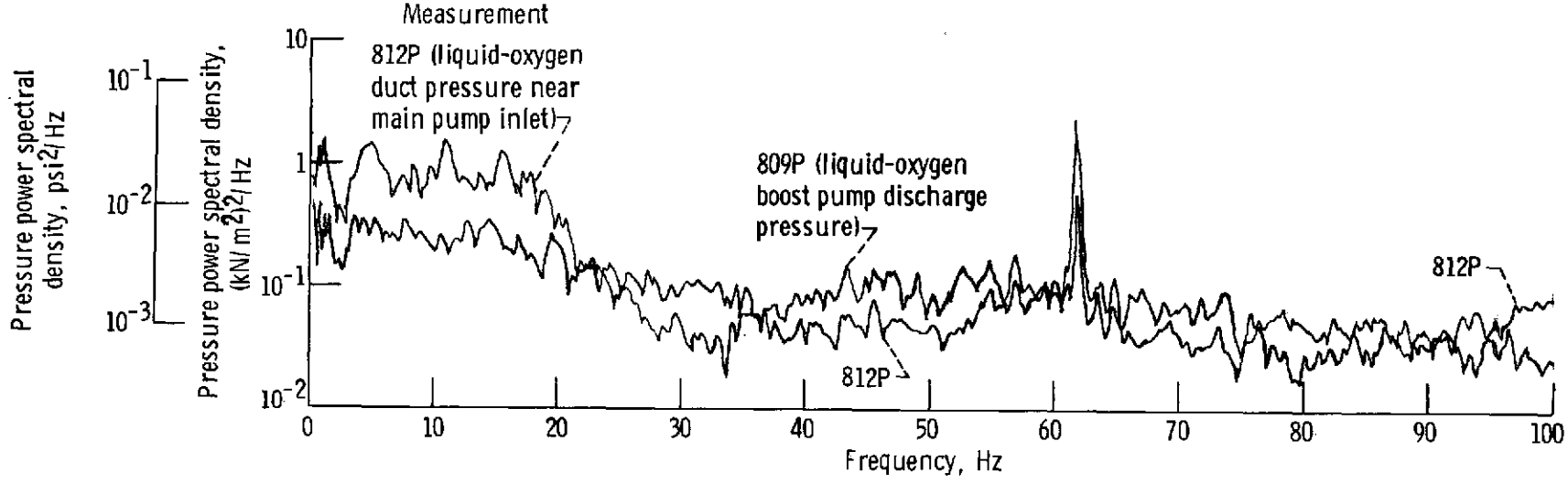

Figure 20. - Power spectral density of liquid-oxygen feedline at a net positive suction pressure of 154.0 kN/m^2 (22.3 psi) - run 8G-1.

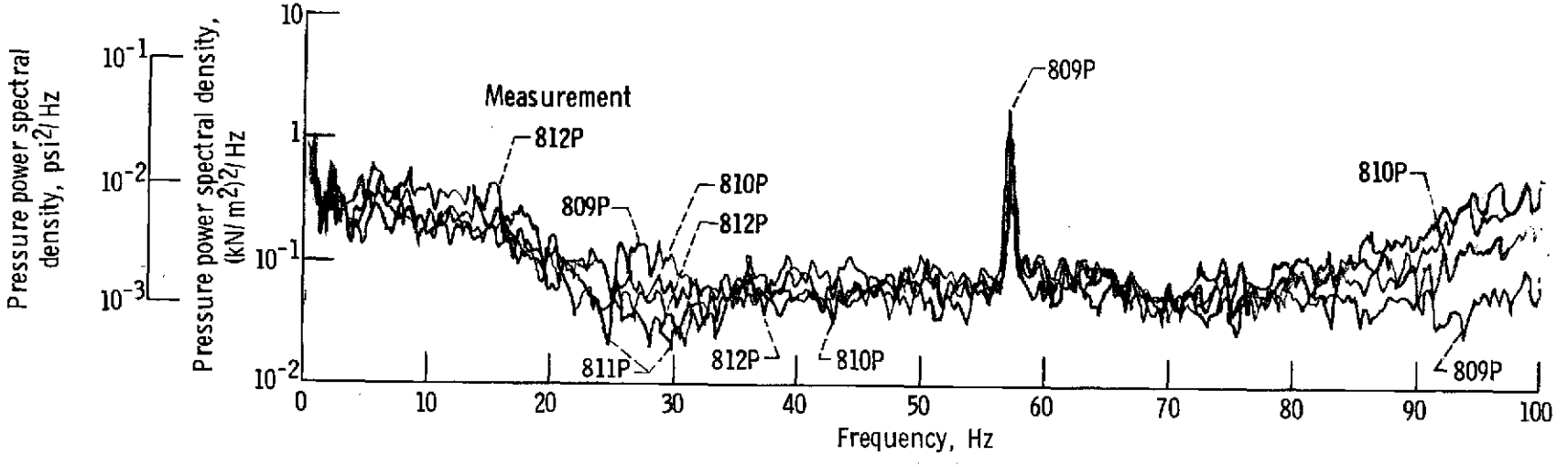

Figure 21. - Power spectral density of liquid-oxygen feedline at a net positive suction pressure of 98.5 kN/m^2 (14.3 psi) - run 8G-2.

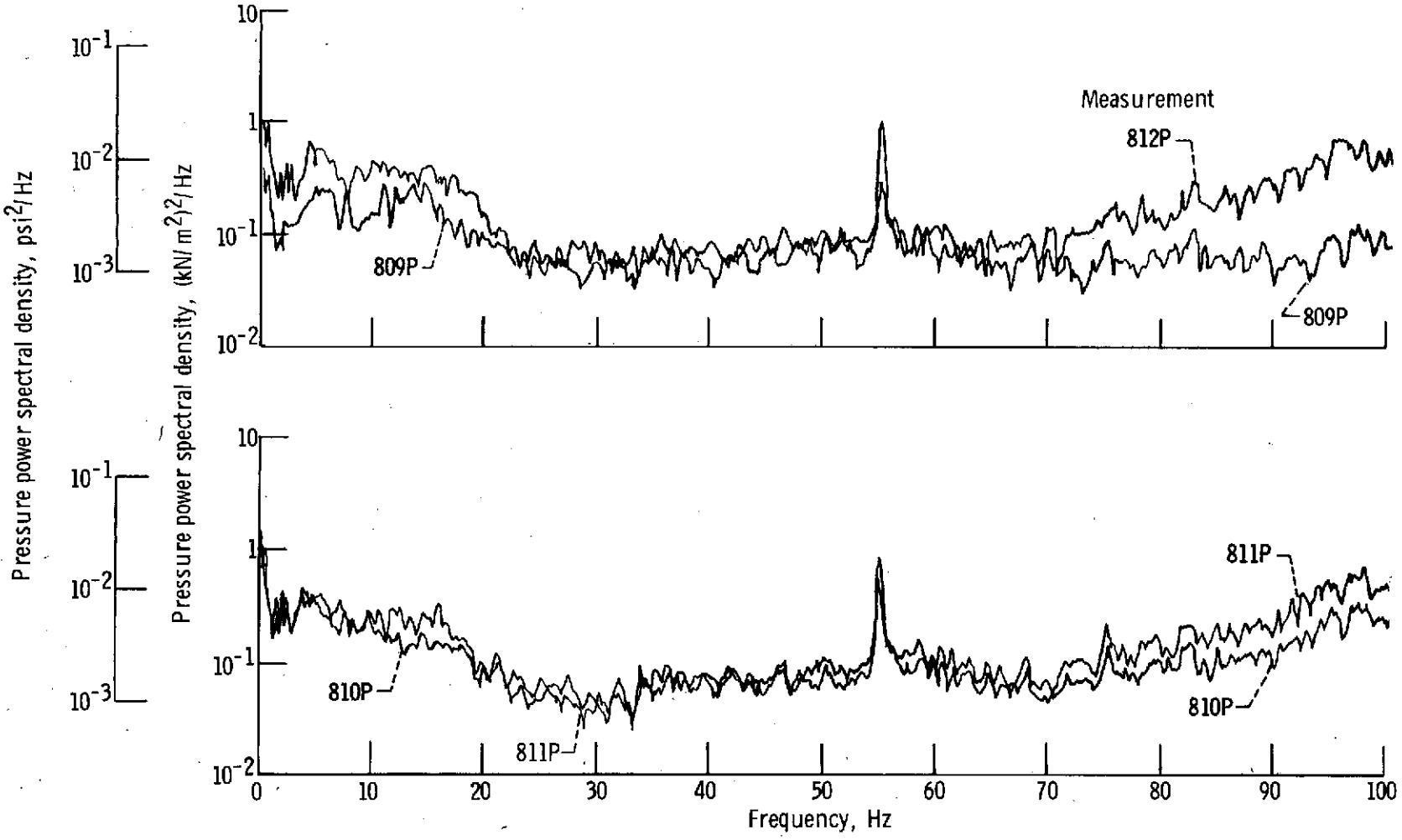

Figure 22. - Power spectral density of liquid-oxygen feedline at a net positive suction pressure of 78.3 kN/m^2 (11.3 psi) - run 8F-1.

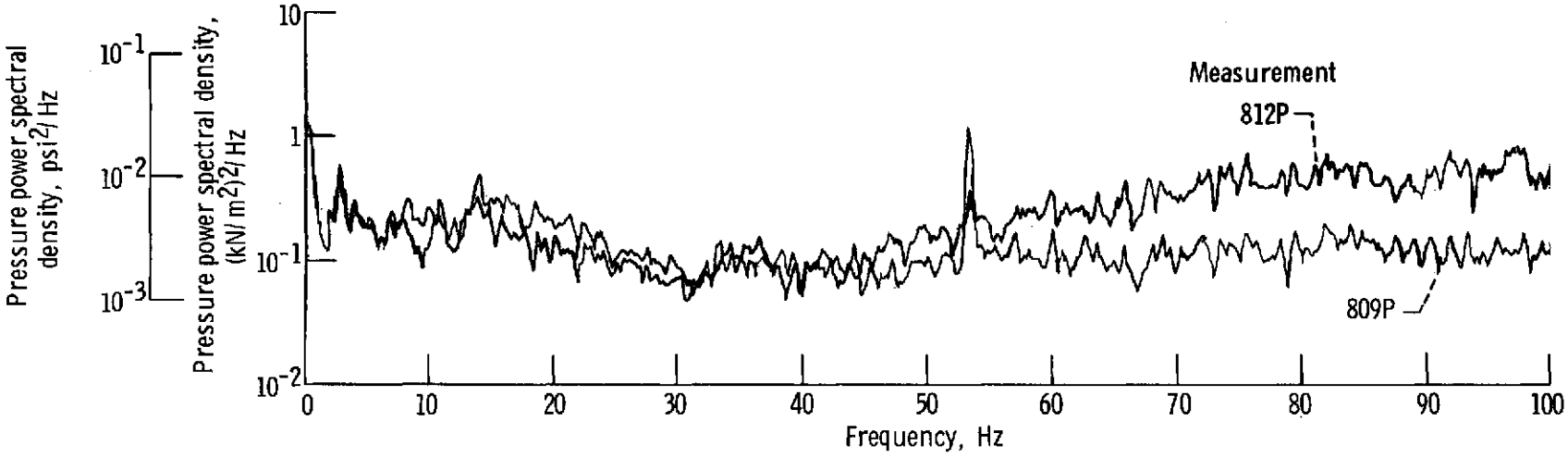

Figure 23. - Power spectral density of liquid-oxygen feedline at a net positive suction pressure of 55.9 kN/m^2 (8.1 psi) - run 8F-2.

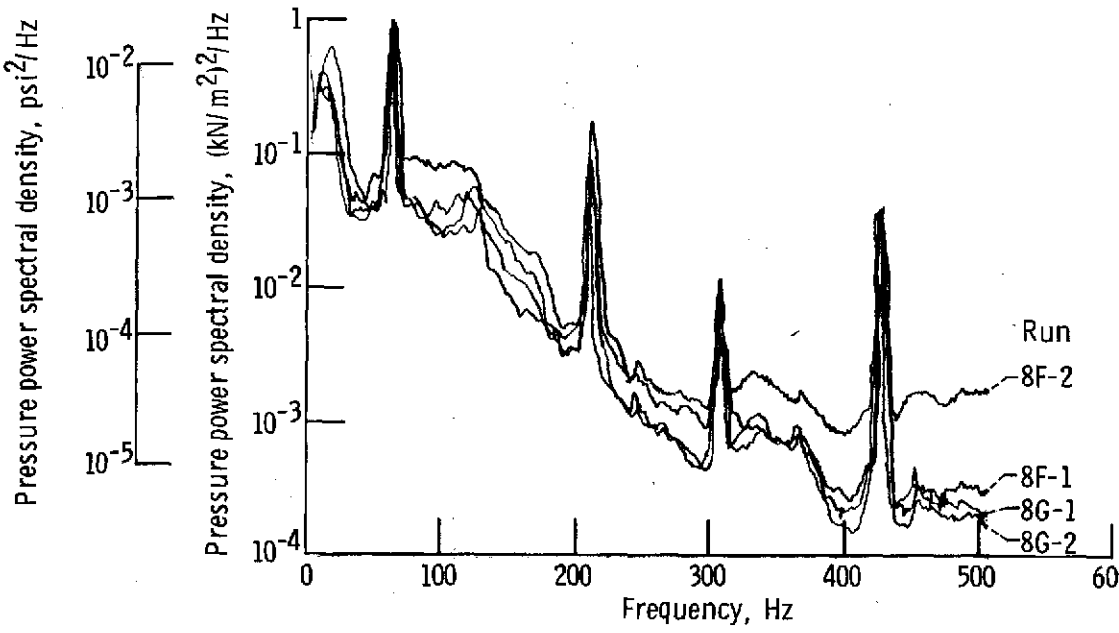

Figure 24. - Power spectral density of C-1 engine oxygen pump inlet pressure (805P).

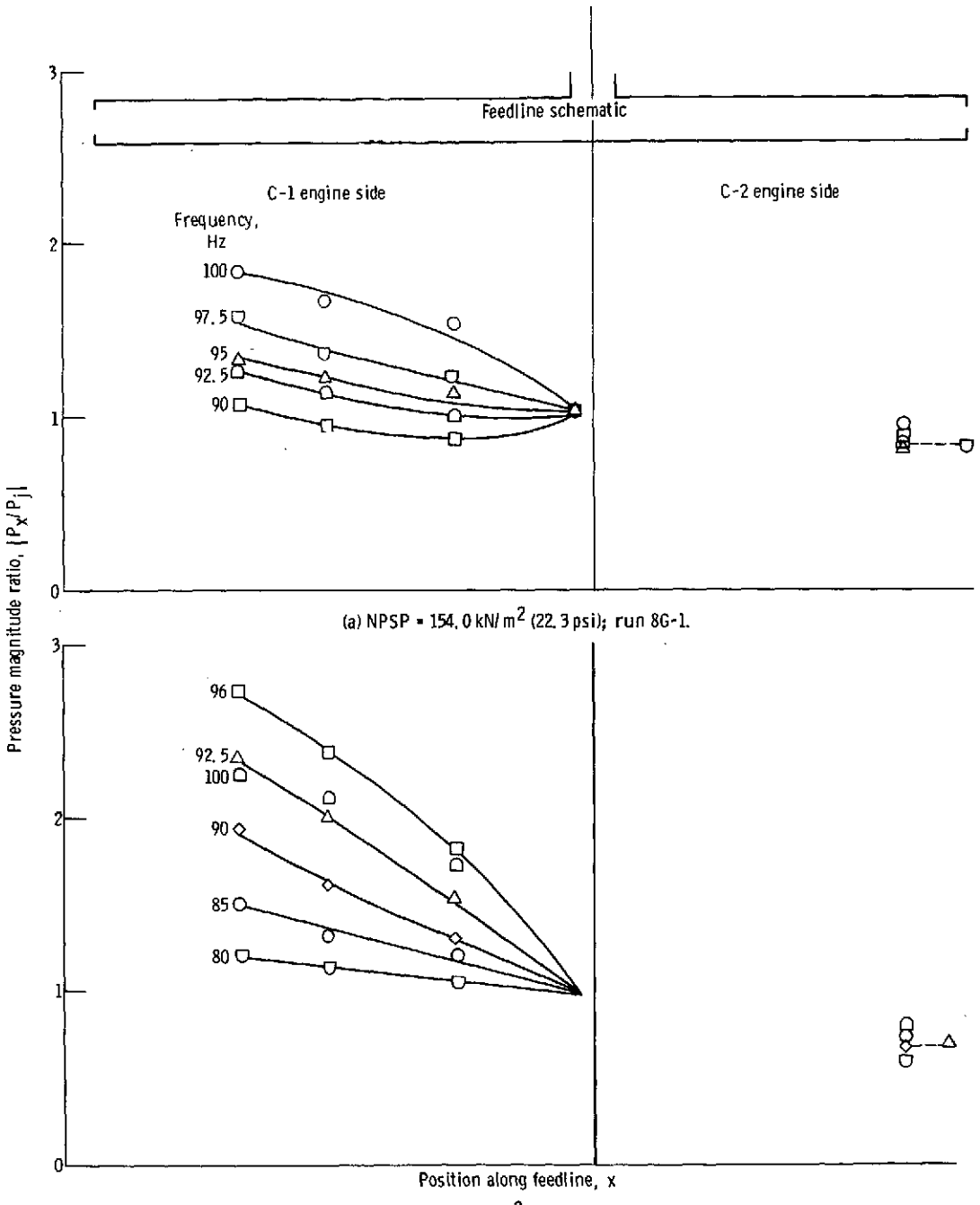

(a) NPSP = 154.0 kN/m^2 (22.3 psi); run 8G-1.

(b) NPSP = 98.5 kN/m^2 (14.3 psi); run 8G-2.

Figure 25. - Pressure magnitude ratio for liquid-oxygen feedline at various net positive suction pressures (NPSP).

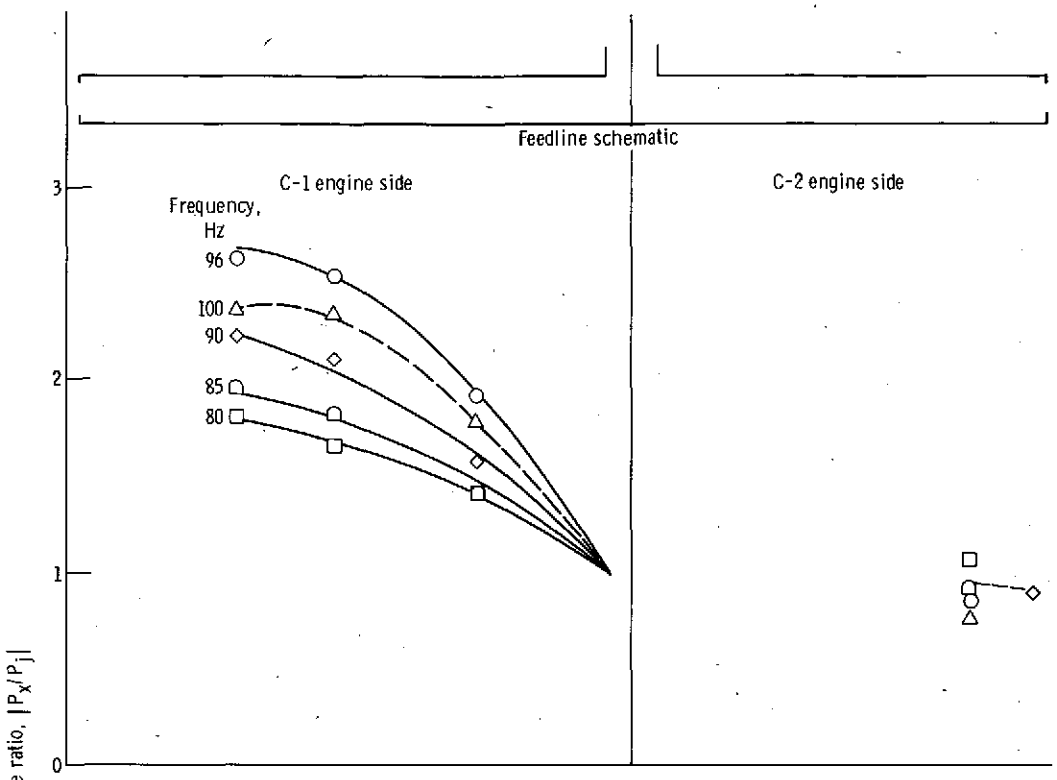

(c) NPSP = 78.3 kN/m^2 (11.3 psi); run 8F-1.

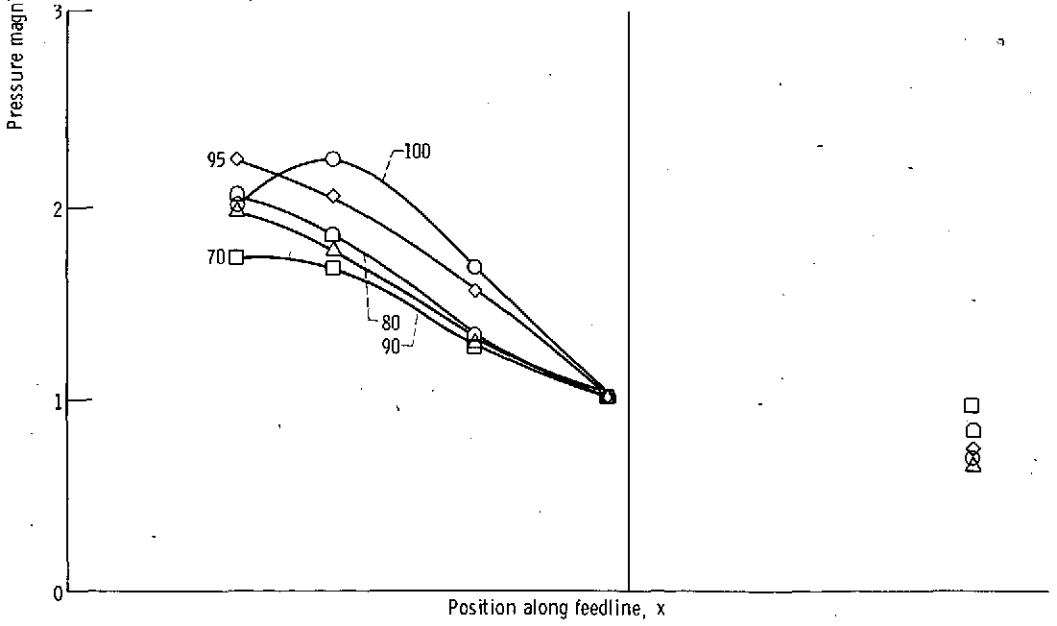

(d) NPSP = 55.9 kN/m^2 (8.1 psi); run 8F-2.

Figure 25. - Concluded.

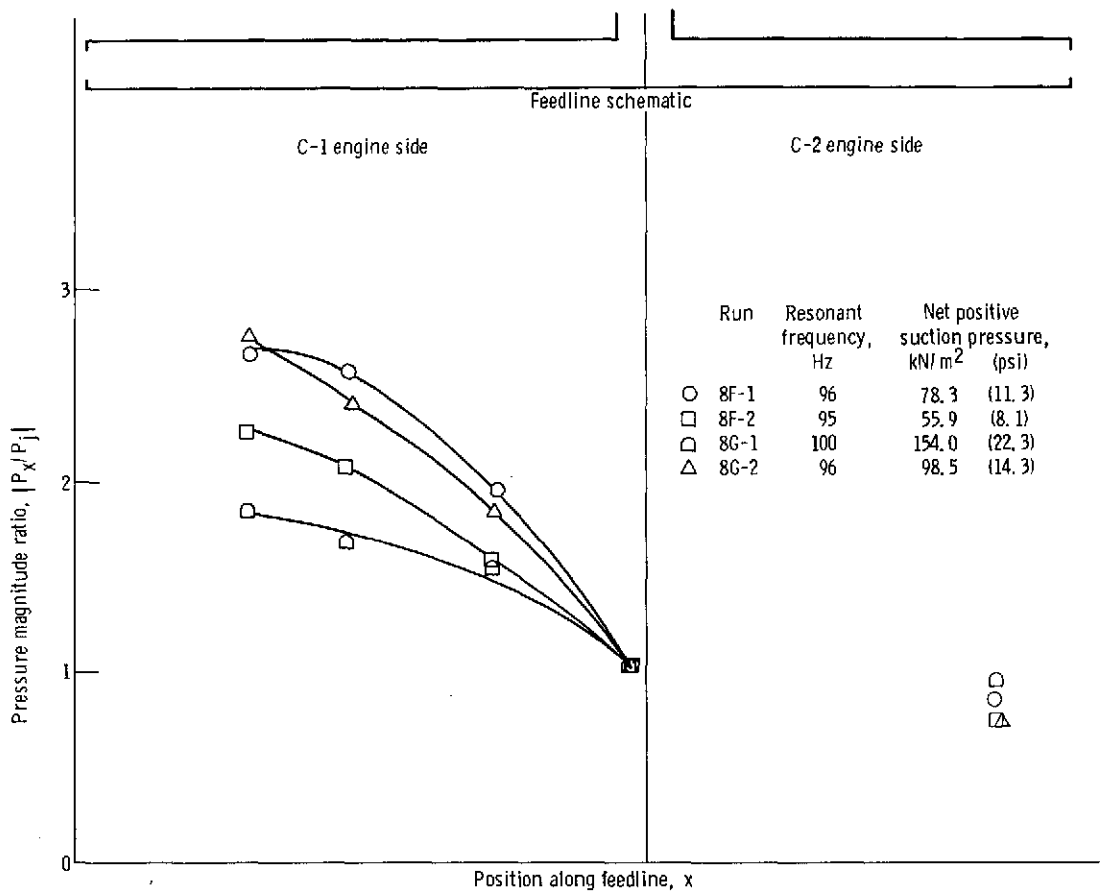

Figure 26. - Comparison of maximum pressure magnitude ratios at resonant frequencies - liquid-oxygen feedline.

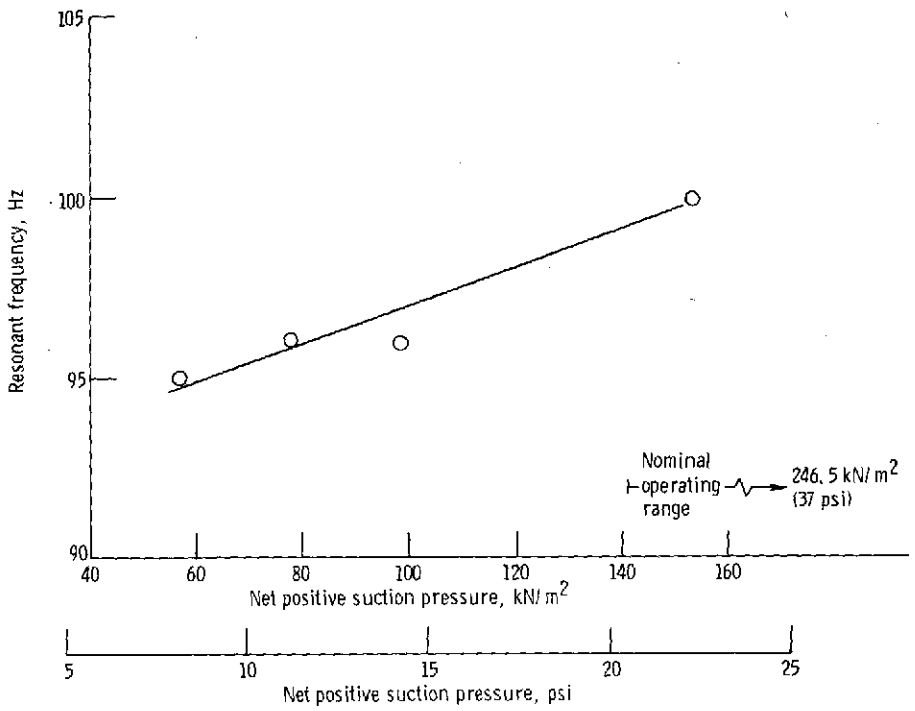

Figure 27. - Resonant frequency as function of net positive suction pressure - liquid-oxygen feedline.

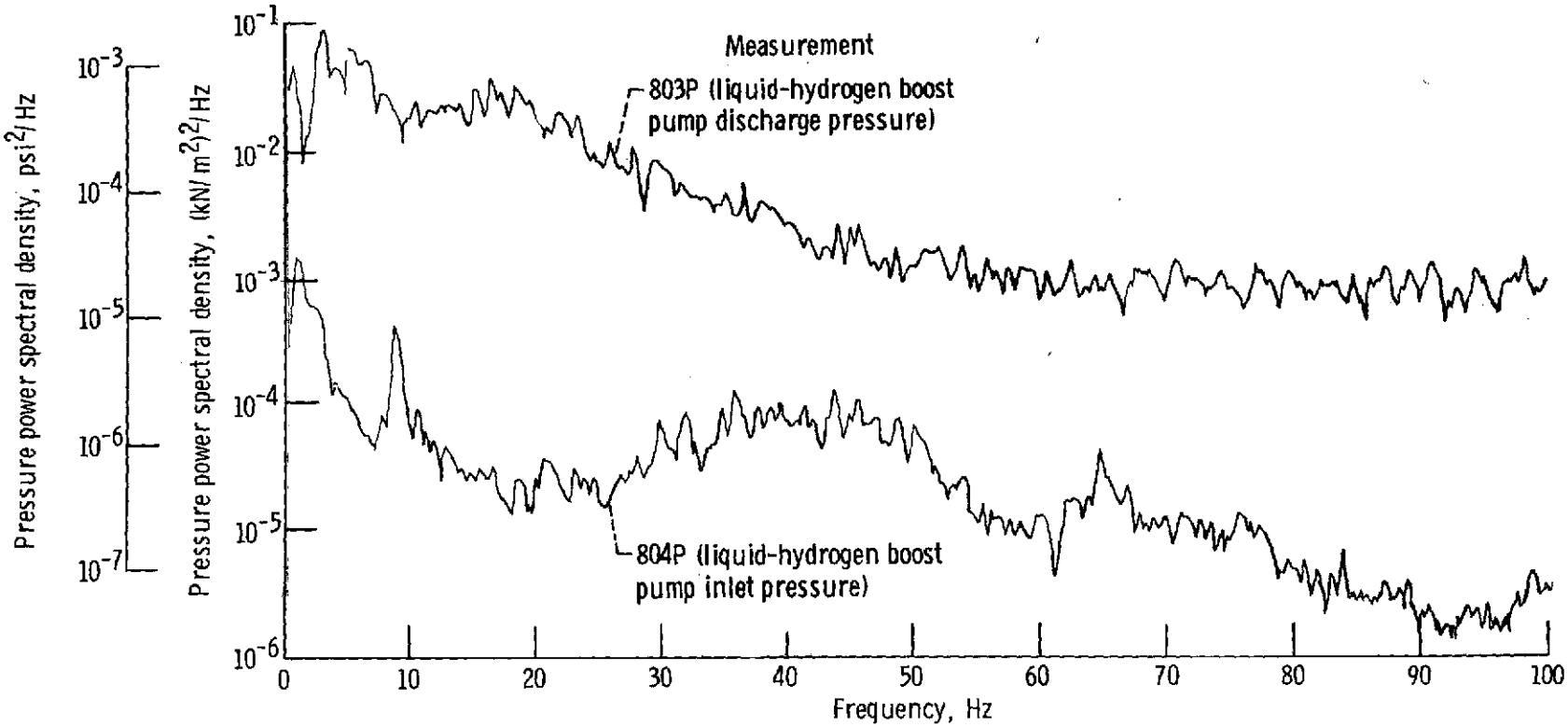

Figure 28. - Power spectral density of liquid-hydrogen boost pump at a net positive suction pressure of 33.1 kN/m^2 (4.8 psi) - run 8G-2.

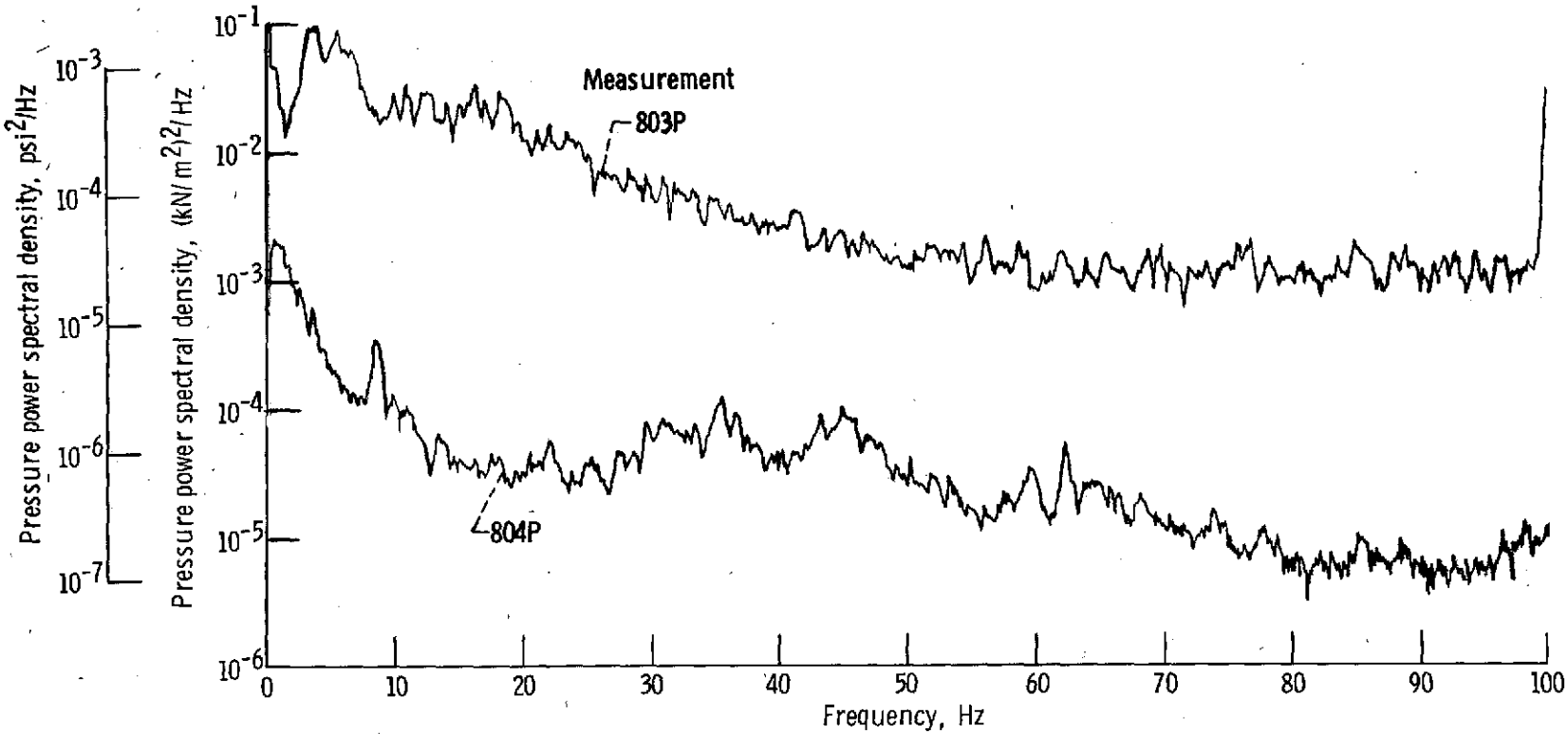

Figure 29. - Power spectral density of liquid-hydrogen boost pump at a net positive suction pressure of 17.9 kN/m^2 (2.6 psi) - run 8F-2.

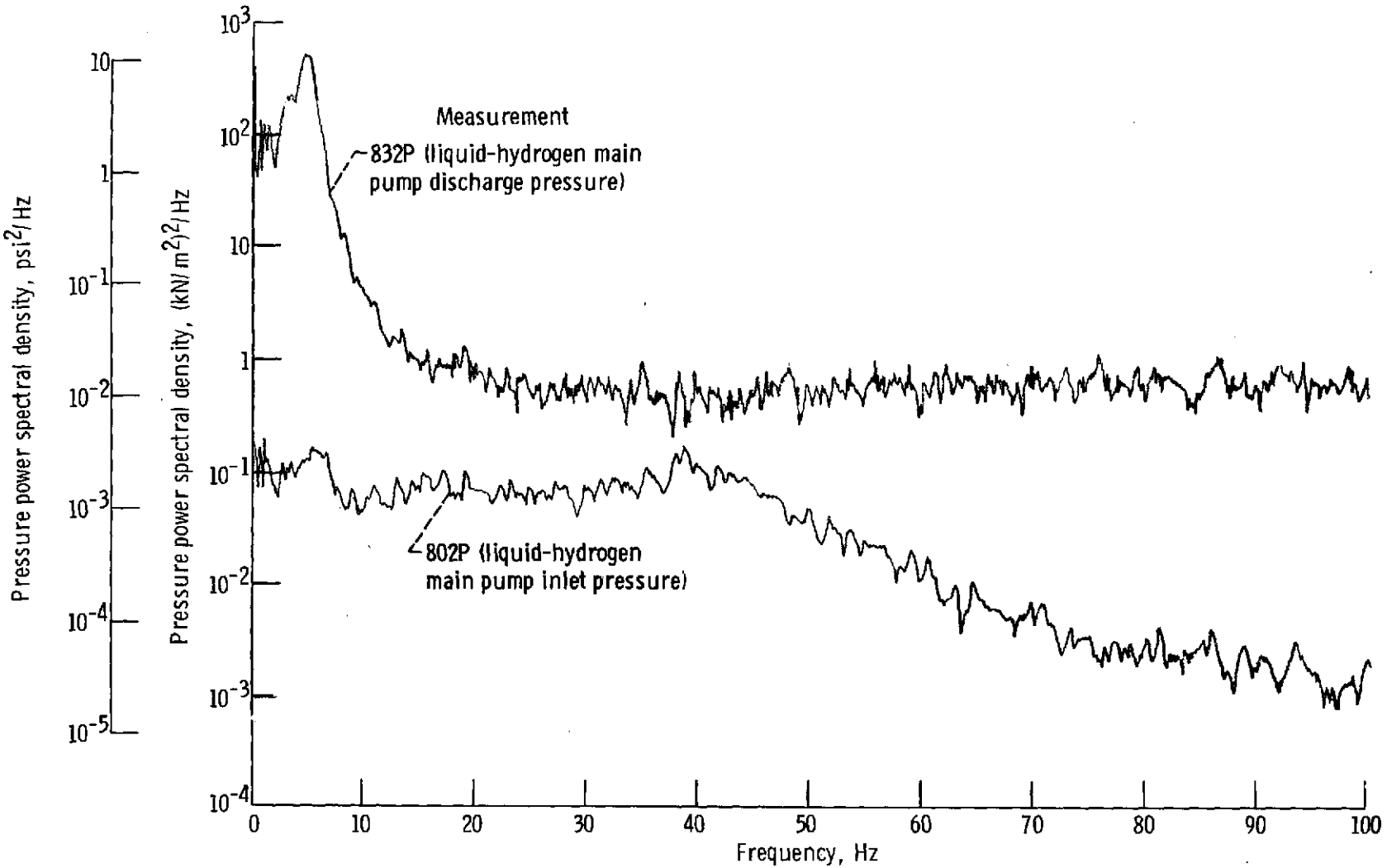

Figure 30. - Power spectral density of liquid-hydrogen main pump at a net positive suction pressure of 47.6 kN/m^2 (6.9 psi) - run 8G-1.

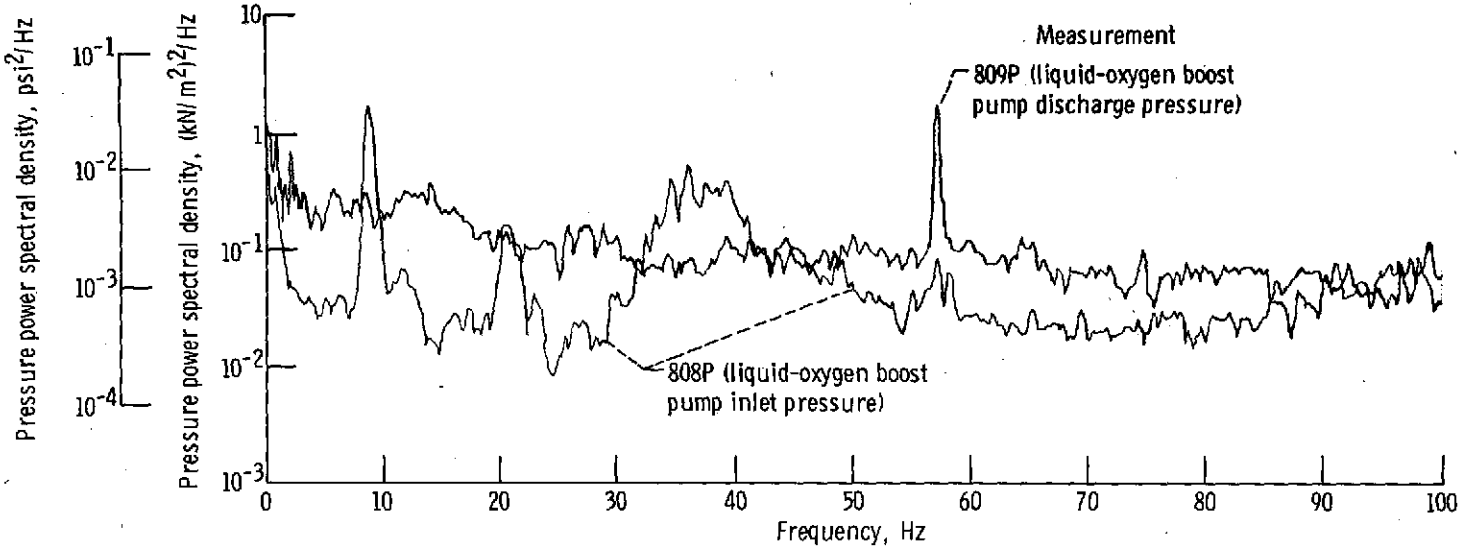

Figure 31. - Power spectral density of liquid-oxygen boost pump at a net positive suction pressure of 98.5 kN/m^2 (14.3 psi) - run 8G-2.

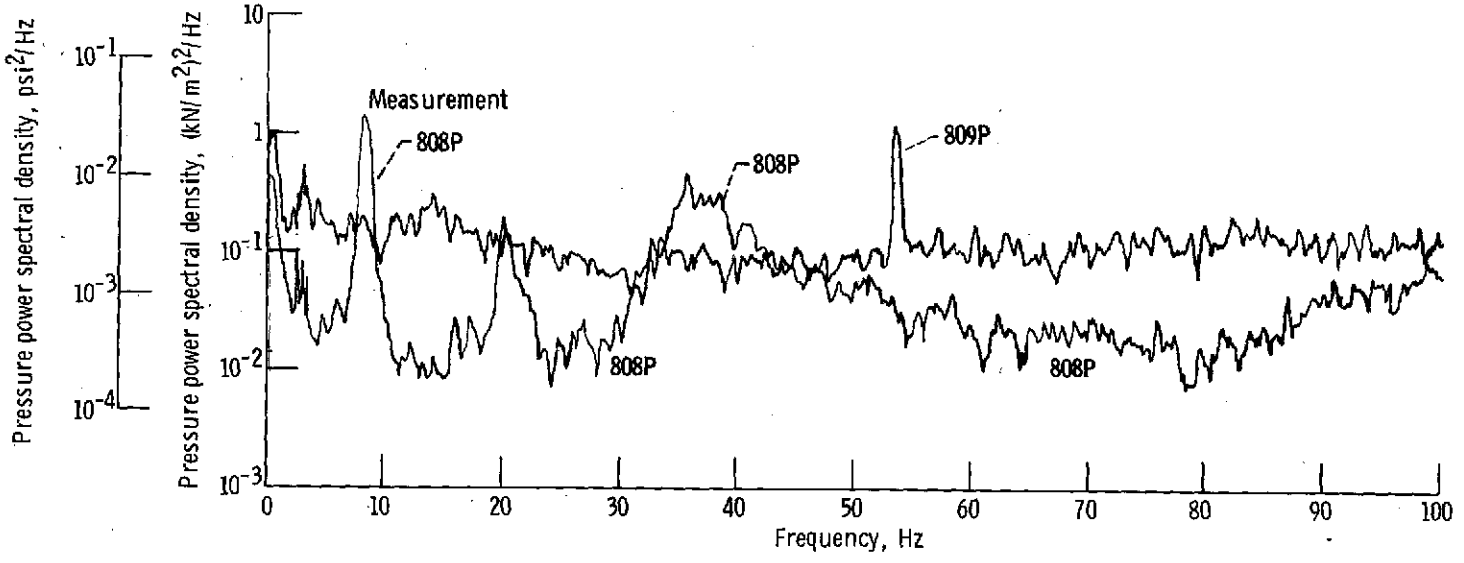

Figure 32. - Power spectral density of liquid-oxygen boost pump at net positive suction pressure of 55.9 kN/m^2 (8.1 psi) - run 8F-2.

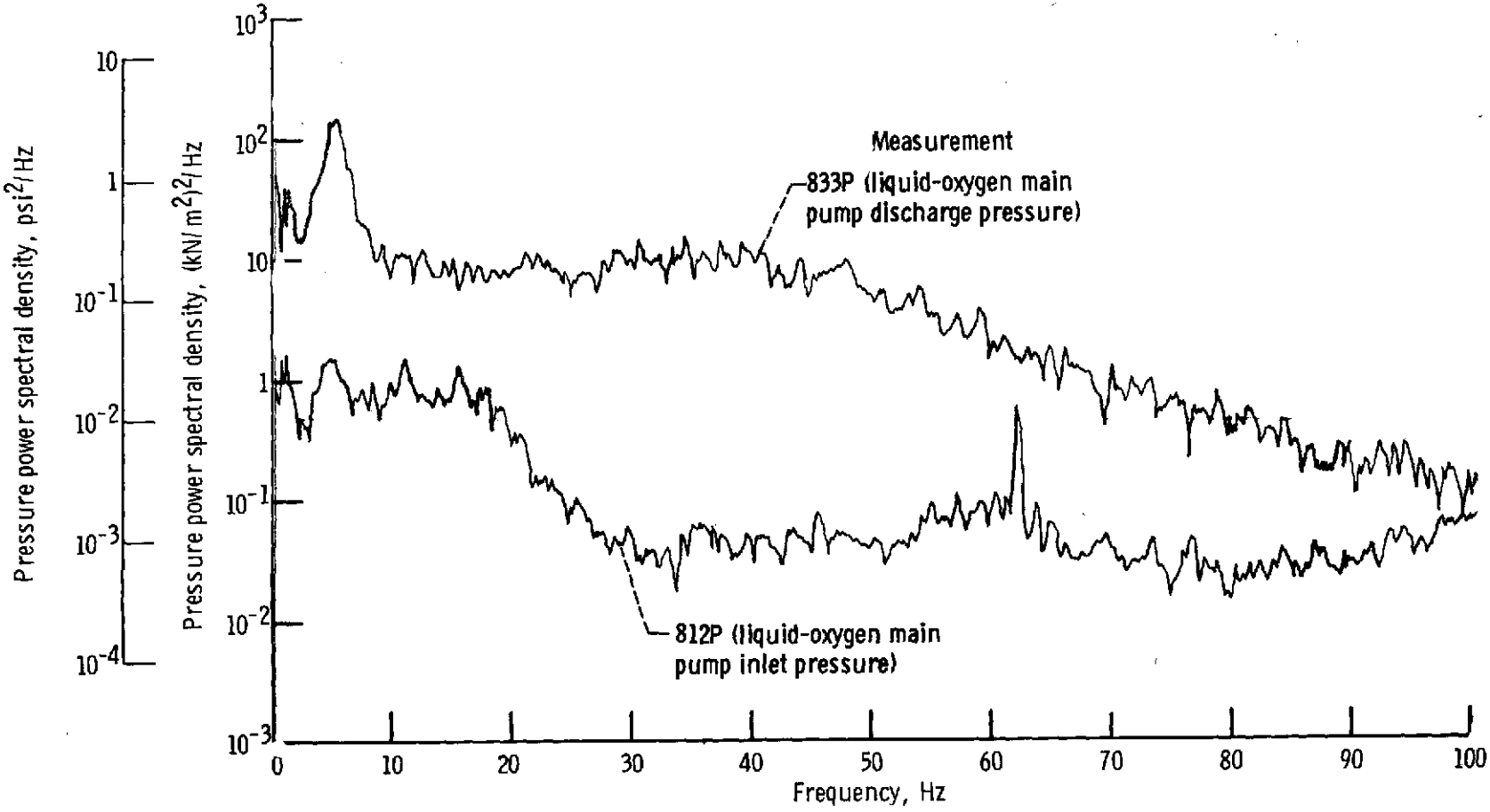

Figure 33. - Power spectral density of liquid-oxygen main pump at a net positive suction pressure of 154.0 kN/m^2 (22.3 psi) - run 8G-1.

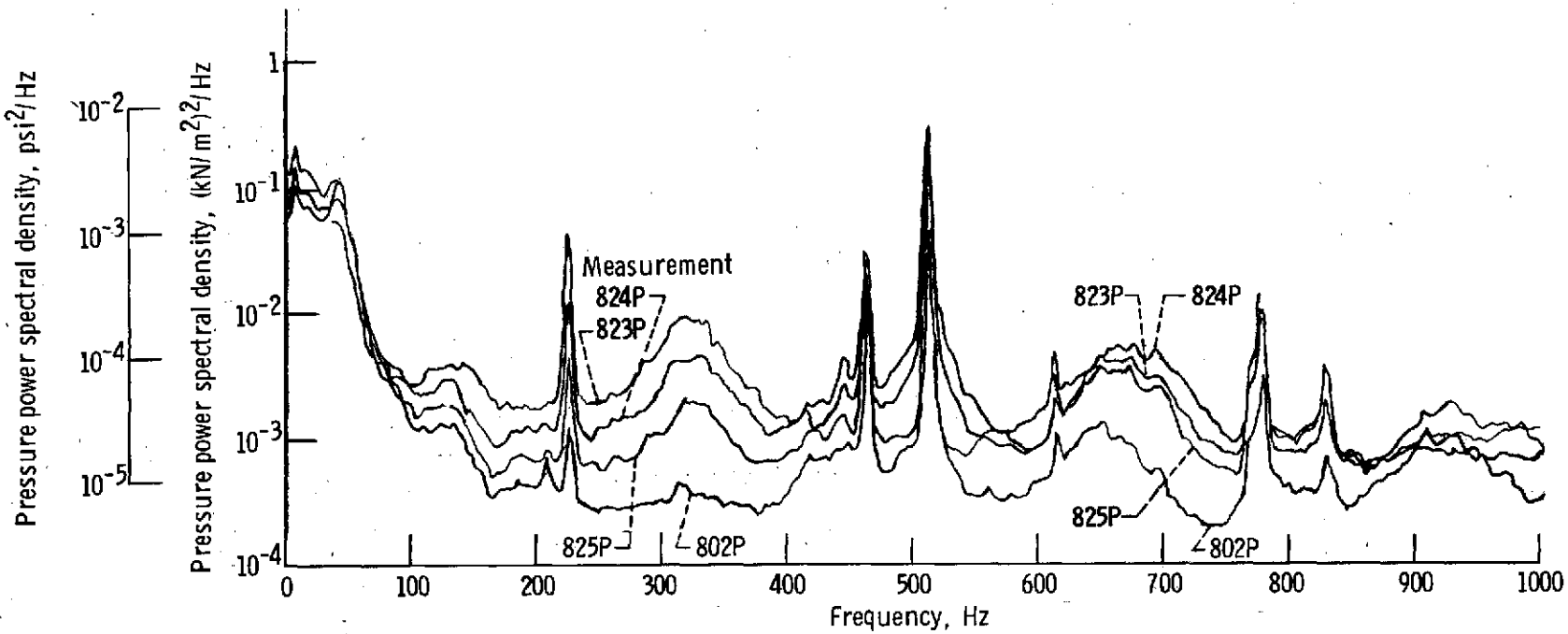

Figure 34. - Power spectral density of liquid-hydrogen feedline at high frequencies - run 8E-1.

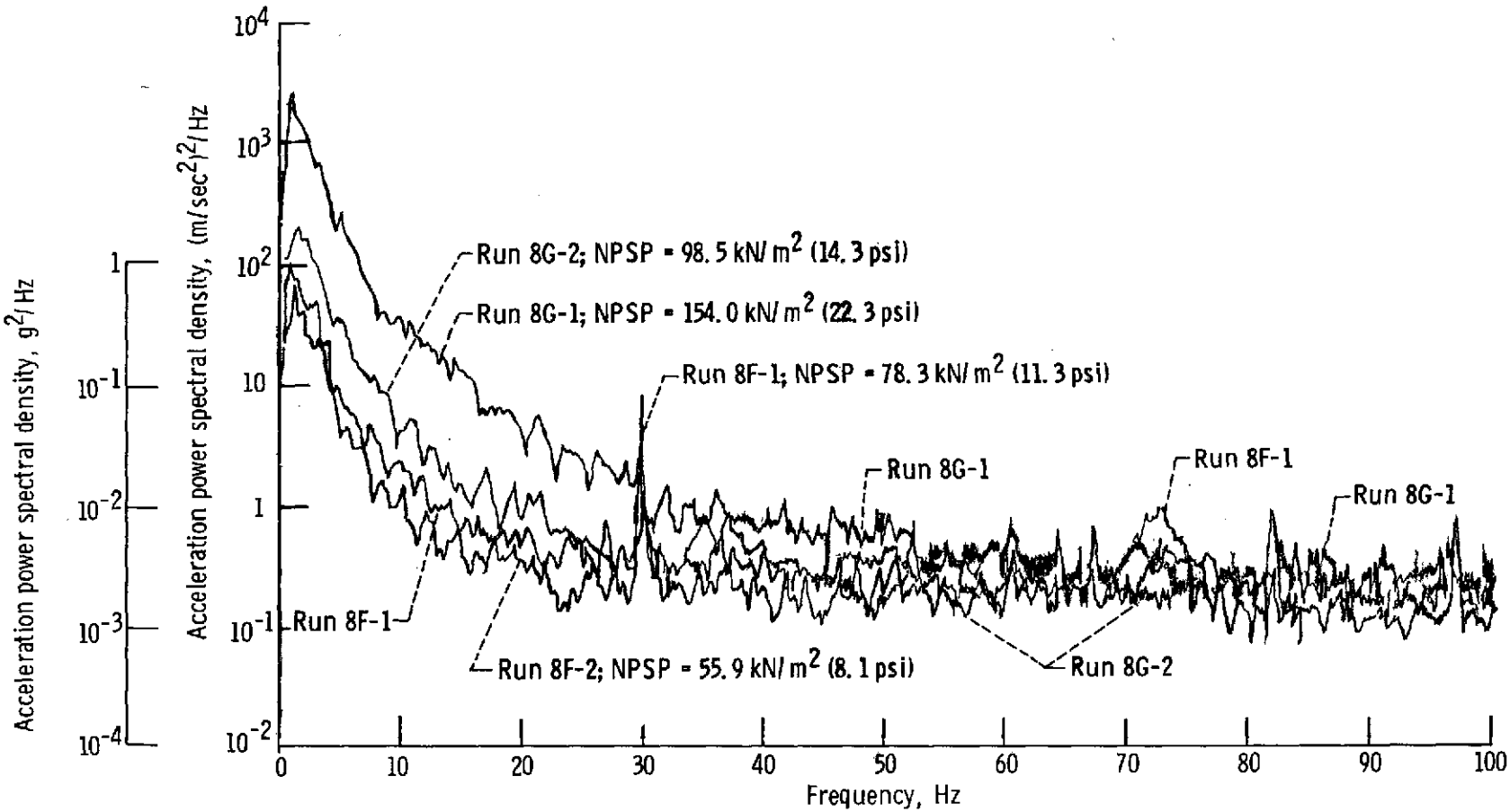

Figure 35. - Power spectral density of liquid-oxygen feedline acceleration and liquid-oxygen pump face acceleration at various net positive suction pressures.

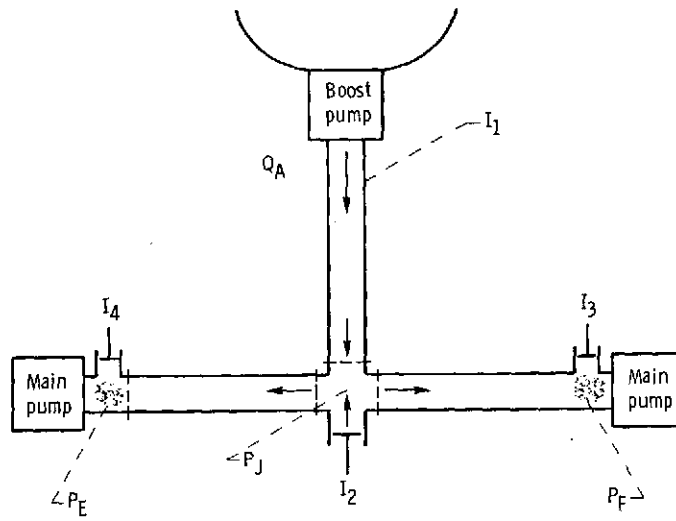

Figure 36. - Diagram of hydrogen feedline configuration used as basis for analytical model.

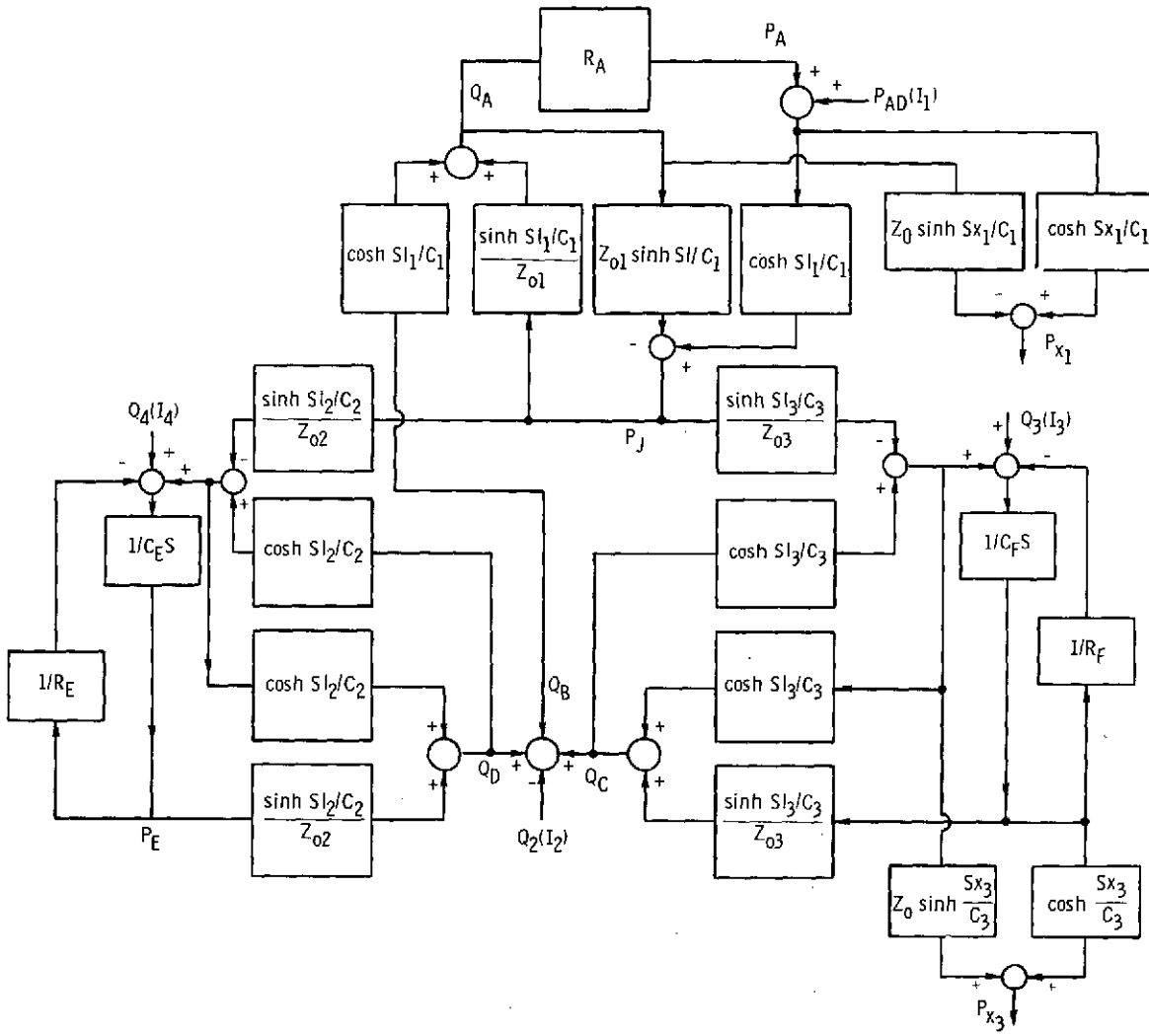

Figure 37. - Block diagram of hydrogen feedline.

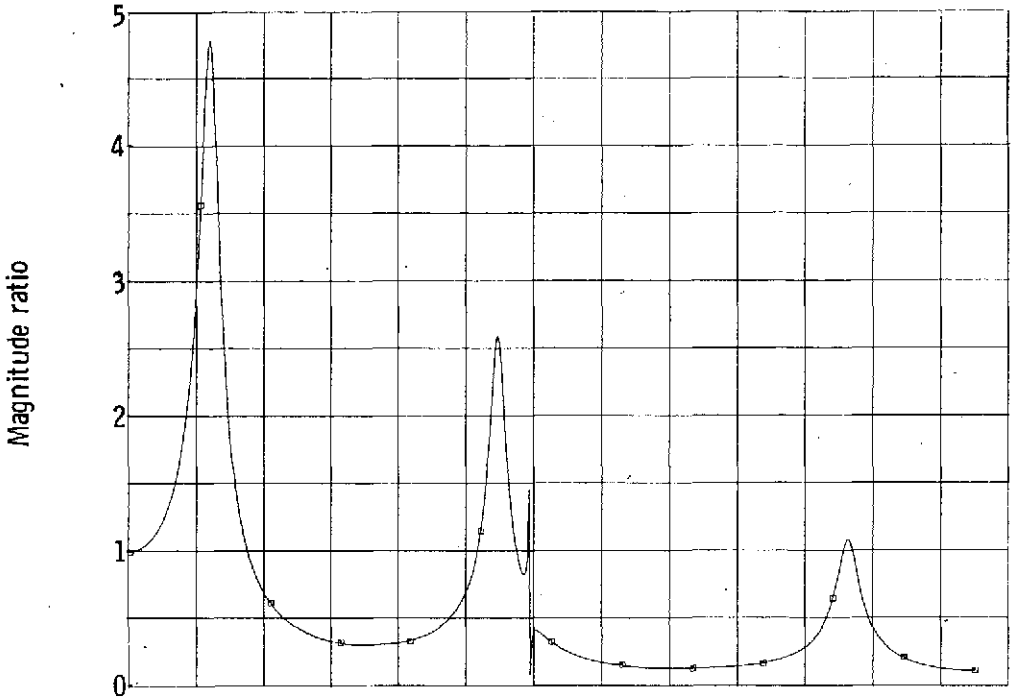

(a) Magnitude ratio.

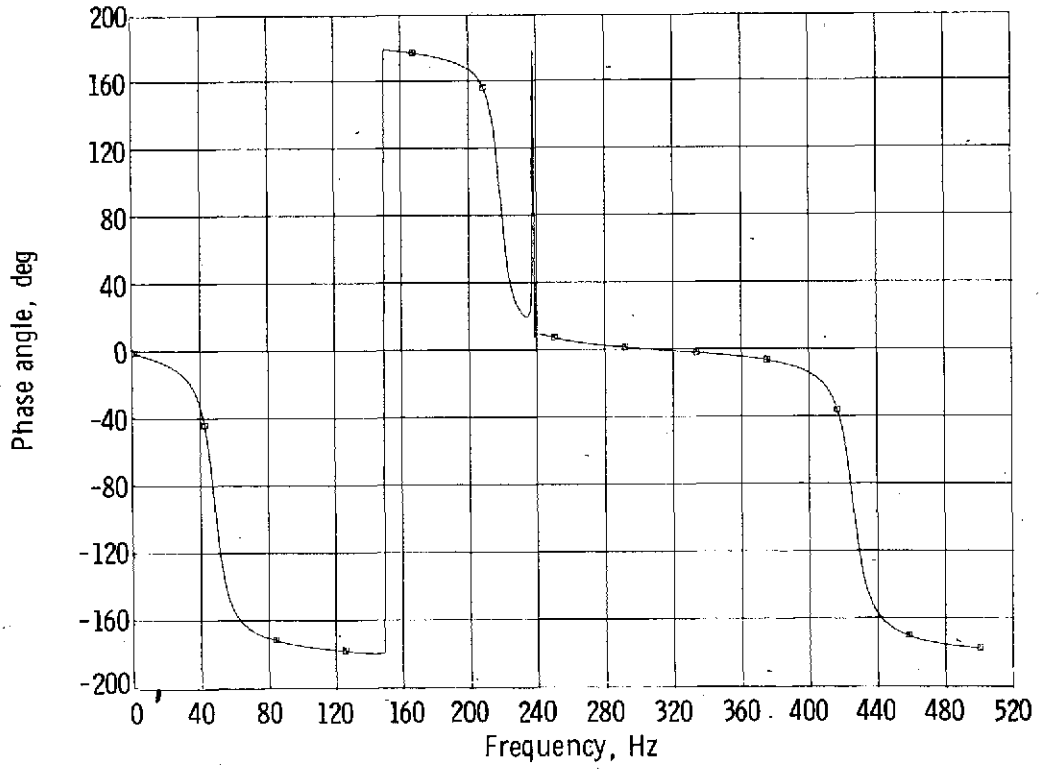

(b) Phase angle.

Figure 38. - Hydrogen feedline frequency response P_F/Q_J - driving at I_2.

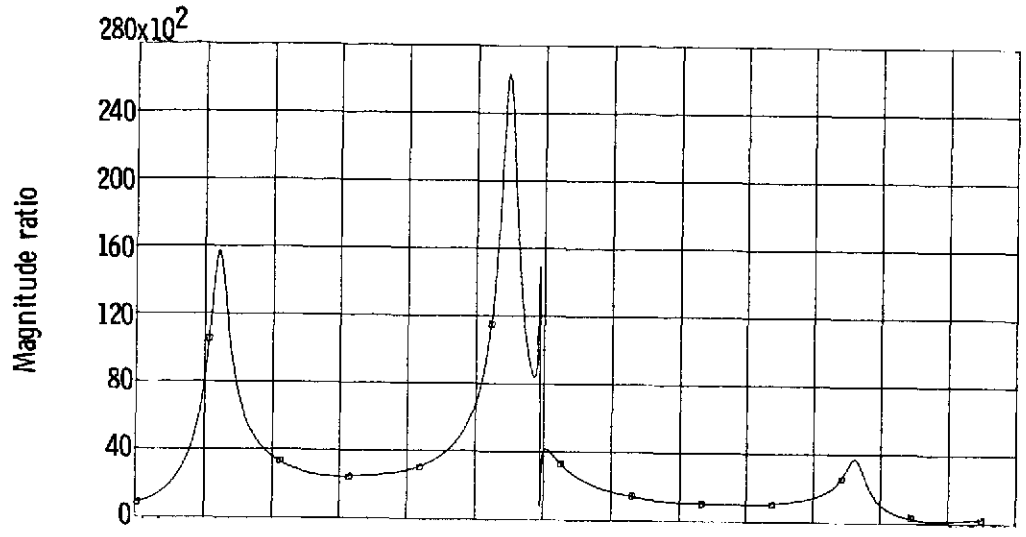

(a) Magnitude ratio.

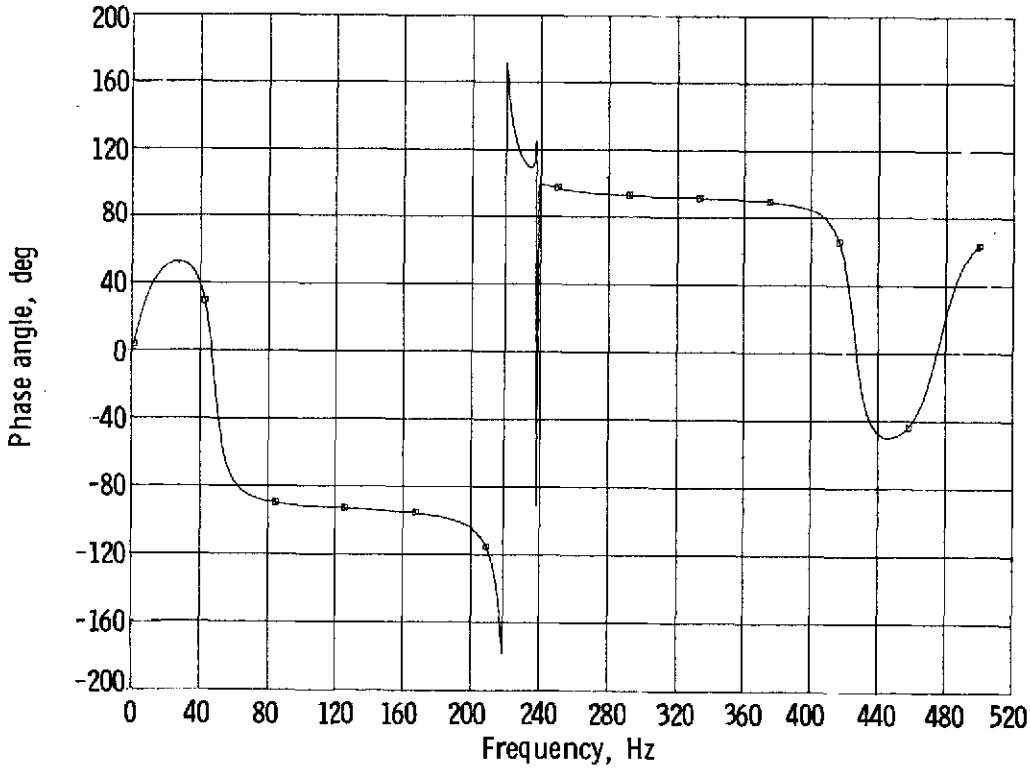

(b) Phase angle.

Figure 39. - Hydrogen feedline frequency response P_F/Q_J - driving at I_2.

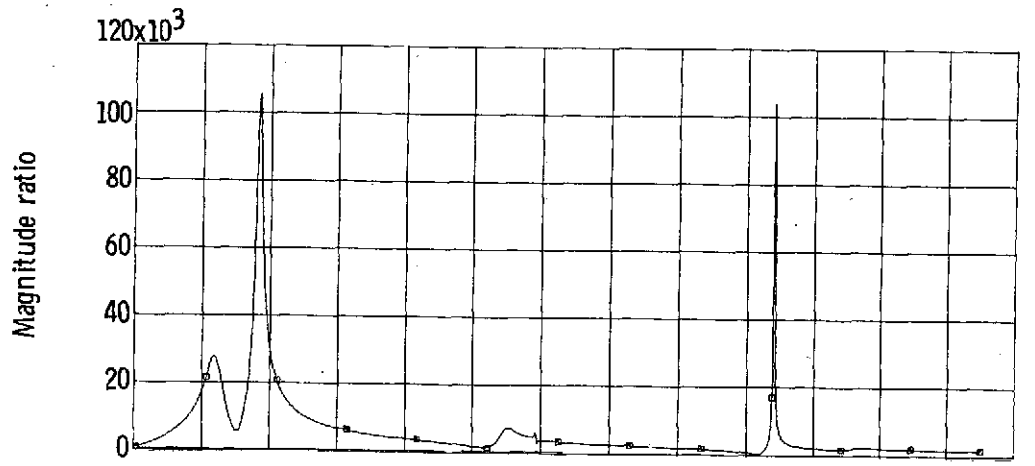

(a) Magnitude ratio.

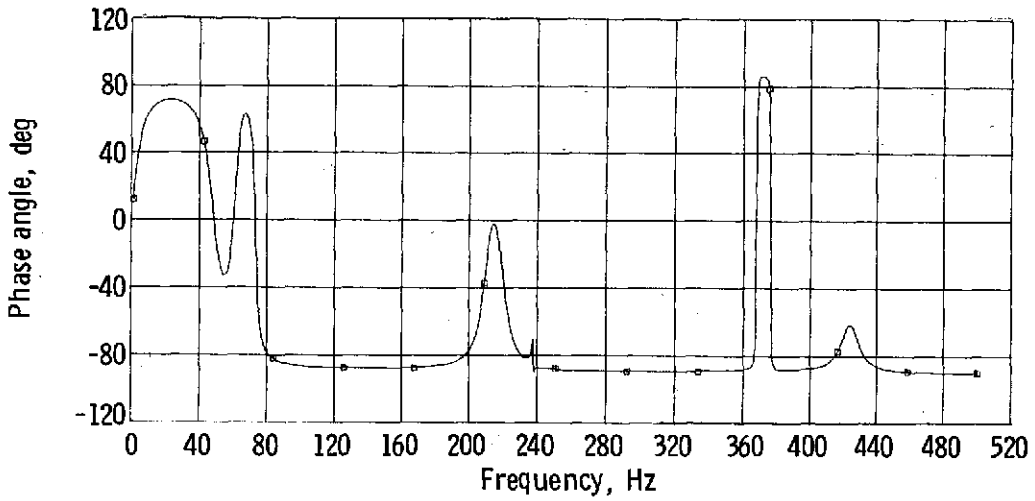

(b) Phase angle.

Figure 40. - Hydrogen feedline frequency response P_F/Q_3 - driving at I_3.

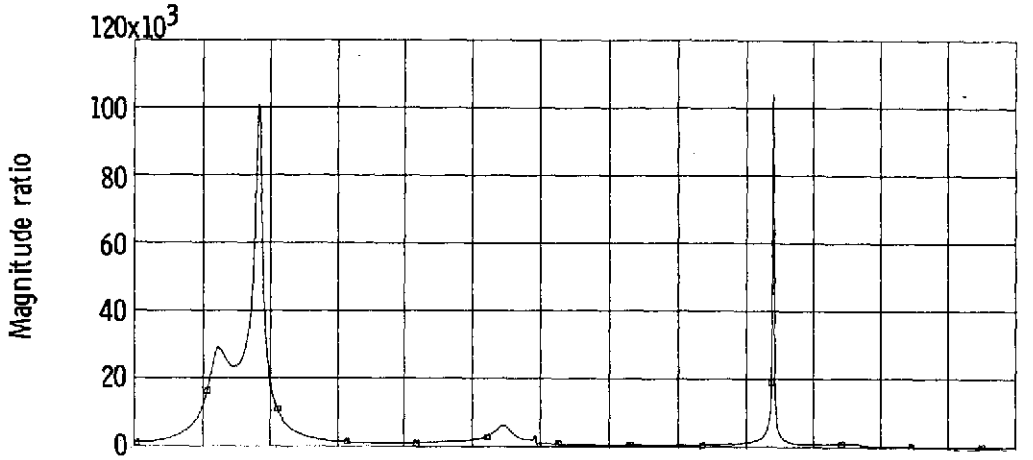

(a) Magnitude ratio.

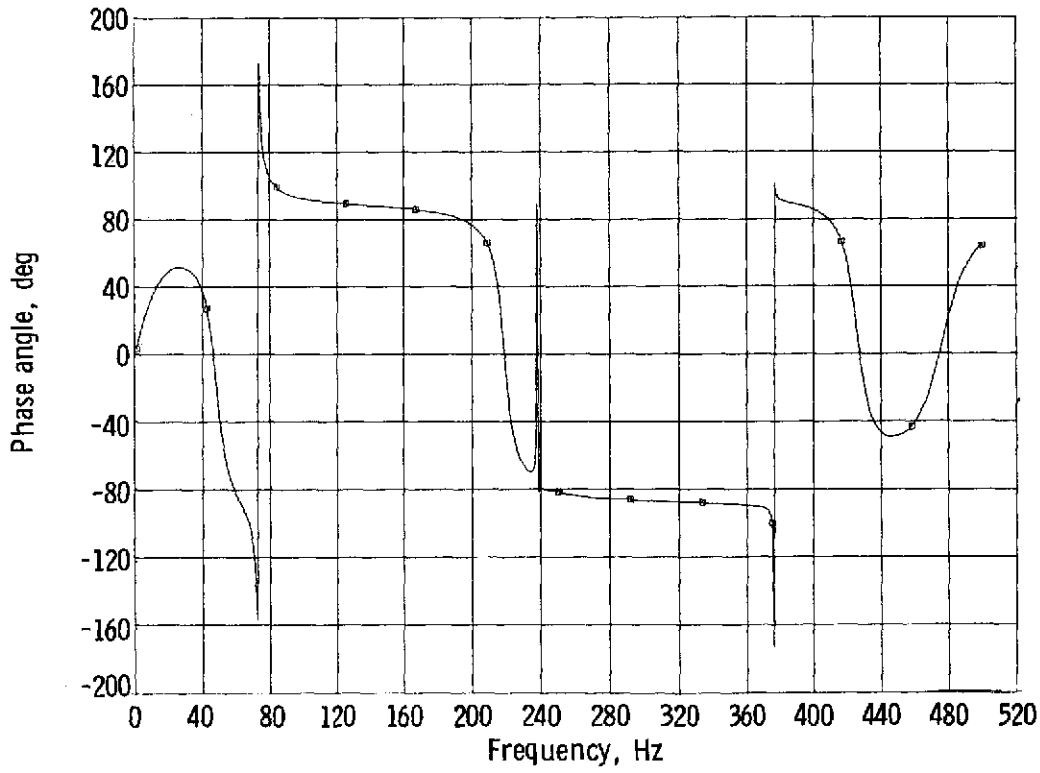

(b) Phase angle.

Figure 41. - Hydrogen feedline frequency response P_F/Q_4 - driving at I_4.

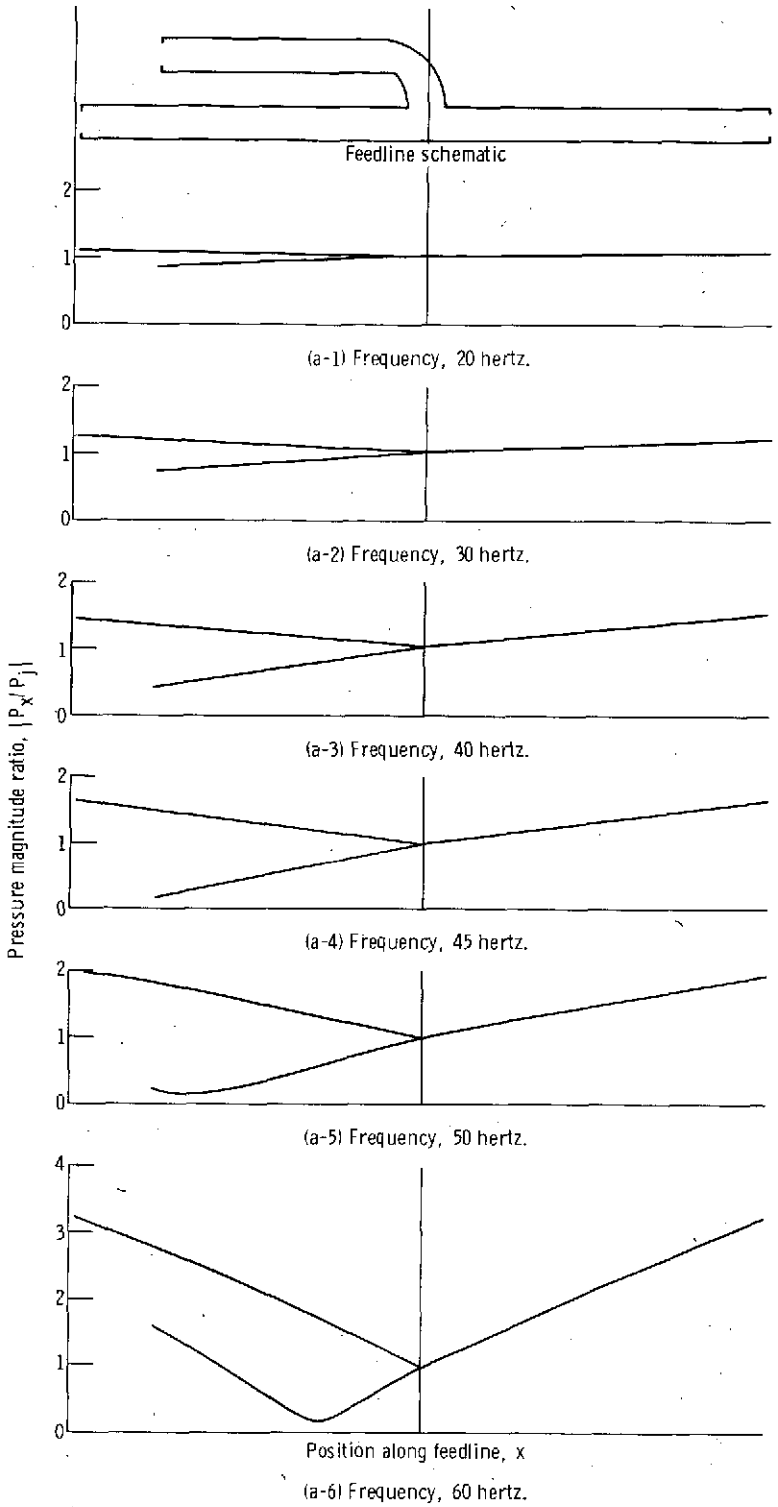

(a) Symmetrical response of system for frequency steps between 20 and 70 hertz.

Figure 42. - Pressure magnitude ratio - hydrogen feedline driving at I_1.
$R_A = 1.5 \times 10^6$ N-sec/m^5 (885 lbf-sec/ft^5); $R_E = 3.56 \times 10^8$ (2.1$\times 10^5$ lbf-sec/ft^5);
$C_E = 118 \times 10^{-10}$ m^5/N (12$\times 10^{-7}$ ft^5/lbf).

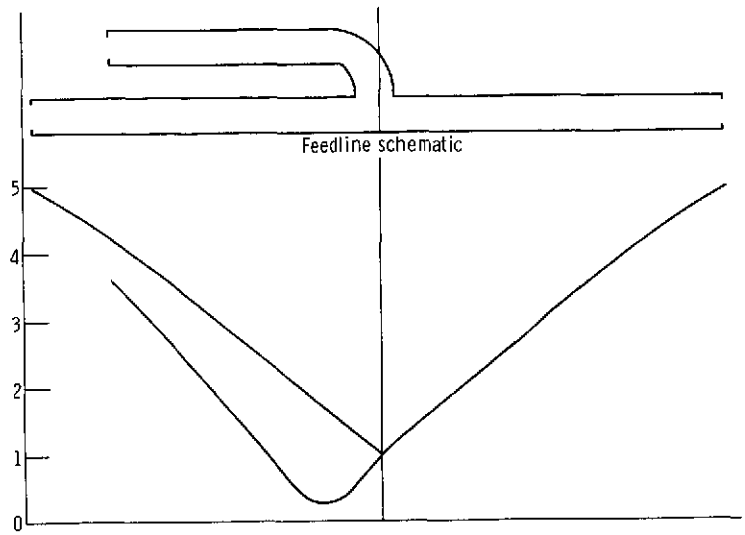

(a-7) Frequency, 65 hertz.

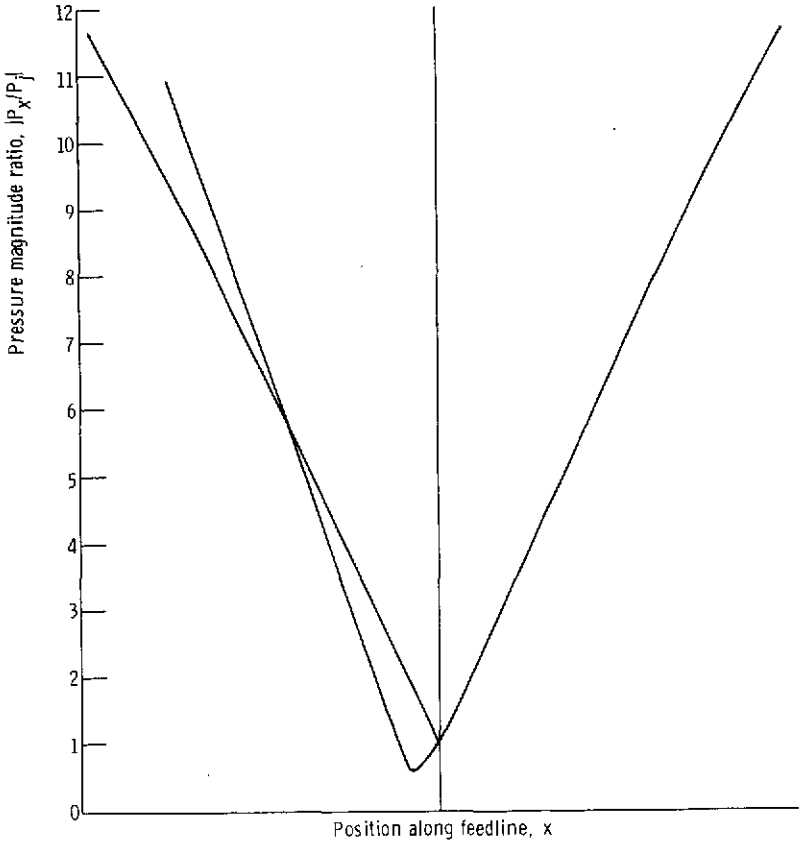

(a-8) Frequency, 70 hertz.

(a) Concluded.

Figure 42. - Continued.

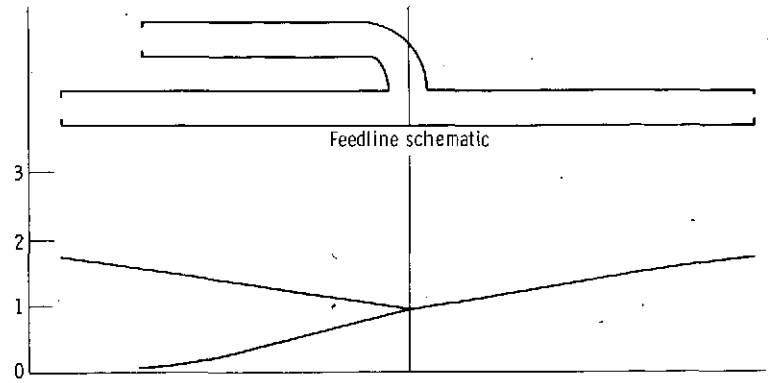

(b-1) Frequency, 48 hertz.

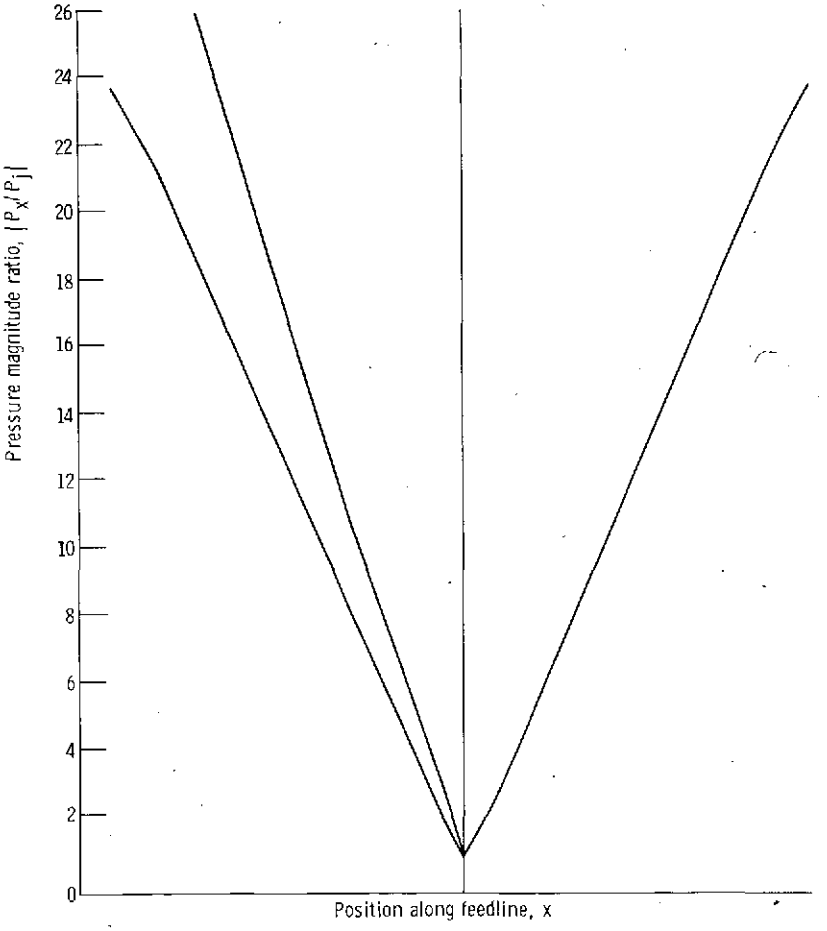

(b-2) Frequency, 74 hertz.

(b) Symmetrical and asymmetrical responses near resonant frequencies of 48 and 74 hertz.

Figure 42. - Concluded.

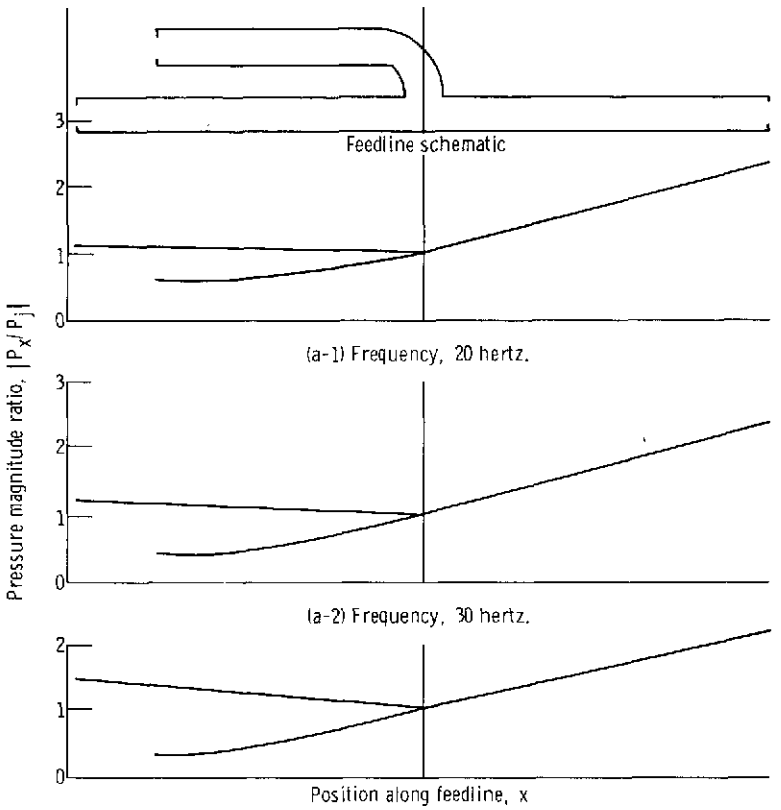

(a-1) Frequency, 20 hertz.

(a-2) Frequency, 30 hertz.

(a-3) Frequency, 40 hertz.

(a) Symmetrical response of system for frequency steps between 20 and 70 hertz.

Figure 43. - Pressure magnitude ratio - hydrogen feedline driving at l_3.
$R_A = 1.5 \times 10^6$ N-sec/ m^5 (885 lbf-sec/ ft^5); $R_E = 3.56 \times 10^8$ (2.1×10^5 lbf-sec/ ft^5);
$C_E = 118 \times 10^{-10}$ m^5/ N (2×10^{-7} ft^5/ lbf).

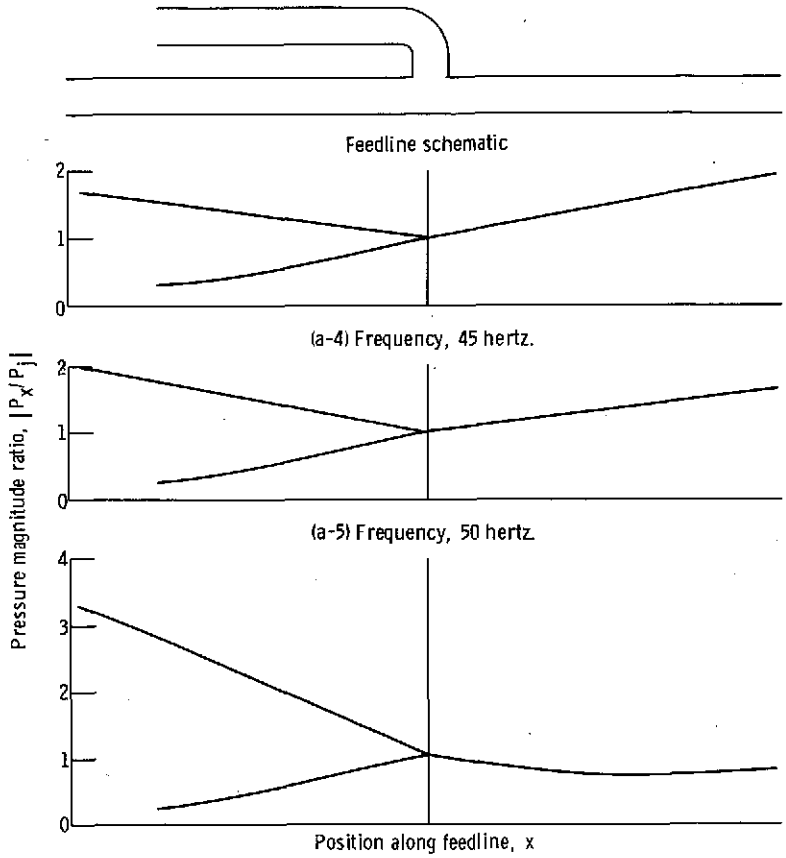

(a-4) Frequency, 45 hertz.

(a-5) Frequency, 50 hertz.

(a-6) Frequency, 60 hertz.

(a) Continued.

Figure 43. - Continued.

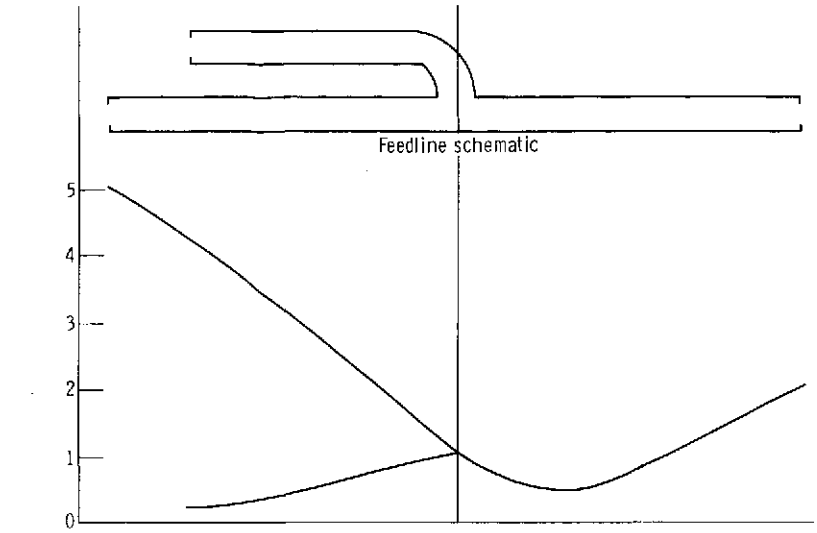

(a-7) Frequency, 65 hertz.

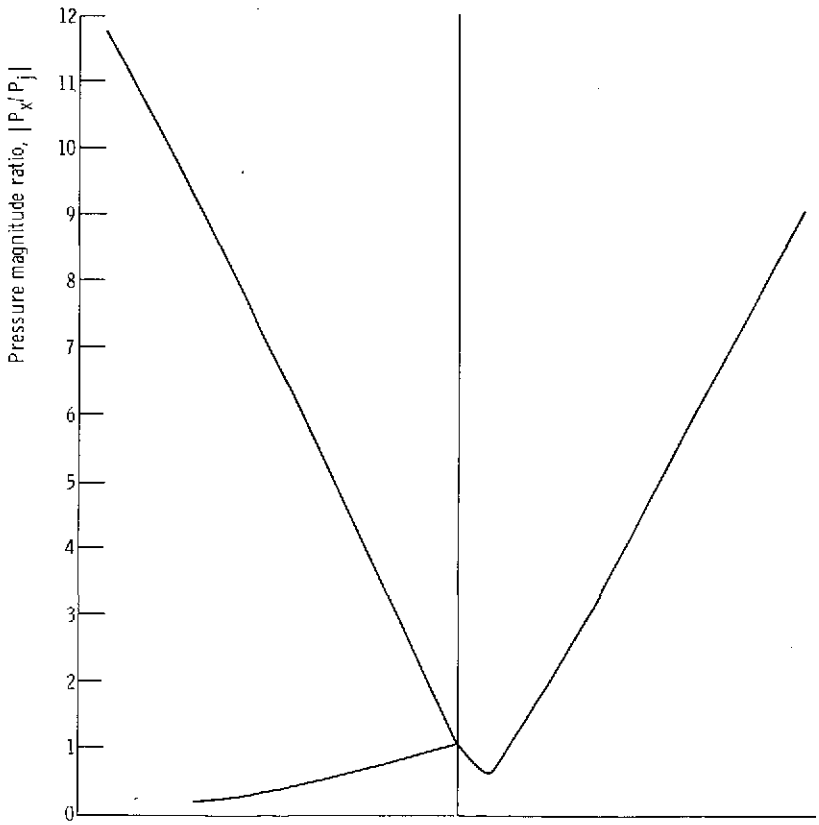

(a-8) Frequency, 70 hertz.

(a) Concluded.

Figure 43. - Continued.

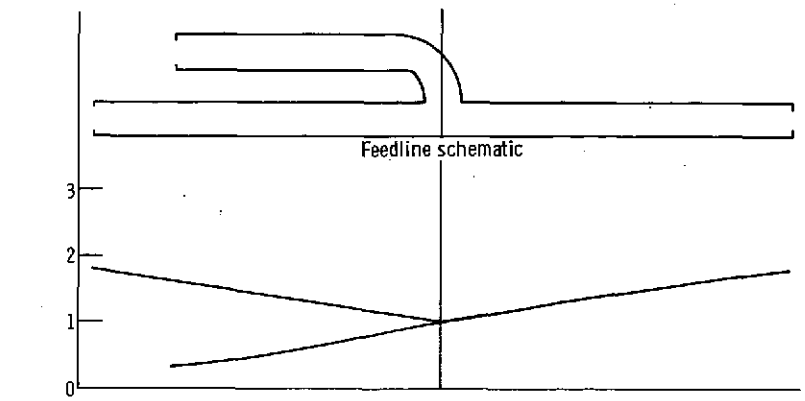

(b-1) Frequency, 47.6 hertz.

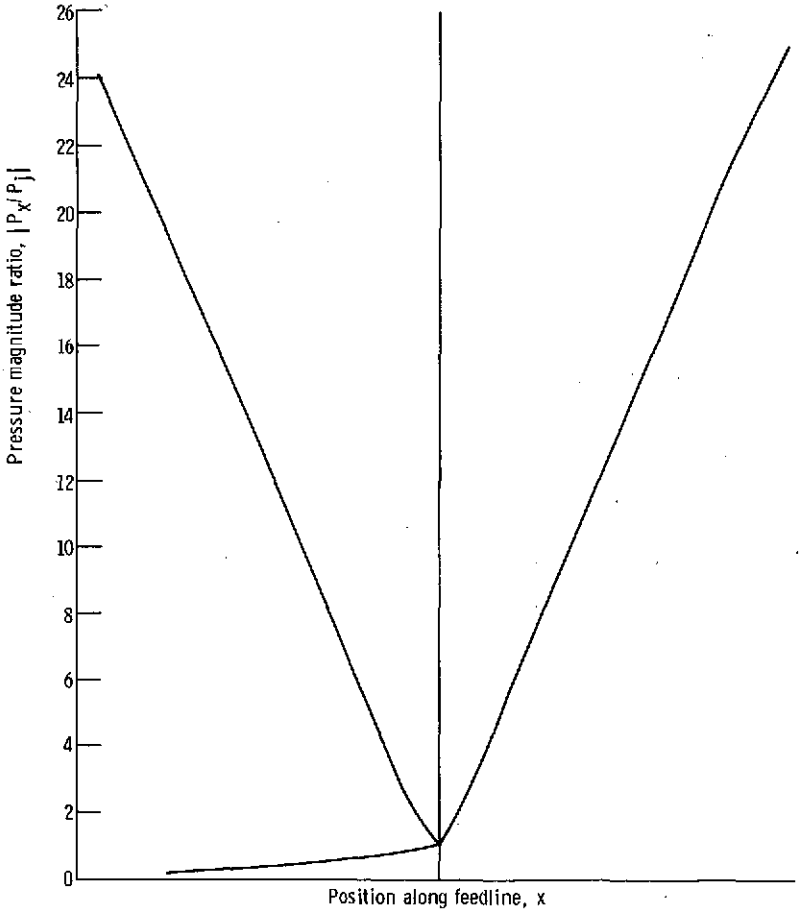

(b-2) Frequency, 73.2 hertz.

(b) Symmetrical and asymmetrical responses near resonant frequencies of 47.6 and 73.2 hertz.

Figure 43. - Concluded.

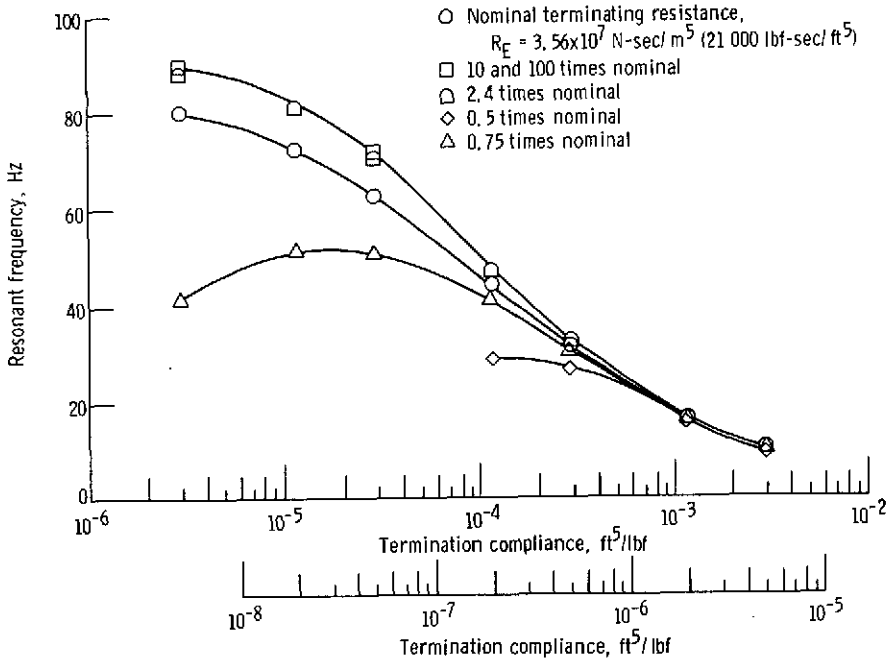

Figure 44. - Resonant frequency as function of termination compliance - based on peak in P_F/P_{AD}. R_A = 1.5x10^6 N-sec/ m^5 (885 lbf-sec/ ft^5).

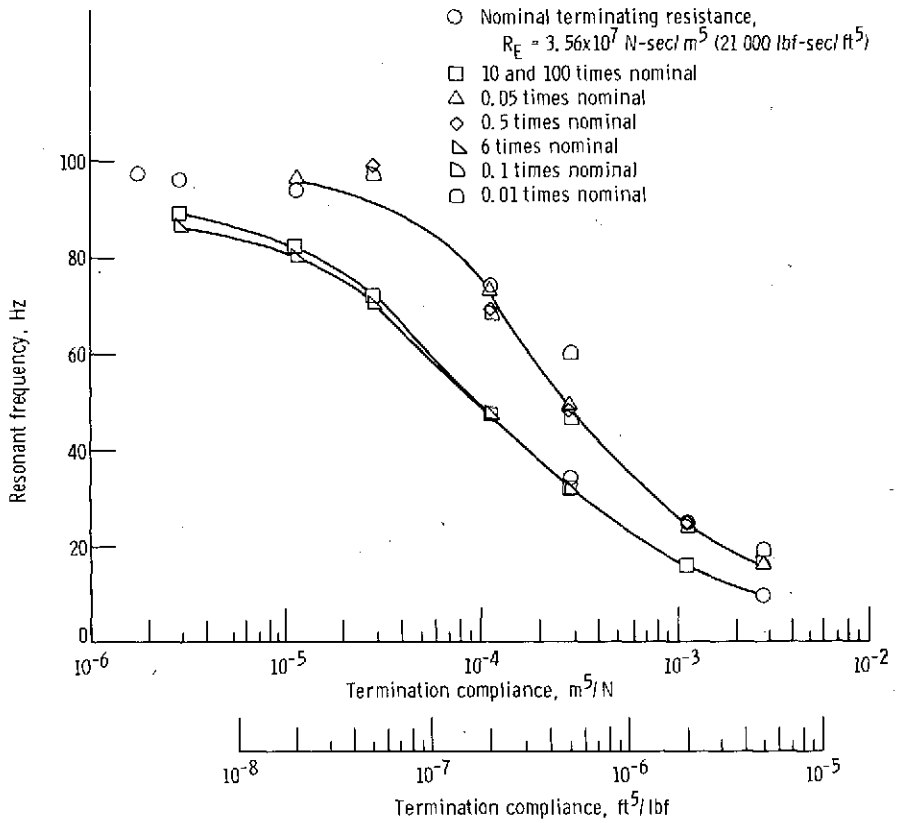

Figure 45. - Resonant frequency as function of termination compliance - based on peak in P_F/Q_3. R_A = 1.5x10^6 N-sec/m^5 (885 lbf-sec/ft^5).

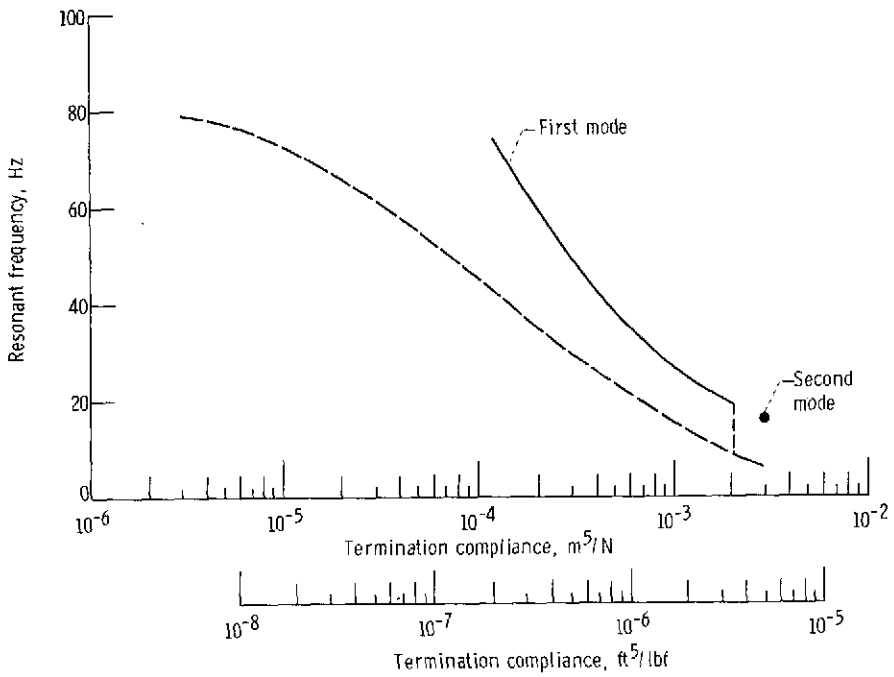

Figure 46. - Resonant frequency as function of termination compliance - hydrogen feedline driving at l_3 - with symmetric mode obscured by asymmetric mode. $R_A = 3.0 \times 10^6$ N-sec/ m^5 (1670 lbf-sec/ ft^5); $R_E = 3.56 \times 10^8$ N-sec/ m^5 (1000 lbf-sec/ ft^5).

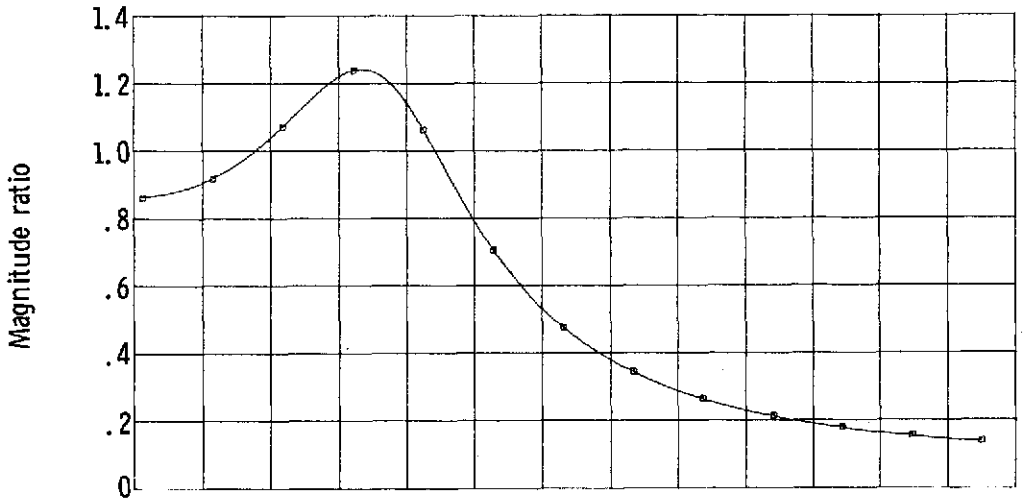

(a) Magnitude ratio.

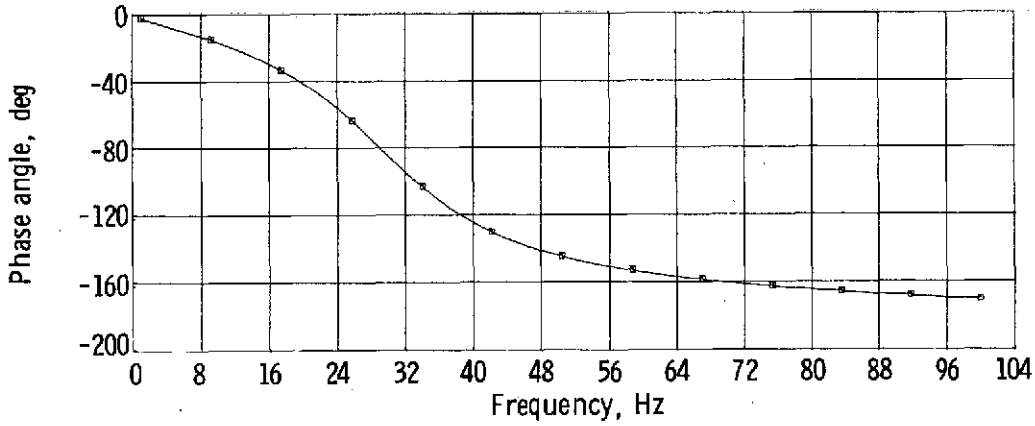

(b) Phase angle.

Figure 47. - Hydrogen feedline frequency response at resonant frequency of 27 hertz P_F/P_{AD} - driving at I_1.

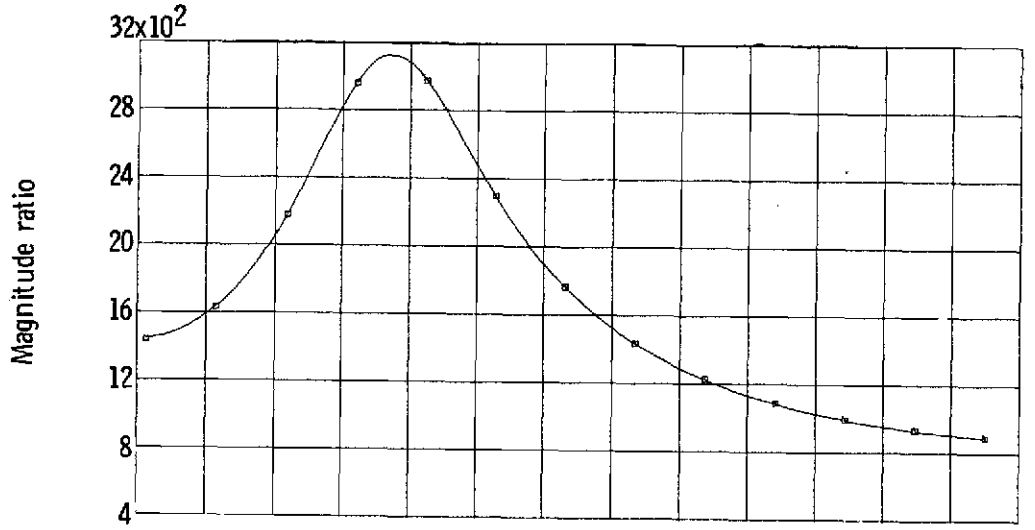

(a) Magnitude ratio.

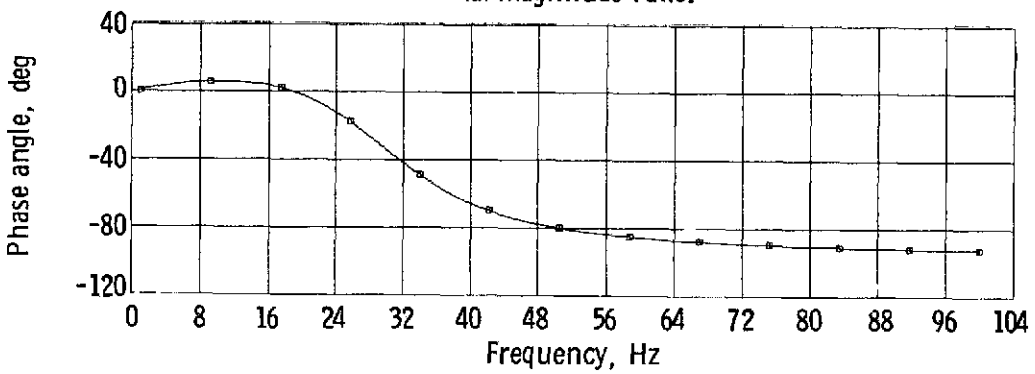

(b) Phase angle.

Figure 48. - Hydrogen feedline frequency response at resonant frequency of 30 hertz P_F/Q_J - driving at I_2.

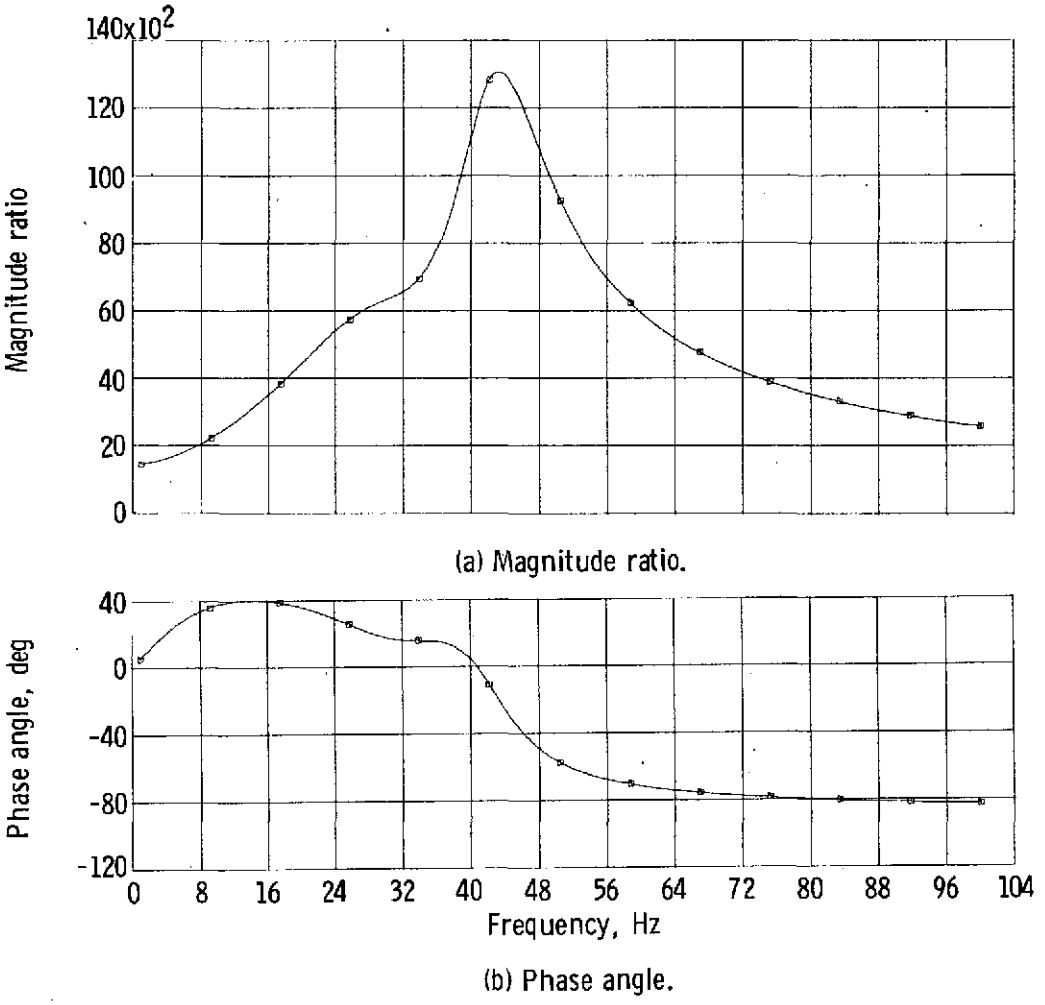

(a) Magnitude ratio.

(b) Phase angle.

Figure 49. - Hydrogen feedline frequency response at resonant frequency of 43 hertz P_F/Q_3 - driving at I_3.

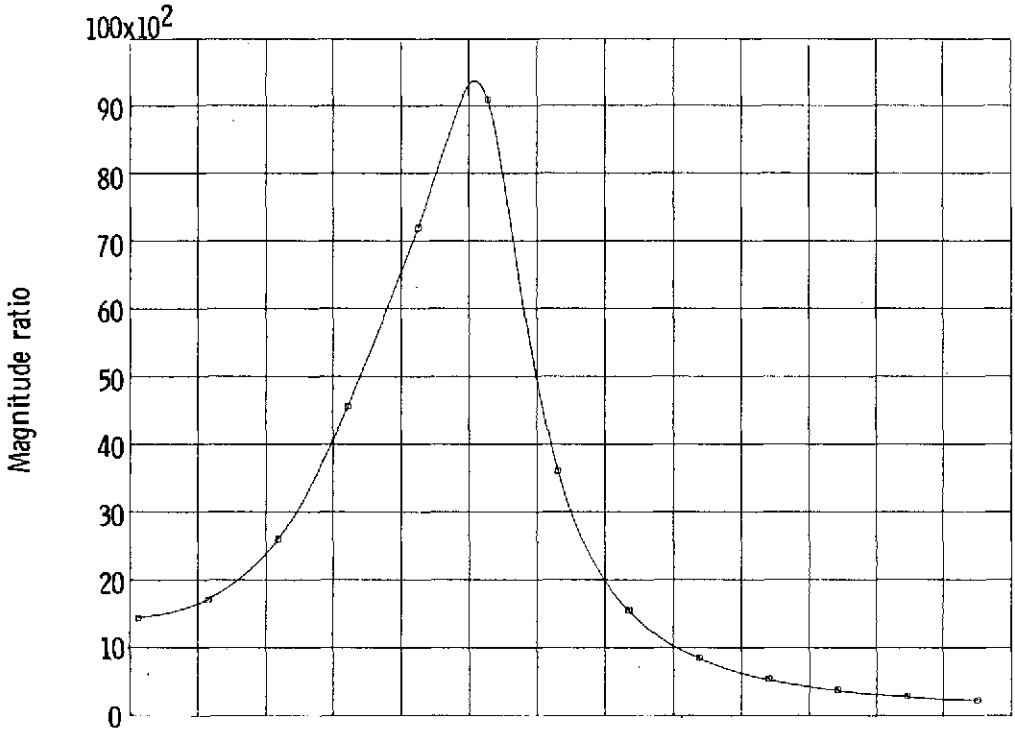

(a) Magnitude ratio.

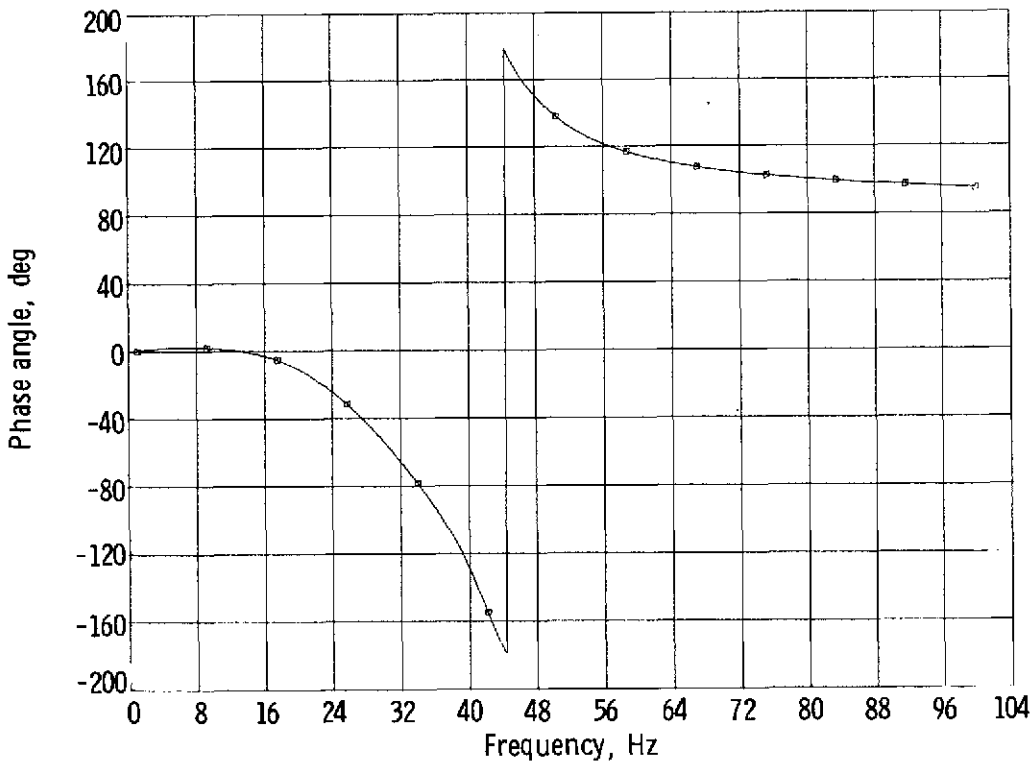

(b) Phase angle.

Figure 50. - Hydrogen feedline frequency response at resonant frequency of 41 hertz P_F/Q_4 - driving at I_4.